A NEW ULTRAWIDE-BAND (UWB) MICROWAVE IMAGING SYSTEM WITH MINIMIZED MUTUAL COUPLING EFFECTS FOR BREAST TUMOR DETECTION
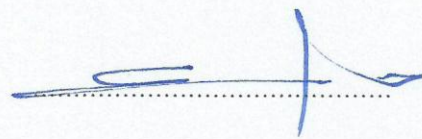
by

İlhami Ünal

Submitted to the Institute of Graduate Studies in

Science and Engineering in partial fulfillment of

the requirements for the degree of

Doctor of Philosophy

in

Electrical and Electronics Engineering
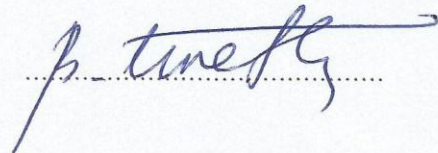
Yeditepe University

2013

A NEW ULTRAWIDE-BAND (UWB) MICROWAVE IMAGING SYSTEM WITH MINIMIZED MUTUAL COUPLING EFFECTS FOR BREAST TUMOR DETECTION
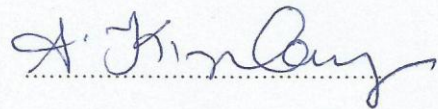
APPROVED BY:

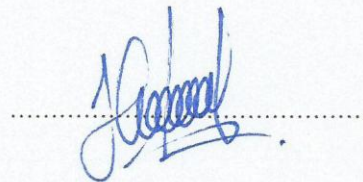Assoc. Prof. Dr. Cahit Canbay
(Supervisor)

Assoc. Prof. Dr. Bahattin Türetken
(Co-advisor)

Assoc. Prof. Dr. Ahmet Kızılay

Assist. Prof. Dr. Hamid Torpi

Prof. Dr. H. Selçuk Varol

DATE OF APPROVAL: …./…./….

ACKNOWLEDGEMENTS

ABSTRACT

A NEW ULTRAWIDE-BAND (UWB) MICROWAVE IMAGING SYSTEM WITH MINIMIZED MUTUAL COUPLING EFFECTS FOR BREAST TUMOR DETECTION

Electromagnetic waves and antennas have a huge application area, and one of the challenging areas is remote sensing systems and detection systems using microwaves, today. Increasing demand on non-destructive sensing or detecting breast tumor keeps this subject hot in this field. There are various passive and active microwave techniques which have been proposed as an alternative to the most widely used X-ray mammography for early detection of breast cancer, such as microwave radiometry, hybrid microwave-induced acoustic imaging, microwave tomography and UWB microwave radar technique. Because of its excellent advantages, recent years have shown a dominant interest in a UWB microwave imaging technique, for a particular technique to detect and locate a breast tumor.

This study will consist of an optimum antenna design with minimized mutual coupling effects, fabrication and testing for tumor detection. Realistic breast phantom models, as well as tumor-simulating objects, will be constructed for testing on. Images of the measured signals will be created as a function of position with fast and improved imaging algorithms. It's aimed to get better resolution results than similar recent developed microwave imaging systems.

ÖZET

MEME KANSERİ TÜMÖRÜNÜN TESPİT EDİLMESİ İÇİN KARŞILIKLI KUPLAJ ETKİLERİNİN MİNİMİZE EDİLDİĞİ ÇOK GENİŞ BANDLI (ÇGB) YENİ BİR MİKRODALGA GÖRÜNTÜLEME SİSTEMİ

Elektromagnetik dalgalar ve anten teknolojisi, günümüzde geniş bir uygulama alanına sahiptir ve güncel alanlarından biri de mikrodalga ile uzaktan algılama sistemleridir. Meme kanseri tümörü tespiti üzerine artan tahribatsız algılama ihtiyacı, elektromagnetik dalgalar konusunu bu alanda sıcak tutmaktadır. Meme kanserinin erken tanısında, en yaygın olarak kullanılan X-ışını mamografi tekniğine alternatif olarak birçok pasif ve aktif mikrodalga tekniği geliştirilmiştir. Bunlardan bazıları, mikrodalga radyometri, hibrit mikrodalga termoakustik görüntüleme, mikrodalga tomografisi ve çok geniş bandlı (ÇGB) radar-tabanlı mikrodalga tekniğidir. Mükemmel avantajları ve üstünlüğü nedeniyle, son yıllarda meme kanseri tümörü tespiti için ÇGB mikrodalga görüntüleme teknolojisi büyük ilgi görmektedir.

Bu çalışma, tümör tespiti için karşılıklı kuplaj etkilerinin azaltıldığı optimum anten tasarımı ile üretim ve testlerini içermektedir. Üzerinde çalışmak üzere tümör ve gerçekçi meme fantom modelleri imal edilecektir. Ölçülen sinyaller, hızlı ve geliştirilmiş görüntüleme algoritmaları kullanarak pozisyonun bir fonksiyonu olarak oluşturulacaktır. Günümüzdeki benzer şekilde geliştirilmekte olan görüntüleme sistemlerinden daha iyi çözünürlük elde edilmesi amaçlanmıştır.

TABLE OF CONTENTS

LIST OF FIGURES

LIST OF TABLES

LIST OF SYMBOLS / ABBREVIATIONS

$\mathbf{A}$	Magnetic vector potential
A	Radius of sphere
D	Distance between Vivaldi antenna and metal plate
$\mathbf{E}$	Electric field intensity
$\mathbf{E}^i$	Incident electric field intensity
E_0	Amplitude of electric field intensity
E_{rs}	r-component of the scattering electric field intensity
$E_{\theta s}$	θ-component of the scattering electric field intensity
$E_{\phi s}$	ϕ-component of the scattering electric field intensity
E_{qp}	Electric field intensity of the p. antenna effecting on the q. antenna
$\mathbf{F}$	Electric vector potential
f	Frequency
$\mathbf{H}$	Magnetic field intensity
$\mathbf{H}^i$	Magnetic field intensity
H_0	Amplitude of magnetic field intensity
h	Thickness of dielectric substrate rectangular microstrip patch antenna
$h_n^{(2)}$	Spherical Hankel function of the second kind of order n
I_p	Current distribution along the p. thin dipole antenna
I_q	Current distribution along the q. thin dipole antenna
j	Unit imaginary number
j_n	Spherical Bessel function of the first kind of order n
k	Propagation constant in medium
k_0	Propagation constant in free space (wave number)
L	Length of rectangular microstrip patch antenna
L_p	Antenna length of p. thin dipole antenna
L_q	Antenna length of q. thin dipole antenna
N	Number of planar layers
n	Order number for Bessel and Legendre functions

$P_n^1(\cos(\theta))$	Derivative of the associated Legendre function of the first kind of order n, with respect to θ
r	Spherical coordinate variable
R_0	Total reflection coefficient of N-layered lossy media
r_g	Radius of spherical gland tissue
S_{11}	Ratio of signal that reflects from port one for a signal incident on port one
S_{22}	Ratio of signal that reflects from port two for a signal incident on port two
S_{21}	Ratio of transmitted signal at port two to incident signal at port one
S_{12}	Ratio of transmitted signal at port one to incident signal at port two
T	Time
W	Width of rectangular microstrip patch antenna
Z_{qp}	Mutual coupling impedance between q. and p. thin dipole antennas
α	A measure of relaxation time distribution
Δt	Time-step for discretization of time
Γ	Reflection coefficient
ε	Permittivity of medium
ε_r'	Real part of relative permittivity of medium
ε_r''	Imaginary part of relative permittivity of medium
ε_r	Relative permittivity of medium
ε_0	Absolute permittivity of free space
$\varepsilon_{r\infty}$	Relative permittivity at high frequency range
ε_{rs}	Relative permittivity at low frequency range
η	Characteristic impedance of medium
λ_0	Wavelength in free space
λ	Wavelength in medium
μ	Permeability of medium
μ_o	Permeability of free space
v	Phase velocity of electromagnetic field in medium
ω	Angular frequency

ω_o	Resonance frequency
ϕ	Spherical coordinate variable
ψ	Angle of incidence measured from the tangential axis to the boundary
σ	Conductivity of medium
σ_s	Conductivity of medium at low frequencies
σ^*	Complex conductivity of medium
$\tan\delta$	Loss tangent
τ	Relaxation time
τ^d	Time delay
θ	Spherical coordinate variable
θ_i	Angle of incidence measured from the normal axis to the boundary
θ_t	Angle of refraction
ACS	American Cancer Society
CMI	Confocal Microwave Imaging
CST	Computer Simulation Technology
CT	Computed Tomography
DAS	Delay-and-Sum
DMIST	Digital Mammographic Imaging Screen Trail
DOT	Diffuse Optical Tomography
EIT	Electrical Impedance Tomography
EMF	Electromotive Force
FEKO	FEldberechnung für Körper mit beliebiger Oberfläche
PEC	Perfectly Electric Conductor
PEM	Positron Emission Mammography
PET	Positron Emission Tomography
MAMI	Multistatic Adaptive Microwave Imaging
MEG	Magnetoencephalography
MIST	Microwave Imaging via Space-Time
MRI	Magnetic Resonance Imaging
NIR	Near Infra-Red
RCB	Robust Capon Beamforming

SQUID	Superconducting Quantum Interference Device
TDLU	Terminal Duct Lobular Unit
TE	Transverse Electric
TM	Transverse Magnetic
UWB	Ultrawide-band

1. INTRODUCTION

1.1. OVERVIEW OF BREAST CANCER DETECTION

Cancer is one of the leading causes of mortality with more deaths per annum than heart disease among those under 85 years of old [1]. Breast Cancer is especially one of the main causes for women's death in all over the world [2]. It's the second leading cause of female cancer mortality [3]. According to the American Cancer Society (ACS), 230,480 women were anticipated to be diagnosed with breast cancer in the USA in 2011 alone [4]. Breast cancer was anticipated to be responsible for almost 40,000 deaths in the USA in 2011 [4]. These statistics clearly demonstrate the importance of this disease and its impact on the health. The early detection of tumor could help to reduce the higher percentages of death cases and thus save a lot of lives.

There are over 200,000 new cases of invasive breast cancer diagnosed each year in the USA. One out of every seven women in the USA will be diagnosed with breast cancer in their life time [3]. In Turkey, one out of every twelve women is diagnosed with breast cancer. The frequency of diagnosis of breast cancer especially increased after 1970s. Every year, one of 44,000 women is died by breast cancer in the world.

Breast cancer is the most frequent cause of cancer related death for women in both developed and developing countries [1]. The estimated number of deaths globally due to breast cancer in 2008 was 458367. Mortality rates show less geographical variation compared to incidence rates because of the more favorable survival of breast cancer in high-incidence developed regions. The world standardized mortality rate for breast cancer is 12.5 per 100000 and ranges from 17.5 per 100000 in Western Europe to 6.3 per 100000 in Eastern Asia, as shown in Figure 1.1 [1].
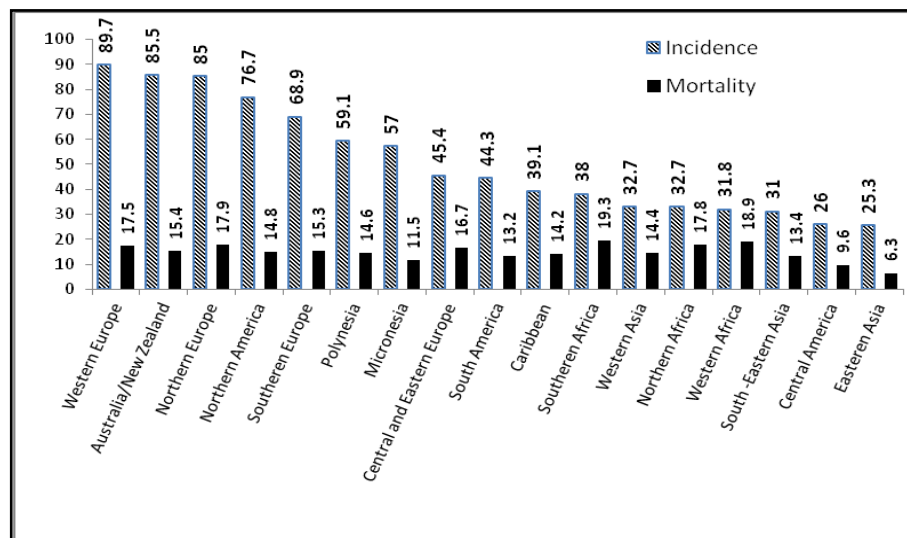
Figure 1.1. Age standardized incidence and mortality rates for breast cancer worldwide per 100000 in 2008 [1]

Early diagnosis and treatment are the hot keys to survive from the breast cancer. The present "golden standard" screening technology for detecting early-stage breast cancer is X-ray mammography. Despite the fact that X-ray mammography provides high resolution images, it's not highly reliable. It has high false-negative and false positive rates [5-8]. The most widely used X-ray mammography also requires painful and uncomfortable breast compression and exposes the patient to ionizing radiation. Digital tomosynthesis technology has less X-ray radiation level than conventional and digital mammography with advantages of less compression and less pain (around 30 per cent less). However it's an expensive technology. Ultrasound technology is harmless but it is less effective than mammography, therefore it's used as a supporting imaging technique for mammography. Magnetic resonance imaging (MRI) is another option, but it is too expensive and not suitable for routine breast screening. There are more breast screening techniques used in hospitals and under investigation. A comprehensive list of modalities used for breast imaging can be found in [9]. The limitations of existing breast cancer detection methods motivate the research studies for new breast screening techniques. An ideal breast cancer detection method should have the following properties [3-10]:

- has low health risk,
- is sensitive to tumors and specific to malignancies,

- detects breast cancer at a curable stage,
- is noninvasive and simple to perform,
- is cost effective and widely available,
- involves minimal discomfort, so the procedure is acceptable to women,
- provides easy to interpret, objective, and consistent results,
- imaging as fast as possible.

However, even with the combined use of mammography, ultrasound, and MRI techniques, the current method of screening for breast cancer does not meet the ideal requirements. Therefore, researchers are actively searching for alternative modalities of screening and diagnostic breast imaging [10]. Electromagnetic waves and antennas have a huge application area, and one of the challenging areas is remote sensing systems and detection systems using microwaves, today. Increasing demand on non-destructive sensing or detecting breast tumor keeps this subject hot in this field. There are various passive and active microwave techniques which have been proposed as an alternative especially to the most widely used X-ray mammography for early detection of breast cancer, such as microwave radiometry [11], hybrid microwave-induced acoustic imaging [12], microwave tomography [13] and UWB microwave radar technique [8, 14-18].

X-ray mammography has several limitations, especially when dealing with younger women who have dense breast tissues. Therefore, there is a small contrast between healthy and diseased breast tissues at X-ray frequencies [8]. On the other hand, the physical basis for microwave detection of breast tumor is the significant contrast in the electrical properties of the normal and the malignant breast tissues [8], which exists in the earliest stage of tumor development. Another advantage of the microwave imaging technique is that it would be nonionizing and noninvasive. It does not also require painful breast compression. Furthermore, microwave attenuation in normal breast tissue is low enough to make signal propagation through even large breast volumes quite feasible [8]. It would also let 3-D imaging results in a very short time interval, too.

The passive methods (microwave radiometry) use radiometers to measure the temperature differences in the breast as temperature increases in the presence of tumor than with healthy breast tissue [11]. The hybrid methods (microwave-induced acoustic imaging) use

microwave energy to heat tumors. They expand and generate pressure waves which are detected by ultrasound transducers [12]. Currently, there are two main active methods involve illuminating the breast with microwaves and then measuring transmitted or backscattered signals; such as microwave tomography [13] and radar-based imaging [8, 14-18]. The microwave tomography system is low cost and easy to build because it is a narrow-band system [3]. However, in microwave tomography, a nonlinear inverse scattering problem is solved to reconstruct an image of the dielectric properties in the breast. The inverse scattering approach does not require any a priori information about the imaged object to produce the complex dielectric constant distribution. However, in practice it often faces difficulty in converging to the right solution due to the ill-conditioned non-linear problem it tackles [18].

In contrast to the image reconstruction aim of the microwave tomography technique, ultrawide-band (UWB) radar-based imaging approach solves a simpler computational problem faster dealing with only to identify the presence and location of significant scattering obstacles such malignant breast tumors. The UWB radar approach requires an estimate of average dielectric properties of the body to form an image. Its main challenge comes from a small return signal due to a target which is masked by a large signal caused by reflections at an air-imaged body interface. UWB radar technology itself encompasses a diverse range of fields including microwave and antenna theory to capture the backscattered signals, digital signal processing to locate the target tissue and for the image computation and software engineering for the collection of the data and image output.

Because of its excellent advantages, recent years have shown a dominant interest in a UWB microwave imaging technique, for a particular technique to detect and locate a breast tumor. The UWB microwave radar-based imaging technique specifically uses short duration pulses. Using a mechanical scanning sub-system, measurements are repeated for different locations of an UWB probe antenna. In the electronic equivalent, UWB array antenna with switched elements is used. The UWB radar technique offers creation of an image, which can be formed by combining all of the signals (S_{ii} and S_{ij}, $i{\neq}j$) coming from different antennas in a very short time [19-21]. Well-known delay-and-sum (DAS) algorithm is used to create microwave images of breast cancer tumors [8, 22, 23]. In order to enhance the tumor detection, microwave imaging via space-time (MIST) beamforming

[14, 24, 25], robust capon beamforming (RCB) [26] and multistatic adaptive microwave imaging (MAMI) [27] algorithms can also be employed. Comparisons of these techniques are given in [15, 28].

In order to enhance their detection capabilities, the two techniques require the use of high sensitive antennas operating over a considerable UWB frequency range, as well as, the use of better algorithms to eliminate possible clutters in the image to increase detection ability of the microwave imaging system.

1.2. BASIC ANATOMY OF BREAST

In the development of an alternative technology of breast cancer screening, it is important to have a basic understanding of the anatomy, histology, and pathology of the breast. The breast (Figure 1.2) is a modified skin gland that lies on the chest wall, usually between the clavicle and the sixth rib, and is bounded externally by skin and internally by the pectoralis muscle. Breast tissue also extends up into the axilla (underarm region) via a pyramidal-shaped axillary tail. The tissue in the breast primarily consists of a combination of fat and glandular tissue, with the relative proportions of the two varying widely. The remainder of the breast is made up of connective tissue, vascular tissue, lymphatics, and nerves. The key features of each of these elements are described below [10].
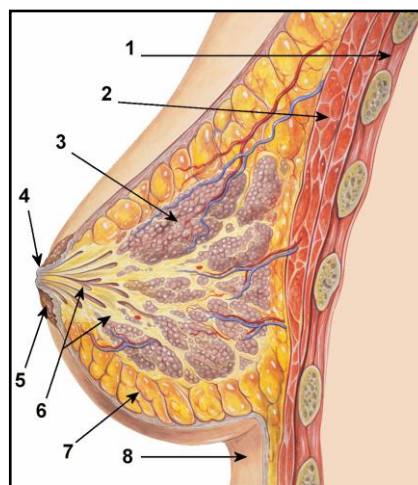
Figure 1.2. Anatomy of the breast: 1. chest wall, 2. pectoralis muscles, 3. lobules, 4. nipple, 5. areola, 6. ducts, 7. fatty tissue, 8. skin [10]

1.2.1. Adipose (Fatty) Tissue

The adipose tissue in the breast can be divided into three main groups: subcutaneous (directly beneath the skin), retromammary (back of the breast), and intraglandular (between the glandular structures). The subcutaneous and retromammary fat regions form a layer between the majority of the glandular tissue and the external boundaries (skin and pectoralis muscle) of the breast. The majority of cancers develop in the region of glandular tissue within 1 cm of these fat layers. Unfortunately, the layers of fat do not completely isolate the glandular tissue from either the surrounding skin or muscle, which enables the cancer to spread. The amount of fat generally increases with age, body mass, and breast size, but this is by no means an absolute [10, 29].

1.2.2. Glandular Tissue

The glandular tissue in the breast consists of a number of discrete lobes, which are made up of lobules (which produce milk) and ducts (which deliver it to the nipple). There are approximately 15-20 lobes in each breast, and each lobe is thought to be exclusively drained by its own individual duct system. Within a lobe are dozens of lobules 2-3 mm in diameter, and within each lobule are as many as 100 alveoli (often referred to as acini), which are the basic secretory units of the breast. The ductal system can be thought of as a tree-like structure, with a single lactiferous duct that opens at the nipple acting as a trunk that branches into many smaller ducts that each end in what has been termed the terminal duct lobular unit (TDLU) [10, 30].

1.2.3. Skin and Connective Tissues

The breast is supported by a combination of connective tissue and skin. The skin overlying the breast generally varies in thickness between 0.8 mm and 3 mm, and skin thickness tends to be inversely proportional to breast size. The skin also contains the nipple, which is slightly below the center point of the breast and extends about 5-10 mm above the skin surface, and the surrounding areola, which contains a number of small bumps called Montgomery's glands, which lubricate the skin during breast feeding. Finally, the breast is supported by a surrounding layer of fascia (connective tissue), which is interspersed with

the subcutaneous and retromammary adipose tissue, and by a number of suspensory ligaments (Cooper's ligaments) that provide an internal supporting framework for the breast lobes [10, 30].

1.2.4. Vascular and Nerve Tissues

The breast receives its blood supply from a variety of axillary, internal thoracic, and intercostal arteries. Each artery generally has a corresponding veinous channel which drains a web of veins originating from the nipple, the subcutaneous layer, and the glandular tissue of the breast. Similarly, the breast receives its nerve supply from multiple branches of the intercostal nerves [10, 31].

1.2.5. Lymphatic Tissue

The lymphatics, vein-like vessels that drain lymph fluid into the blood stream, represent the body's main line of defense in the body's immune response, but they also provide a conduit for cancer cells to spread and metastasize. In the breast, the vast majority of lymphatics travel from the nipple to lymph nodes in the axilla, and from there to nodes above the collar bone. Some lymphatics also drain the rear part of the breast to nodes under the breast bone (internal thoracic nodes). Finally, there are also a small number of lymph nodes within the breast itself [10].

1.3. BREAST CANCER SCREENING TECHNIQUES

Based on the definition given by the ACS, cancer refers to a group of diseases characterized by uncontrolled growth and spread of abnormal cells [9]. Cancer can develop almost anywhere in a human body, such as the skin, marrow, bone, brain, breast, colon, liver and lung. Cancer can also strike people at any age. In all of these cancer cases, only about 10 per cent are genetically related and approximately 1/3 of the deaths can be completely avoided with appropriate diet and healthier living styles (such as not smoking and drinking) [9].

Breast cancer is a type of cancer originating from breast tissue, most commonly from the inner lining of milk ducts or the lobules that supply the ducts with milk. There are several types of breast cancer. In many cases, breast cancer starts in the ducts or lobules of the breast (where milk can be produced). In the early stages of breast cancer, breast tumors found in these ducts are called "in situ" meaning that they are in one location and are noninvasive. Invasive breast cancer means that the cancerous breast tumor has broken through the wall of the ducts or lobules and spread to other parts of the body.

Since early diagnosis and treatment are the hot keys to survive from the breast cancer, there are several techniques that are used for detection of early stages of breast cancer such as; mammography, tomosynthesis, ultrasound technique, magnetic resonance imaging (MRI), and other emerging electromagnetic techniques under development.

1.3.1. Mammography

Mammography as the standard imaging method for breast cancer screening has resulted in reduced breast cancer mortality over years. However, the number of cancers undetected through mammography is substantial, particularly for women with dense breast tissue, with sensitivity as low as 30–48 per cent [32].

The Digital Mammographic Imaging Screen Trail (DMIST), which is 3-4 times more expensive, found an improvement from 55 per cent to 70 per cent in cancer detection compared to film mammography [33]. Even though there is substantial number of undetected cancer cases with digital technology, mammographically missed cancer is a particular problem for women with dense breasts (Figure 1.3).

One of the main drawbacks is the high miss detection which can reach 30 per cent [34] with high false positive (lead to unnecessary biopsies) and negative detection. In some cases, it cannot detect if the tumor size is too small, at the same time unable to differentiate between malignant and benign tumors. The main drawback is, it is very painful for the patients, harmful for human tissue and it poses a considerable risk of causing the very cancer, it is not recommended to be used on patients under 40 years old [35]. To date, no main stream method has been developed that provides a safer and/or more accurate method

than traditional mammography.
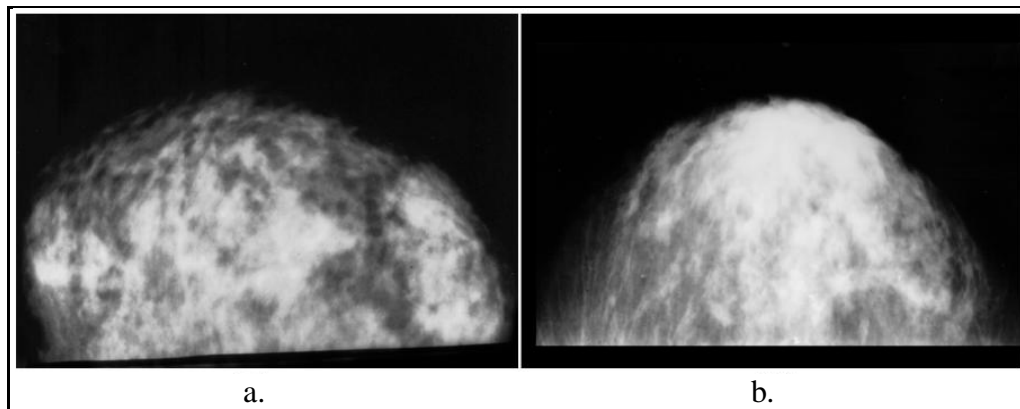
Figure 1.3. Difficulty imaging dense breasts with mammography: a. normal, b. cancerous

[33]

1.3.2. Digital Tomosynthesis

Mammography is an effective imaging tool for detecting breast cancer at an early stage and is the only screening modality proved to reduce mortality from breast cancer. However, the overlap of tissues depicted on mammograms may create significant obstacles to the detection and diagnosis of abnormalities. Breast tomosynthesis, a new tool that is based on the acquisition of three-dimensional digital image data, could help solve the problem of interpreting mammographic features produced by tissue overlap. Breast tomosynthesis has the potential to help reduce recall rates, improve the selection of patients for biopsy, and increase cancer detection rates, especially in patients with dense breasts [36].

In analog (screen-film) mammography, X-rays from a stationary tube are absorbed by a phosphor screen, which then emits light and exposes a film to create an image. In breast tomosynthesis, a moving X-ray source and a digital detector are used. The X-ray tube in a breast tomosynthesis system moves along an arc during exposure (Figure 1.4). In theory, the motion of the tube could be linear, circular, or elliptic; the system we use currently is equipped with a tube that moves in an arc [36].
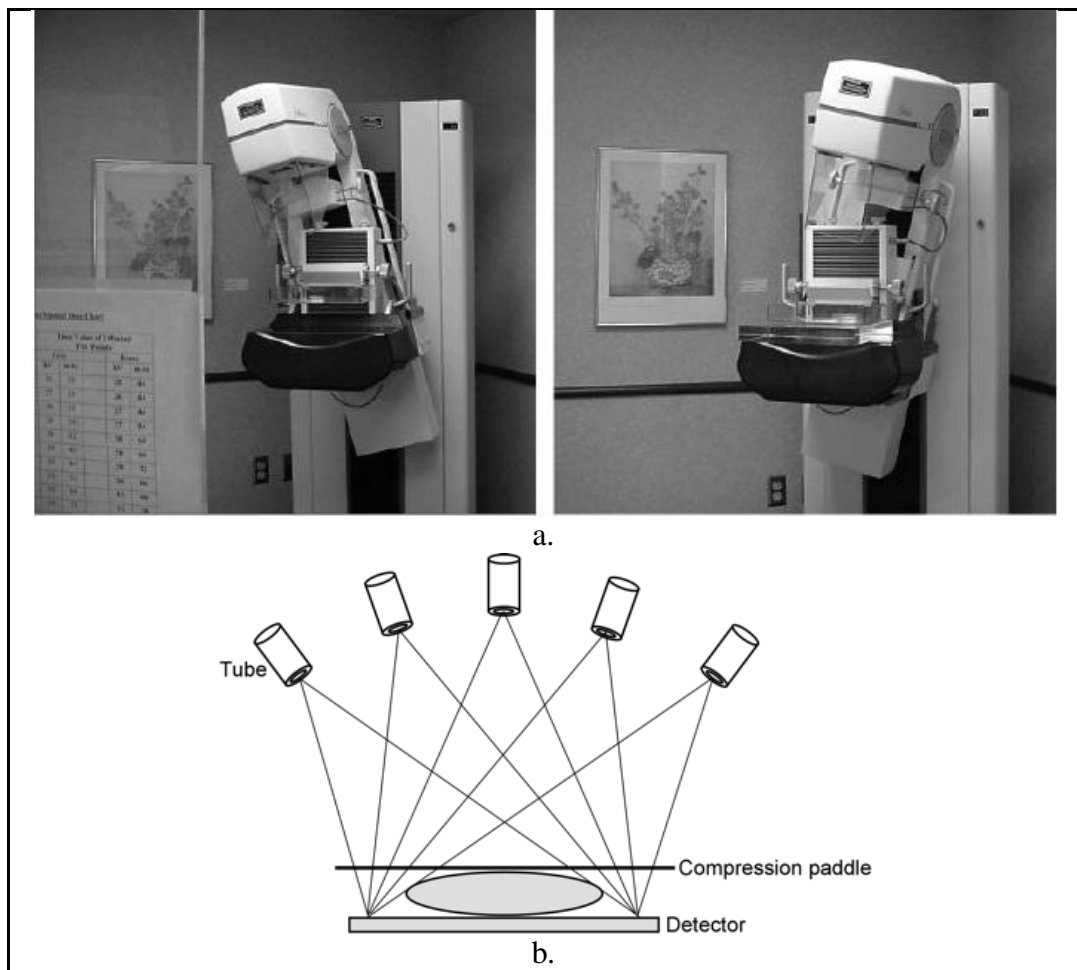
Figure 1.4. a. Digital tomosynthesis equipment, b. motion of the tube in an arc [36]
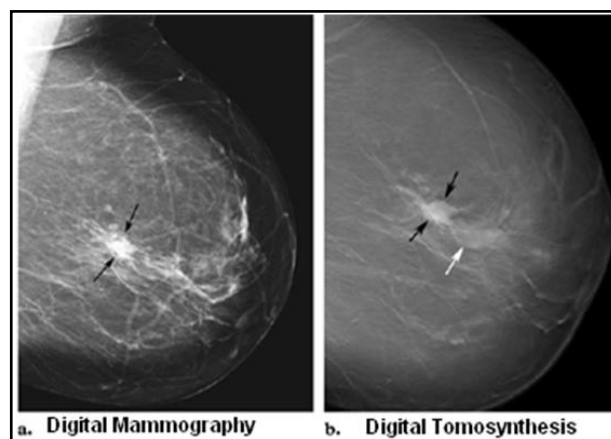
Figure 1.5. Comparison of the two imaging results for a. digital mammography, b. digital
tomosynthesis [36]

The clearer depiction with tomosynthesis should allow easier differentiation between benign and malignant lesions (Figure 1.5).

One can also list the disadvantages and advantanges of tomosynthesis as follows:

- Big detectors and difficulty in giving positions.
- Long application time interval can lead possible movement with some artifacts in the image.
- Large calcifications can lead some artifacts in the image.
- Long Evaluation Time.
- Still Ionizing Radiation.
- 3-D Imaging Availability.
- Imaging the tumor which has been hidden behind the dense breast tissue, too.
- Less possible repetitive films. Less X-ray radiation.
- Increased true diagnosis decreasing surgery and biopsy rates.
- Less compression, less pain (30 per cent less).

1.3.3. Ultrasound Technique

Ultrasound is an attractive supplement to mammography because it is widely available and relatively inexpensive. This technique requires high skill and longer time, and that is why the technique is not used [37]. However, the main disadvantage is its disability to produce high resolution for deep and condensed tissue structure such as fatty tissues [38]. The false-positive results could lead to more procedures, including biopsies that are not necessary. Although ultrasound is often used in an attempt to prevent an invasive measure for diagnosis, sometimes it is unable to determine whether or not a mass is malignant, and a biopsy will be recommended. Preliminary data from a trial being conducted showed that there was a higher rate of false-positive results with ultrasounds than with mammography stated as 2.4 per cent-12.9 per cent for ultrasound and 0.7 per cent-6 per cent for mammography [39].

Ultrasound imaging relies on high frequency sound waves that reflect with varying intensity from different tissues. In the breast, ultrasound is able to differentiate skin, fat,

glandular tissue, and muscle. However, for a number of reasons, ultrasound has yet to prove itself as an effective breast cancer screening methodology, despite improvement in recent years. A major limitation of ultrasound, unfortunately, is that breast fat and most cancer cells have similar acoustic properties, which makes detecting many tumors impossible with ultrasound. Also, it is important to recognize that the vast majority of ultrasound procedures are performed using hand-held devices, making the imaging results highly operator-dependent.

1.3.4. Magnetic Resonance Imaging (MRI)

Magnetic resonance imaging relies on the interaction of RF energy and strong magnetic fields with the magnetic properties of certain atoms to produce high resolution images. Magnetic Resonance Imaging (MRI) is costly and has recently been recommended by the American Cancer Society (ACS) to screen women at very high risk of breast cancer [40]. In literature [41], MRI had a specificity of only 95.4 percent, compared to 96, 99.3, and 99.8 percent for ultrasound, clinical breast exam, and mammography, respectively. Because of lower specificity and higher cost, compared to mammography, MRI may not be optimal for breast cancer screening. In a study performed on women with a high risk factor for cancer, over 15 per cent, the sensitivity of MRI was estimated to be 71.1 per cent, compared to 40 per cent for mammography and 17.8 per cent for clinical breast examination [41]. MRI has several advantages such as a high sensitivity, no ionizing radiation, and the ability to image radio graphically dense breast. However, the prime limitation of MRI is the high cost of imaging [4].

Some advantages and disadvantages of various imaging techniques used in hospitals can be summarized as follows:

Table 1.1. Advantages and disadvantages of different imaging techniques for breast cancer detection

Imaging Technique	Method	Advantages	Disadvantages
Analog (Conventional) Mammography	X-ray	Cheap Short application time	Not convenient for women with dense breasts. Negative False Rate 10-30 per cent. Ionizing Radiation, Dangerous. Compressed Breast, Pain.
Digital Mammography	X-ray	Availability of copying and archiving the images Image Processing	Same disadvantages as analog mammography. 3-4 times more expensive than analog mammography.
Tomosynthesis	X-ray	3-D Image Reconstruction by getting data from different angles. Increased imaging feature of lesions.	Ionizing Radiation. Less compression, less pain (around 30 per cent less than mammography).
Ultrasonography	Ultrasonic Sound Waves	Used as scanning for women with dense breasts. Cheaper than Mammography. No danger, no ionizing radiation.	More Negative False Rate than Mammography 17 per cent. Cannot image the whole breast at the same time. Cannot image the deep locations in the breast. Cannot image calcifications for early detection. Cannot diagnosis malign tumors.
Magnetic Resonance Imaging (MRI)	High Power Magnetic Field and RF	Method for diagnosis. Additional method for mammography for women with high risk. No ionizing radiation.	High Negative false rate, increased biopsy rates. High Cost.
Computed Tomography (CT)	X-ray	Real 3-D Images.	Ionizing Radiation. Radiation dose (average) 6 mGy. Calcifications can be imaged better in mammography. If contrast is not applied, malign tumors cannot be detected in dense breasts.
Positron Emission Tomography (PET)	Nuclear medicine Gamma-ray	Reconstructed Images from 3 different spatial planes. Not anatomical, but physiological imaging.	Less spatial resolution than CT. Ionizing Radiation. Long evaluation time.
Positron Emission Mammography (PEM)	Nuclear medicine Gamma-ray	Diagnosis Purpose.	Expensive. Long evaluation time. High radiation dose (0.01 Gy). Compression of breast as mammography.

1.3.5. Emerging Electromagnetic Techniques

Especially, the limitations of the X-ray mammography method present a significant challenge to the accurate detection of breast cancer. These limitations are behind the motivation to develop alternative detection techniques.

Electrical impedance tomography (EIT), diffuse optical tomography (DOT), biomagnetic and microwave imaging techniques are other alternative electromagnetic detection techniques. In particular, they have been receiving rising interest in recent years.

1.3.5.1. Electrical Impedance Tomography (EIT)

EIT, a 2-D or 3-D reconstruction of the impedance of the breast is created over the range of frequency from 100 Hz to 1 MHz [42]. EIT is accomplished by placing sensors on the surface of the breast with each sensor applying a current and then measuring the resulting voltage differences across the sensors. In some versions of EIT, a voltage was applied and the generated currents were measured. By applying suitable reconstruction algorithms, the impedance of the breast could be reconstructed using the applied currents and the measured voltages [43]. Due to the differences between the permittivity and conductivity of cancerous and healthy tissue in the frequency range less than 1 MHz, tumor regions have different complex impedances compared to the surrounding healthy tissue. However, it was approved to be used in association with X-ray mammography and not independently [43]. One of the practical EIT system called "The TransScan system" suffers from the limitation that artifacts due to interfering muscles and bones could appear in the impedance map and also the maximum reliable imaging depth is 3.5 cm. The smallest reconstructed tumors in clinical experiments had diameters ranging between 3–5 mm [43].

Imaging algorithms for EIT usually assume quasi-static variations to simplify Maxwell's equations. EIT imaging algorithms typically involve the solution of the inverse problem which is in general nonlinear, ill-posed and highly dependent on the electrode model, experimental errors, and noise [44].

1.3.5.2. Diffuse Optical Tomography (DOT)

Diffuse optical tomography (DOT) of breast cancer is defined as the use of light to image the optical properties of the breast interior. Compared to other breast cancer detection modalities, DOT uses significantly higher frequencies in the near infra-red (NIR) range from about 650 to 950 nm in wavelength [45]. The 650 to 950-nm wavelength range represents a spectral window where the penetration of light through the biological tissue is maximal and, therefore, larger imaging depth can be achieved. DOT typically exhibits a minimum detected tumor size of 5–10 mm [46]. In mammography, the incident X-ray photons travel through the breast in straight lines; however, in DOT the NIR photons experience multiple scattering as they propagate through the breast [45]. In this frequency range, the propagation of light through biological tissue can be approximated with reasonable accuracy using the diffusion equation and hence the name diffuse optical tomography.

In DOT, the optical properties of the biological tissues, primarily the absorption and the scattering coefficients, are reconstructed at different locations in the breast. The absorption coefficient at each pixel arises from the summation of the absorption of the different of chromophores or dyes at each pixel [45].

1.3.5.3. Biomagnetic Detection

In preliminary studies shown in [47-49], elevated magnetic fields were detected from malignant breast tumors in comparison to benign tumors. In [47], the biomagnetic fields from 11 patients with invasive breast carcinoma and ten with benign breast tumors were recorded. It was found that invasive breast carcinoma produced magnetic fields with higher magnitude and more fluctuations than benign tumors. On average, malignant tumors generated 754 fT, whereas benign tumors generated 274 fT in the 2–7 Hz frequency range [48]. By employing nonlinear chaotic analysis the classification of malignant and benign tumors was achieved. The results presented in [47-49] were highly preliminary in terms of the number of patients, the simplicity of the superconducting quantum interference device (SQUID) system used and the negligence of the other biomagnetic signals generated from the human body [50]. The detection of the biomagnetic fields generated from excitable organs such as the brain has emerged as an important diagnostic modality which is termed as magnetoencephalography (MEG). Recent developments in MEG include the

development of whole head MEG system with few hundred SQUID sensors [50]. Similarly, the development of SQUID systems with a large number of detectors arranged to conform to the shape of the breasts is anticipated to increase the accuracy of the biomagnetic detection of breast cancer.

1.3.5.4. *Microwave Imaging*

Microwave Imaging is another emerging technique for several biomedical imaging applications. Recent years have shown a dominant interest in microwave imaging technique for breast cancer detection. Microwave signals are the non-ionizing form of electromagnetic waves and thus do not incur health hazard when used at low levels. Microwave detection is less expensive and safer than other forms of detection and also noninvasive. For these reasons, this method has been increasingly recommended as a regular examination and detection tool for early breast cancer detection but it is under research and investigation stage till today.

The main motivation was the hypothesis that the electrical properties, permittivity and conductivity, of malignant breast tumors tissue differ significantly from those of the normal surrounding breast tissue. The difference was estimated to be almost five to ten times larger [51]. Cancerous tissues have permittivities and conductivities that are different than those of healthy breast tissues. Therefore, when an incident wave is exerted, cancerous tissue will scatter differently indicating their presence [52]. Microwave imaging has been employed in few clinical trials and it exhibited a minimum detected tumor size of 9–10 mm, and a preliminary accuracy of 80 per cent–90 per cent [4, 53-55]. There are many passive and active methods of the microwave technique.

The passive methods (microwave radiometry) use radiometers to measure the temperature differences in the breast as temperature increases in the presence of tumor than with healthy breast tissue [11]. Microwave radiometry is a functional imaging modality since it detects the elevated microwave emission due to the high activity of the tumor. The hybrid methods (microwave-induced acoustic imaging) use microwave energy to heat tumors. They expand and generate pressure waves which are detected by ultrasound transducers [12]. Currently, there are two main active methods involve illuminating the breast with microwaves and then measuring transmitted or backscattered signals; such as microwave

tomography [13] and radar-based imaging [8, 14-17]. In microwave tomography, a nonlinear inverse scattering problem is solved to reconstruct an image of the dielectric properties in the breast. The inverse scattering approach does not require any a priori information about the imaged object to produce the complex dielectric constant distribution. However, in practice it often faces difficulty in converging to the right solution due to the ill-conditioned non-linear problem it tackles [18]. In contrast to the image reconstruction aim of the microwave tomography technique, UWB radar-based imaging approach solves a simpler computational problem faster dealing with only to identify the presence and location of significant scattering obstacles such malignant breast tumors. The UWB microwave radar-based imaging technique specifically uses short duration pulses. Using a mechanical scanning sub-system, measurements are repeated for different locations of an UWB probe antenna (Figure 1.6). In the electronic equivalent, UWB array antenna with switched elements is used (Figure 1.7 and Figure 1.8). The UWB radar technique offers creation of an image, which can be formed by combining all of the signals (S_{ii} and S_{ij}, i≠j) coming from different antennas in a very short time [19-21].
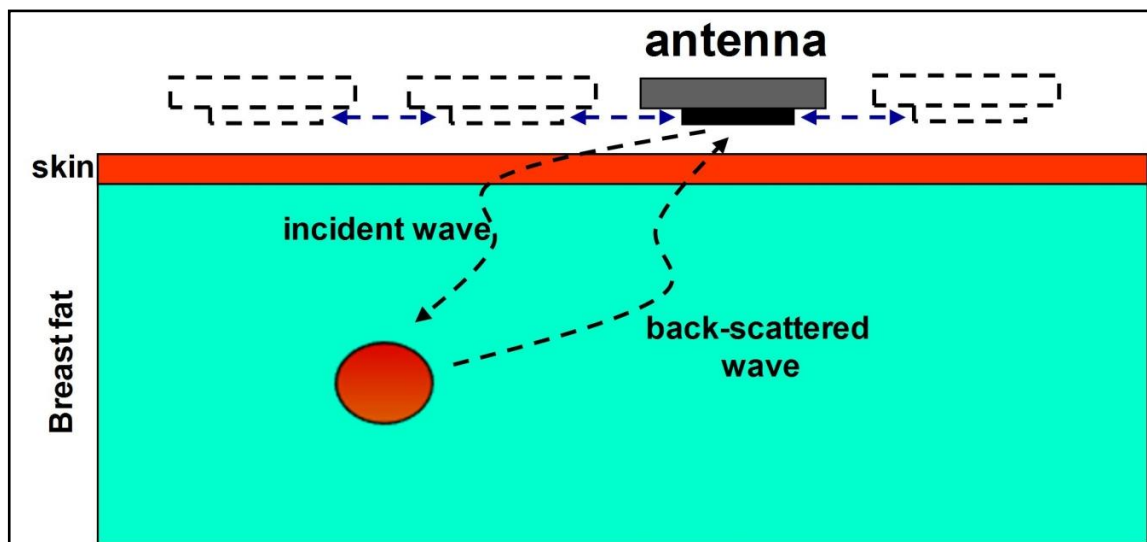
Figure 1.6. Schematic illustration of basic monostatic radar measurement system
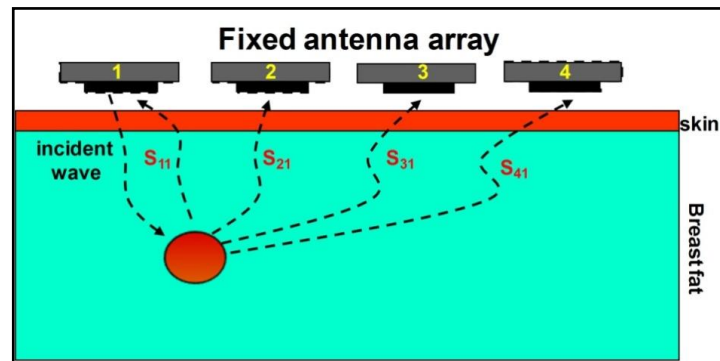
Figure 1.7. Schematic illustration of basic multistatic radar measurement system
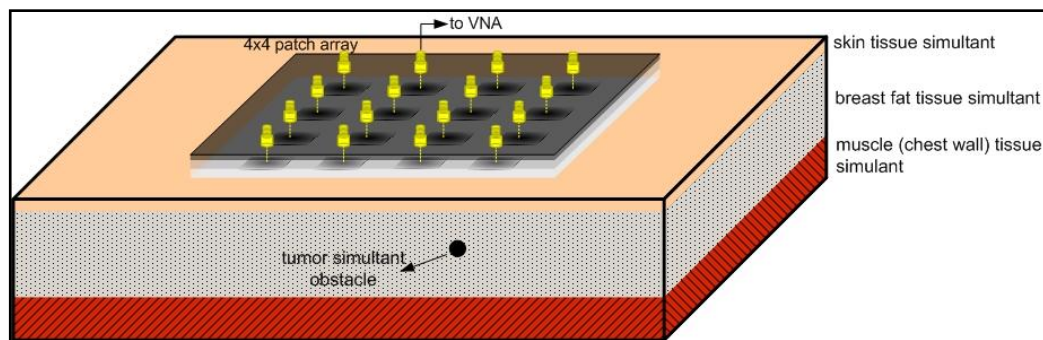
Figure 1.8. Schematic illustration of a basic multistatic radar measurement system with
4×4 microstrip patch antenna array

Over the past few years, several research groups have been working on both hardware and software aspects of microwave breast imaging to take advantage of the high contrast of healthy and malignant tissue at microwave frequencies. Several microwave imaging techniques have been suggested, including microwave tomography and confocal imaging (UWB imaging). UWB radar imaging, as proposed by Hagness et al. [56, 57] uses reflected UWB signals to determine the location of microwave scatters within the breast. This is a similar imaging procedure to that used in surface-penetrating radar rather than using the tomographic approach of reconstructing the entire dielectric profile of the breast. UWB radar imaging uses the Confocal Microwave Imaging (CMI) approach to identify and locate regions of scatterings within the breast [8, 14, 58-61]. A recent study of the dielectric properties of adipose, fibro-glandular and cancerous breast tissue has highlighted the dielectric heterogeneity of normal breast tissue [62]. The dielectric properties of normal

breast tissue being primarily homogeneous, found a very significant dielectric contrast between adipose (fatty) and fibro-glandular tissue within the breast.

The first near-field microwave imaging system used in clinical trials was developed at Dartmouth College by Meaney et al. [63, 64]. The system consisted of a circular antenna array of 32 monopoles operating in the frequency range 300–1000 MHz. The antenna array was positioned in a tank filled with saline to act as the coupling medium between the antennas and the breast. The patient lay in the prone position with her breast hanging, through an opening in the table, into the tank where the antennas were immersed. The antenna array moved vertically, in 1 cm steps, through a mechanical jack to acquire measurement from the chest level down to the nipple. A microwave switching system was used to select which antenna transmits the power from the microwave source and which antenna sends its received power to the receiver.

An UWB microwave imaging system was developed by Klemm et al. at the University of Bristol [15-17, 54]. In comparison to the system of Meaney et al., this system operated at higher frequencies (3-10, 4-8, 4.5-9.5 GHz) which were achieved by employing different very small UWB antennas in a hemi-sphere array encircling the breast, instead of using monopole antennas. Since there are a lot of microwave imaging systems under development for breast cancer detection, detailed comparisons of those recent developed experimental microwave imaging systems are given in Table 1.2. In all the systems, there are also no pictorial 3D representations of the tumor size. More work needed to be conducted in real time with real patients in terms of clinical tests, too.

Finally; if one compares the imaging methods, there are various imaging algorithms used in different systems (Table 1.2). Especially for UWB radar imaging, the simple sum-and-time-shift techniques (DAS) do not allow for compensation of frequency-dependent propagation effects, such as dispersion, and offer limited capability for discriminating against artifacts and noise [20]. One can compensate for these frequency-dependent propagation effects by using a broadband beamformer called the MIST beamformer [14, 24, 25]. MIST technique uses a data-independent algorithm to overcome the effects of frequency dependent propagation, as well as, to outperform mono-static DAS, although multi-static DAS still outperforms mono-static MIST [15]. A new data-adaptive algorithm

for breast cancer detection called MAMI has been proposed [27], which is based on robust Capon beamforming (RCB) [26]. MAMI algorithm provides better performance than multistatic DAS and MIST, as shown in Figure 1.9 [15, 28].

Table 1.2. Comparison of recent developed experimental microwave (tomography and radar-based) imaging systems for breast cancer detection

Project Head	University	Antenna	# of Antennas	Imaging Method	Clinical Trial	Tumor Size (dia.)	Measur. Speed	Frequency
Meaney [63, 64]	Dartmouth, 2000, 2011	Monopole (Multifreq CW)	16	2D Inversion Methods, 3D (2011)	Exists	130 subjects, > 1 cm	15 min. Scan	500 MHz-3 GHz
Hagness [24]	Wisconsin 2004	UWB Pyramidal Horn (pulsed)	Single element scanned 49 positions	(MIST) combined with statistical methods (GLRT).	-	4 mm (depth: 2cm)	-	1-11 GHz
Fear [65]	Calgary, 2005	UWB Wu-King Monopole (pulsed)	rotation of phantom around antenna	Tissue Sensing Radar (TSAR), MIST.	-	Exper. (1 cm), simula-tions (4 mm)	-	1-10 GHz
Klemm [54]	U. of Bristol, UK, 2008	Stacked Patch (pulsed)	4x4 (16 conformal array)	Delay and Sum Beam-forming	Exists	4 mm, 10 mm	-	4.5-9.5 GHz
Liu [66]	Duke U., 2008	Bow-Tie Patch (CW)	36	DTA-BIM, BSGS-DBIM	-	< 5 mm	<2 min. scan	2.7 GHz
Klemm [15, 54]	U. of Bristol, UK, 2009	Stacked Patch (pulsed)	31 elements-conformal array	Delay and Sum Beam-forming	Exist (9, 15, 20, 30 mm dia. tumors)	6 mm, 7 mm, 10 mm	90 sec.	3-10 GHz
Rubaek & Zhur-benko [67]	Tech. U. of Denmark, 2009	Horizontally aligned mono-poles	32	Frequency-domain inverse scattering	-	< 5 mm	2 min.	300 MHz-3 GHz
Bialkow-ski & Abbosh [68]	U. of Queensland, Australia, 2010	UWB Tapered Slot Antenna (pulsed)	12 (cylind. array)	Rotation method /back-ground subtraction	-	4 mm	by an additional movement <15 sec.	3-11 GHz

Table 1.2. Comparison of recent developed experimental microwave (tomography and radar-based) imaging systems for breast cancer detection (continue)

Project Head	University	Antenna	# of Antennas	Imaging Method		Tumor Size (dia.)	Measur. Speed	Frequency
Klemm [17]	U. of Bristol, UK, 2011	Wide Slot (pulsed)	60 elements-conformal array	Delay and Sum Beam-forming	-	no info.	10 sec.	4-8 GHz
Bahattin Türetken & İlhami Ünal [69]	TUBİ-TAK-BİLGEM-UEKAE (ATAM), 2011/2013	(pulsed) Stacked Patch / Vivaldi Antenna / Conformal Bow-tie	scanned for 361 positions / 18 positions/ 7 elements	Raw Data / DAS Algorithm	-	20 mm / 10 mm / 2 mm (by simulation)	Manually scanned & Array Antennas	4.6-5.25 GHz / 5-10 GHz / 1-8 GHz
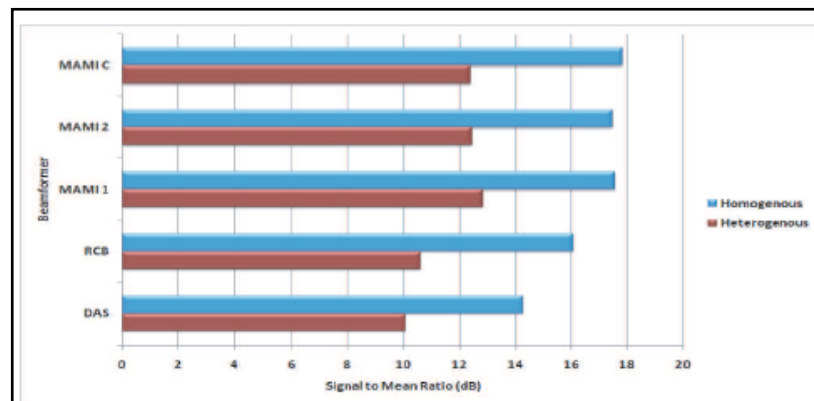
Figure 1.9. Signal to mean (S/Mn) ratio results for each beamformer [28]

1.4. CONTRIBUTION AND OUTLINE OF THIS DISSERTATION

The main goal of this study is making a contribution to the recent microwave imaging systems under developed for breast cancer detection, from antenna design point of view. All of the systems (Table 1.2) are intended to develop a perfect microwave imaging system replacing especially X-ray mammography technology (Figure 1.10) [54].

In addition to the development of experimental systems (Table 1.2), extensive research was performed to advance the antennas, which are the sensors for the microwave imaging

modality. Desired characteristics of these antennas were UWB, compact size, steerable, dual independent linear polarization, isolation from nearby interference, and high radiation efficiency [4]. Several different types of antennas have been considered and reported over the past decade by research groups involved in radar-based UWB breast imaging; such as UWB planar bow-tie [70], ridged pyramidal horn [24], cross-polarized types [71, 72], U-slot [73, 74], antipodal Vivaldi [75], stacked microstrip patch [69, 74], tapered slot [7], dielectric resonator antennas [4], and MEMS-steerable antennas [4], etc. These antennas were generally used and tested in planar, cylindrical or spherical scanning surfaces, as a single element or in an antenna array.
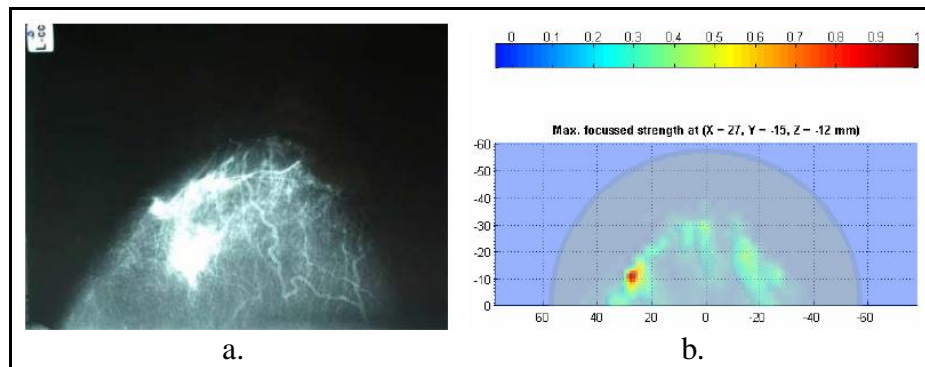
Figure 1.10. Comparison of the clinical imaging results: a. X-ray mammogram, b. radar-based UWB microwave system [54]

Most of the mentioned antennas require a matching liquid to reduce the mismatch between the antenna and the skin layer, such as soybean oil, canola oil, blous saline solutions, alcohol, mixtures of glycerin and water, etc. However, in this study for the simulations, since the skin reflections back to the antenna adversely affect imaging results, better penetration of electromagnetic waves into the breast tissue will be determined by operating the antenna in a coupling medium whose dielectric properties are close to the breast tissue, for simplicity.

Although an antenna array system is applicable and mostly preferred for real breast tumor detection systems, mutual coupling effects between array elements would certainly affect the measurement results [76]. If one antenna element of the array sends UWB electromagnetic waves through the breast, unwanted currents are induced on the nearby

antenna elements which results distortion of the measurement results (Figure 1.11). One can solve the problem by separating the antenna elements as far as possible; however we're limited with the breast surface! There are also some mutual coupling suppression techniques, too [77]. These suppression methods need some additional microwave circuitry such as phase shifters, attenuators, etc. However, that would increase the hardware of the system as well as mechanical parts and connections of the antenna array system. In order to detect the weak reflections from small tumors located in tissues ranging from fatty breast to glandular, a high sensitive antenna is required to send and receive electromagnetic waves with low pulse distortion and low mutual coupling effects in the array. Since antennas are assumed to be operating in the near field region in which spherical waves exist, antenna geometry and polarization should be appropriately selected to perfectly match with the spherical waves inside the breast, too [78].
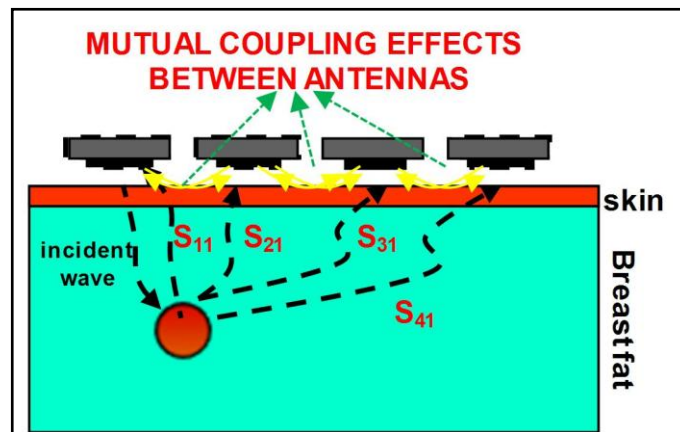
Figure 1.11. Schematic illustration of mutual coupling effects in a basic multistatic radar measurement system

For this purpose, this dissertation mainly presents herein spherical conformal bow-tie antennas to improve tumor detection capability of the microwave imaging system. Conventional planar UWB bow-tie antennas are curved onto a hemi-sphere surface to investigate its effects on enhancement of tumor responses and signal energies, as well as that of mutual coupling levels between array elements and pulse distortion performance. First ideal draft writings and drawings of this study (based on conformal antenna structures and isolation of signals of nearby antennas) can be seen in Figure 1.12, too.

For getting higher resolution results, number of antenna elements should be as many as possible, as well as with the operation of very wide operation frequency region. However, increased number of antennas would be at the expense of an increased mutual coupling which would adversely affect return losses and pulse fidelity [18]. On the other hand, one can decrease the antenna dimensions for using more antennas in the antenna array, by increasing the lower limit of the wide operation frequency range. However, increasing the frequency will lead to decreasing the penetration depth. Therefore, there must be a balance between reasonable contradictory needs of better spatial resolution, better penetration depth [73], less attenuation of electromagnetic waves through the breast and smaller dimensions of a multi-function active imaging system. Therefore, UWB microwave imaging technique is used in the 1–8 GHz frequency range for the operation of the spherical conformal bow-tie antenna.
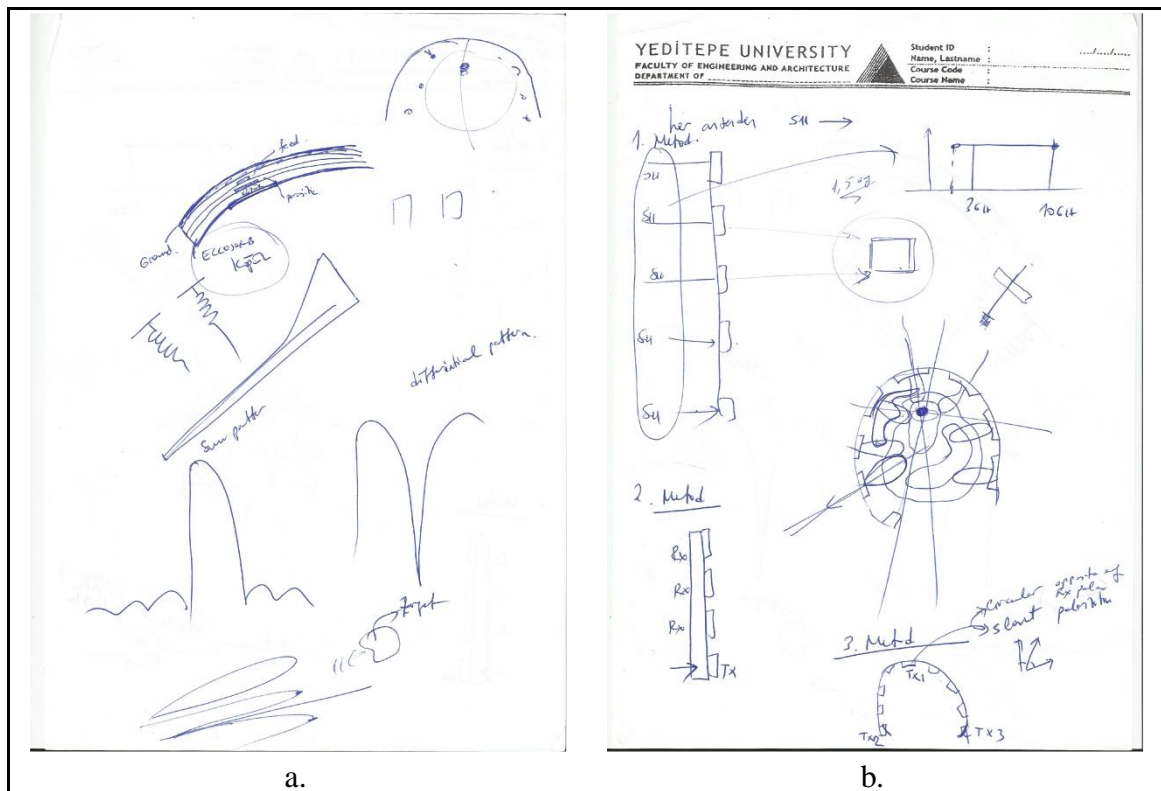
Figure 1.12. First ideal draft writings and drawings by Assoc. Prof. Dr. Bahattin Türetken before starting the Ph.D. thesis, two and a half years ago

Moreover, the main design criteria for a practical microwave imaging systems should be as follows:

- Maximum antenna elements in the array (with smallest antenna size),

- Minimum mechanical connections and parts for the system,

- Minimum mutual coupling effects between antenna array elements,

- Best fidelity characteristics of the antennas for low pulse distortion through the breast,

- Fast and powerful imaging algorithm,

- Minimum resolution result for tumor, as low as possible,

- Maximum Signal/Clutter (S/C) ratio, as much as possible,

- There must be no need for background measurements for early effect (skin reflections and incident wave) removal,

- Avoiding skin reflections by using a matching or coupling medium between breast and antenna, or an alternative method,

- Construction of realistic breast phantom models,

- Abilities to detect tumors hidden behind the glands,

- Compensation of frequency dispersive effects of breast medium for imaging algorithms.

This dissertation is organized as follows: Analytical and numerical preliminary works are given with comparisons as infrastructure studies, in Section 2. In Section 3, a preliminary experimental work is introduced with numerical comparisons, followed by a numerical analysis study of electromagnetic immunity of a microwave imaging system with spherical conformal circular microstrip patch antennas for people who use pacemakers. Section 4 presents the novel spherical conformal bow-tie antenna with the findings related to the enhancement of tumor responses, fidelity and mutual coupling effects of array elements with comparative results, in details. Finally, a monostatic radar-based experimental measurement system by using Vivaldi antennas, as well as preliminary simulation results are briefly introduced with imaging results, in Section 5.

2. ANALYTICAL AND NUMERICAL INVESTIGATIONS

2.1. DISPERSIVE DIELECTRIC PROPERTIES OF BREAST AND TUMOR TISSUES

Electrical parameters of the biological bodies in the human body models are assumed to be dispersive. Frequency dependent complex dielectric constant can be expressed by Debye relation in the following form.

$$\varepsilon_r(\omega) = \varepsilon_r{}' - j\varepsilon_r{}'' = \varepsilon_{r\infty} + \frac{\varepsilon_{rs} - \varepsilon_{r\infty}}{1 + j\omega\tau} \tag{2.1}$$

$$\varepsilon_r{}' = \varepsilon_{r\infty} + \frac{\varepsilon_{rs} - \varepsilon_{r\infty}}{1 + (\omega\tau)^2} \tag{2.2}$$

$$\varepsilon_r{}'' = \frac{\omega\tau\left(\varepsilon_{rs} - \varepsilon_{r\infty}\right)}{1 + (\omega\tau)^2} \tag{2.3}$$

Dispersive complex conductivity is defined as

$$\sigma^* = \left(\sigma_s + \omega\varepsilon_r{}''\right) \tag{2.4}$$

$$\sigma^* = \sigma_s + \frac{\omega^2\tau\left(\varepsilon_{rs} - \varepsilon_{r\infty}\right)}{1 + (\omega\tau)^2} \tag{2.5}$$

where, $\varepsilon_r{}'$ and $\varepsilon_r{}''$ represents real and imaginary part of relative permittivity, respectively and σ_s is low frequency value of conductivity; $\varepsilon_{r\infty}$ and ε_{rs} are the relative permittivity at high and low frequency range, respectively, and τ is the relaxation time and $\omega = 2\pi f$ is the angular frequency in the dispersion region. The time variation $e^{j\omega t}$ is used everywhere.

In general, permittivity and conductivity of homogenous and isotropic dielectrics are functions of frequency. In dielectric media, particularly at high frequencies, the property of dispersiveness can be observed. Imaginary part of relative permittivity, $\varepsilon_r^{''}$, has its maximum value at $\omega = \omega_0$ (Figure 2.1). For this reason, the frequency at which ω equals to ω_0 is called the resonance frequency of the medium. There can be more than one resonance for a medium. Four types of resonances are depicted in Figure 2.2. At the angular frequencies ω_{on} (with $n = 1, 2, 3, 4$) of a medium, the attenuation constant becomes very large, and conductivity has its maximum at these frequencies. It is clear that the imaginary part of the permittivity is associated with power loss or dissipation within the dielectric.
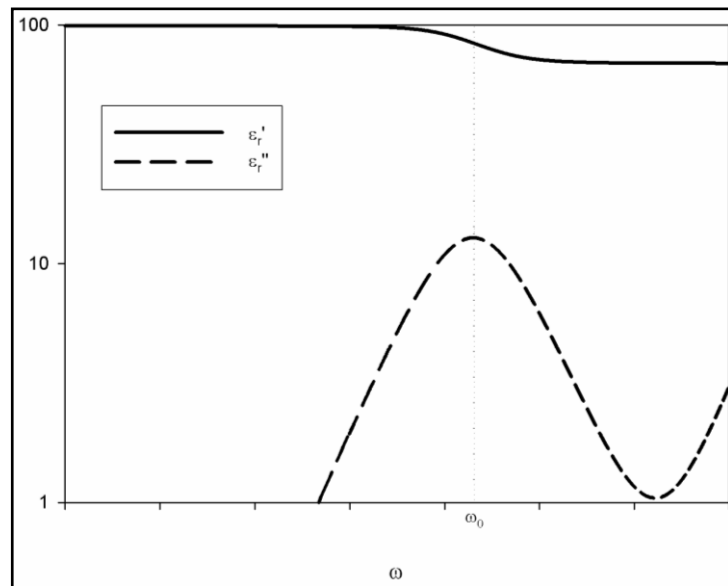
Figure 2.1. Resonance frequency-ω_o (based on the data of vitreous humour tissue)

The electrical parameters of biological tissues under consideration can also be evaluated using a slightly more general form of Debye relations to take into account the presence of a distribution of relaxation times, known as Cole-Cole approximations [79] given below:

$$\varepsilon_r\left(\omega\right) = \varepsilon_{r\infty} + \sum_{n=1}^{4} \frac{\Delta\varepsilon_{rn}}{1+\left(j\omega\tau_n\right)^{\alpha_n}} \tag{2.6}$$

where $\Delta\varepsilon_{rn}$ are the differences of relative permittivity between high and low frequencies, τ_n is the relaxation time, with $0 < \alpha_n < 1$ providing a measure of relaxation time distribution and $\omega = 2\,\pi\,f$ is the angular frequency in the nth dispersion regions.
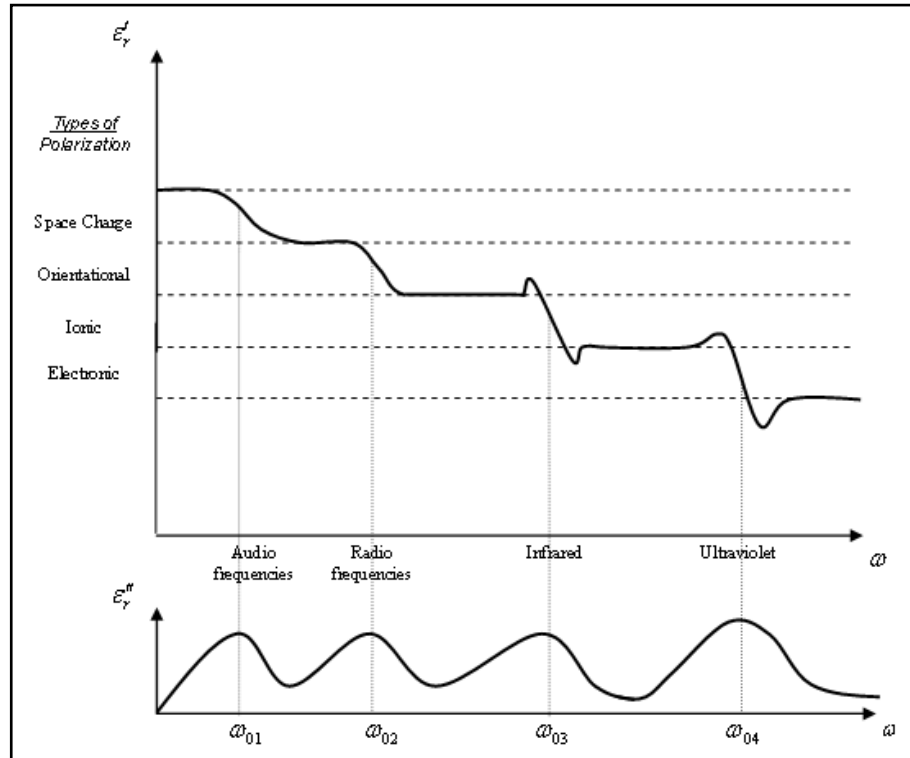
Figure 2.2. Four types of resonances

The dielectric properties of breast and tumor tissues, as well as coupling medium, at constant frequencies are given as follows:

Table 2.1. Dielectric properties of breast fatty tissue at constant frequencies

Reference	ε_r	σ^*	frequency
[70, 80]	9	0.4	3 GHz
[73]	9.8	0.4	6 GHz
[22]	9	0.4	no info.
[81]	9	0.4	no info.
[16] (phantom)	10	1.2dB/cm atten.	6 GHz
[60]	9	0.4	-

Table 2.2. Dielectric properties of skin tissue at constant frequencies

Reference	ε_r	σ^*	frequency
[15]	36	4	no info.
[73]	34.7	3.89	6 GHz
[22]	36	4	no info.
[25]	36	4	no info.
[16] (phantom)	30	16dB/cm atten.	6 GHz
[60]	36	4	-

Table 2.3. Dielectric properties of fibro-glandular tissue at constant frequencies

Reference	ε_r	σ^*	frequency
[73]	21.5	1.7	no info.
[60]	11-15	0.4-0.5	-

Table 2.4. Dielectric properties of ducts at constant frequencies

Reference	ε_r	σ^*	frequency
[73]	37.96	4.5	no info.

Table 2.5. Dielectric properties of chest wall at constant frequencies

Reference	ε_r	σ^*	frequency
[73]	55.56	6.5	no info.
[60]	50	7	-

Table 2.6. Dielectric properties of nipple at constant frequencies

Reference	ε_r	σ^*	frequency
[73]	45	5	no info.
[60]	45	5	-

Table 2.7. Dielectric properties of tumor tissue at constant frequencies

Reference	ε_r	σ^*	frequency
[80]	50	7	3 GHz
[73]	50.7	4.8	6 GHz
[22]	50	4	no info.
[16] (phantom)	50	7	6 GHz
[71]	50	7	2-4 GHz

Table 2.8. Dielectric properties of coupling medium at constant frequencies

Reference	ε_r	σ^*	frequency
[80]	9	0.2	3 GHz
[75]-canola oil	2.5	0.04	1-14 GHz
[82]	9	0	no info.
[16] (phantom)	10	1.2dB/cm atten.	6 GHz
[60]	9	0	-
[70]	9	0.4	-
[71]	9	0.2	2-4 GHz

The dispersive dielectric properties of breast and tumor tissues, as well as coupling medium, in terms of first order Debye model parameters are also given as follows:

Table 2.9. Debye model parameters in [14]

Tissue	$\varepsilon_{r\infty}$	ε_{rs}	τ (ps)	σ_s (S/m)
Skin	4	48	8	0.5
Breast Fat	7	10	7	0.15
Tumor	4	54	7	0.7

Table 2.10. Debye model parameters of coupling medium in [75]

Tissue	$\varepsilon_{r\infty}$	ε_{rs}	τ (ps)	σ_s (S/m)
Canola Oil	2.28	2.514	27.84	0.008

Table 2.11. Debye model parameters in [83]

Tissue	$\varepsilon_{r\infty}$	ε_{rs}	τ (ps)	σ_s (S/m)
Skin	4	44.5	7.96	0.5
Pork fat	2.938	5.84	12.9	0.086
Breast	7	10	7	0.15

Table 2.12. Debye model parameters in [7]

Tissue	$\varepsilon_{r\infty}$	$\varepsilon_{rs}-\varepsilon_{r\infty}$	τ (ps)	σ_s (S/m)
Gland tissue	12.8485	24.643	13	0.2514
Fat tissue	3.987	3.5448	13	0.0803

Table 2.13. Debye model parameters in [84]

Tissue	$\varepsilon_{r\infty}$	$\varepsilon_{rs}-\varepsilon_{r\infty}$	τ (ps)	σ_s (S/m)
Tumor	4	54	7	0.4
Normal breast tissue	7	10	7	0.15

2.2. DETERMINATION OF DIELECTRIC MEDIUM PARAMETERS AND THICKNESSES OF *N*-LAYERED LOSSY MEDIA

A theoretical microwave technique for determination of unknown medium parameters (ε, μ, σ) and unknown thicknesses of *N*-layered lossy media has been presented in this sub-section. Since one knows the exact analytical expression of reflection coefficient of the *N*-layered planar lossy media, unknown parameters can be solved in reverse order. For

different operation frequencies and different angle of incidences, measured (or obtained) data can be increased to determine the unknown thicknesses and medium parameters.

2.2.1. Calculation of Reflection Coefficient of the *N*-Layered Planar Lossy Media

One can easily write transverse electric (TE) field equations in terms of unknown coefficients such as R_0, T_1, R_1, ..., T_N, R_N, as follows (See Figure 2.3):
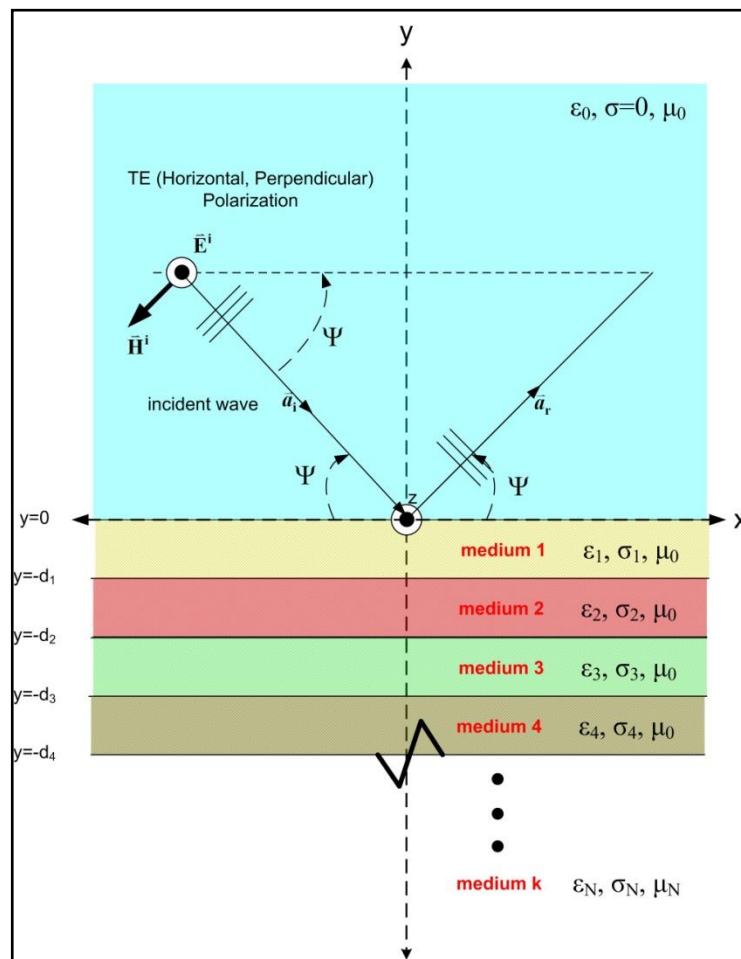
Figure 2.3. Schematic illustration of *N*-layered planar lossy media

$$\mathbf{E}_0 = \boldsymbol{a}_z \left(e^{-jk_0\left(x\cos(\psi)-y\sin(\psi)\right)} + R_0\, e^{-jk_0\left(x\cos(\psi)+y\sin(\psi)\right)} \right) \tag{2.7}$$

$$\mathbf{E}_1 = \boldsymbol{a}_z \left(T_1\, e^{-jk_1\left(x\cos(\theta_{t1})-y\sin(\theta_{t1})\right)} + R_1\, e^{-jk_1\left(x\cos(\theta_{t1})+y\sin(\theta_{t1})\right)} \right) \tag{2.8}$$

$$\mathbf{E}_2 = \boldsymbol{a}_z \left(T_2 \, e^{-jk_2\left(x\cos(\theta_{t2})-y\sin(\theta_{t2})\right)} + R_2 \, e^{-jk_2\left(x\cos(\theta_{t2})+y\sin(\theta_{t2})\right)} \right) \tag{2.9}$$

$$\mathbf{E}_N = \boldsymbol{a}_z \left(T_N \, e^{-jk_N\left(x\cos(\theta_{tN})-y\sin(\theta_{tN})\right)} \right) \tag{2.10}$$

The unknown coefficients are calculated (in a matrix form) by applying boundary conditions (continuity of tangential components of both electric and magnetic fields) and Snell's relations at each boundary. The total reflection coefficient corresponds to R_0.

R_0 can also be calculated by using different methods. As an example, for a normal incidence case, one can use multiple reflections [85] to calculate the total reflection coefficient for $N=2$ layered planar lossless media, as shown in Figure 2.4.
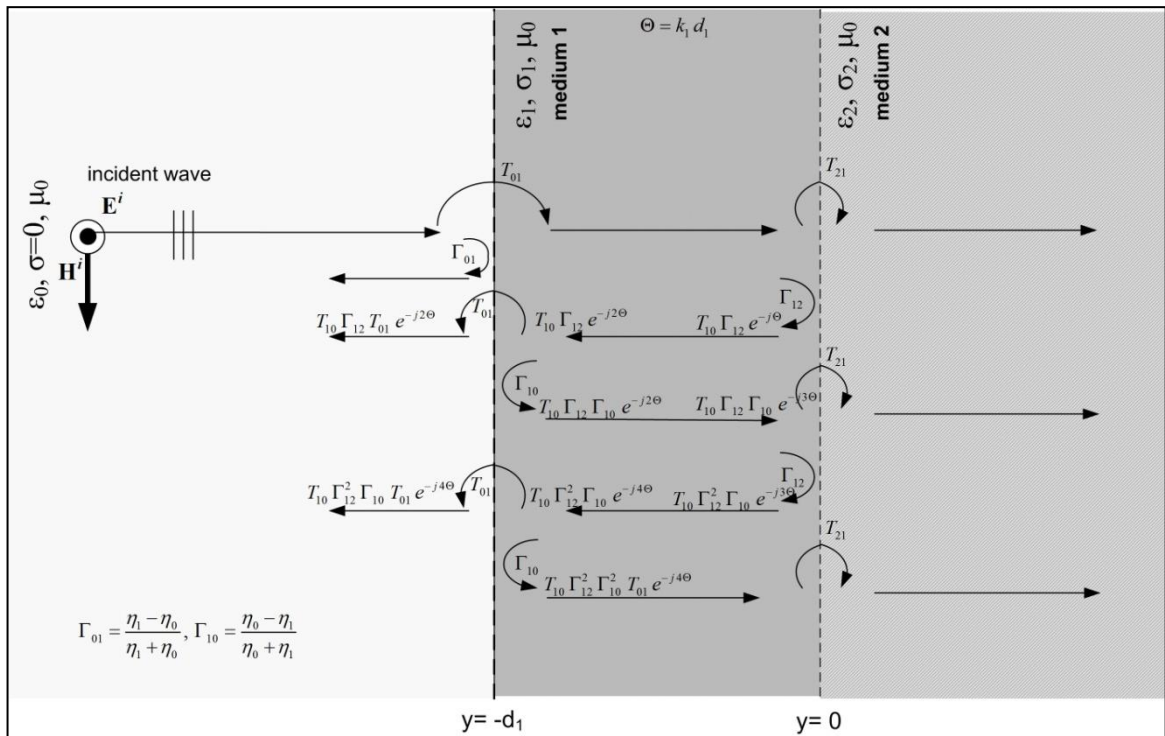
Figure 2.4. Schematic illustration of multiple reflections for normal incidence case ($N=2$ layered planar lossless media)
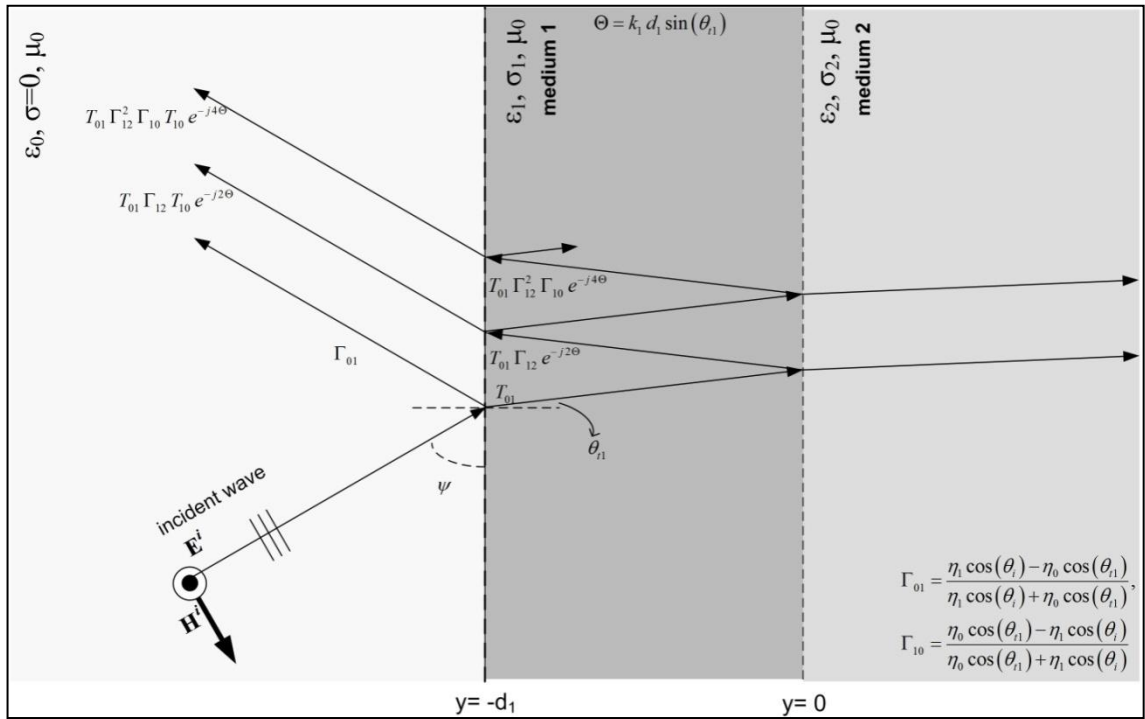
Figure 2.5. Schematic illustration of multiple reflections for angular incidence case ($N=2$ layered planar lossless media)

An iterative calculation method is also explained by J. R. Wait in [86], for normal incidence case, as follows:

$$R_0 = \frac{N_0 - Y_1}{N_0 + Y_1} \tag{2.11}$$

where

$$Y_n = N_n \frac{Y_{n+1} + N_n \tanh(u_n d_n)}{N_n + Y_{n+1} \tanh(u_n d_n)}, \; for \; n = 1,2,3,...,N-1 \tag{2.12}$$

$$Y_N = N_N \tag{2.13}$$

$$N_n = \frac{u_n}{j \mu_n \omega}, \quad u_n = \left(1 - \frac{k_0^2}{k_n^2} \cos^2(\psi)\right)^{1/2} \tag{2.14}$$

One can also drive manually an iterative relation in terms of a correction factor (Q) for angular incidence case for $N=3$ layered planar lossy media, as follows:

$$R_0 = e^{-2jk_0(d_0 \sin(\psi))} \frac{\left[1 + \frac{\sin(\theta_{t1})}{\eta_1} \frac{\eta_0}{\sin(\psi)} Q\right]}{\left[1 - \frac{\sin(\theta_{t1})}{\eta_1} \frac{\eta_0}{\sin(\psi)} Q\right]}$$

(2.15)

where

$$Q = \frac{\left[e^{+jk_1(d_0\sin(\theta_{t1}))} \frac{e^{-jk_1(d_1\sin(\theta_{t1}))}}{2} \kappa_{ps+} - e^{-jk_1(d_0\sin(\theta_{t1}))} \frac{e^{+jk_1(d_1\sin(\theta_{t1}))}}{2} \kappa_{ps-}\right]}{\left[e^{+jk_1(d_0\sin(\theta_{t1}))} \frac{e^{-jk_1(d_1\sin(\theta_{t1}))}}{2} \kappa_{ps+} + e^{-jk_1(d_0\sin(\theta_{t1}))} \frac{e^{+jk_1(d_1\sin(\theta_{t1}))}}{2} \kappa_{ps-}\right]}$$

(2.16)

$$\kappa_{ps+} = \left[P + \frac{\sin(\theta_{t2})}{\eta_2} \frac{\eta_1}{\sin(\theta_{t1})} S\right]$$

(2.17)

$$\kappa_{ps-} = \left[P - \frac{\sin(\theta_{t2})}{\eta_2} \frac{\eta_1}{\sin(\theta_{t1})} S\right]$$

(2.18)

$$P = \left[e^{+jk_2(d_1\sin(\theta_{t2}))} e^{-2jk_2(d_2\sin(\theta_{t2}))} \kappa + e^{-jk_2 d_1 \sin(\theta_{t2})}\right]$$

(2.19)

$$S = \left[e^{+jk_2(d_1\sin(\theta_{t2}))} e^{-2jk_2(d_2\sin(\theta_{t2}))} \kappa - e^{-jk_2 d_1 \sin(\theta_{t2})}\right]$$

(2.20)

$$\kappa = \frac{\left[\frac{\sin(\theta_{t2})}{\eta_2} - \frac{\sin(\theta_{t3})}{\eta_3}\right]}{\left[\frac{\sin(\theta_{t2})}{\eta_2} + \frac{\sin(\theta_{t3})}{\eta_3}\right]}$$

(2.21)
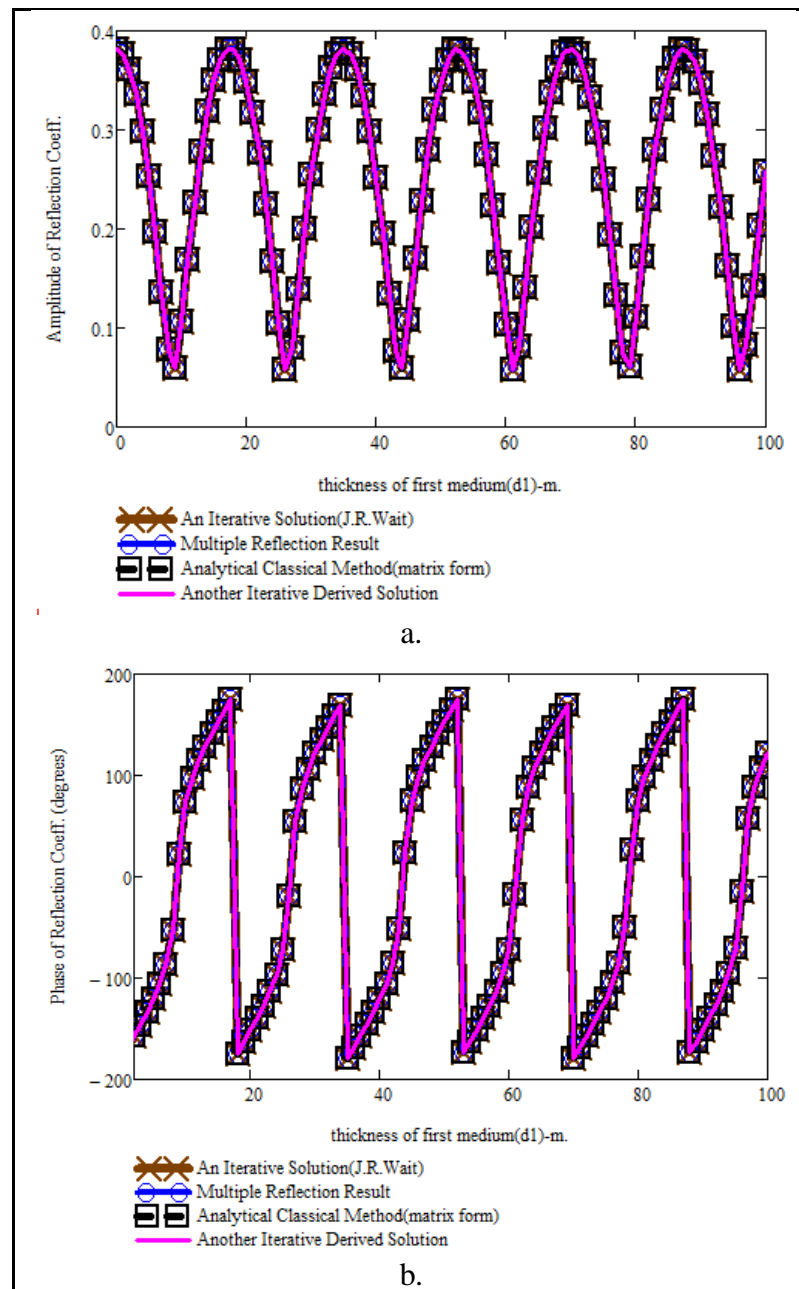
Figure 2.6. a. Amplitude and b. phase variations of reflection coefficient for normal incidence, with respect to thickness of d_1 for different calculation methods, with 100 MHz operation frequency, and $\varepsilon_{r1}=5$, and $\varepsilon_{r2}=2$
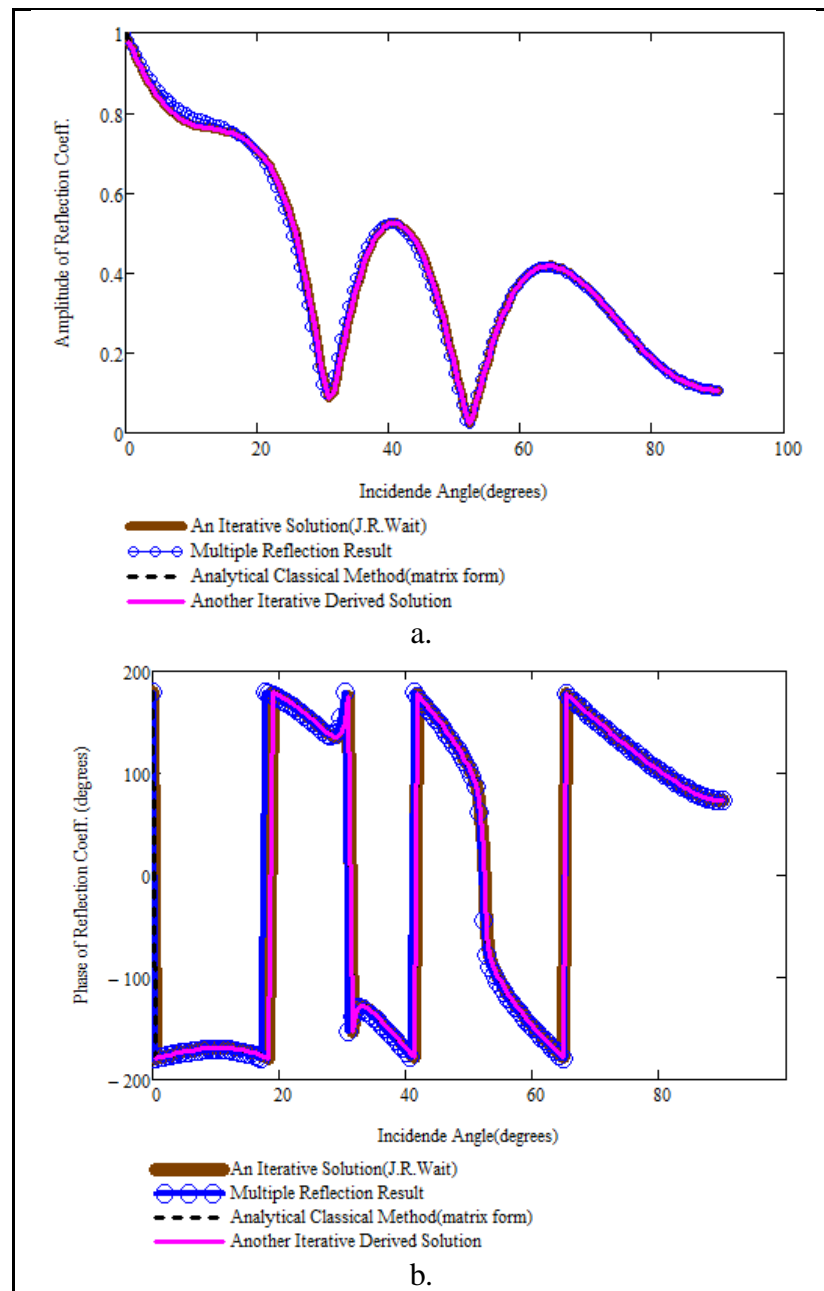
Figure 2.7. a. Amplitude and b. phase variations of reflection coefficient with respect to incidence angle for different calculation methods, with 100 MHz operation frequency, $d_1=10$ m, and $\varepsilon_{r1}=5$, and $\varepsilon_{r2}=2$

Figure 2.6 and Figure 2.7 show that all of the calculation methods give exactly same results. Therefore, one can use the derived analytical classical method (matrix form) for calculation of reflection coefficient of any N-layered planar lossy media. These relations can also be extended for transverse magnetic (TM) mode, too. For $N=2$ layered planar lossy media case, the following parameters are selected as $\varepsilon_{r1}=50$, and $\varepsilon_{r2}=1$, and $\psi=40^{o}$
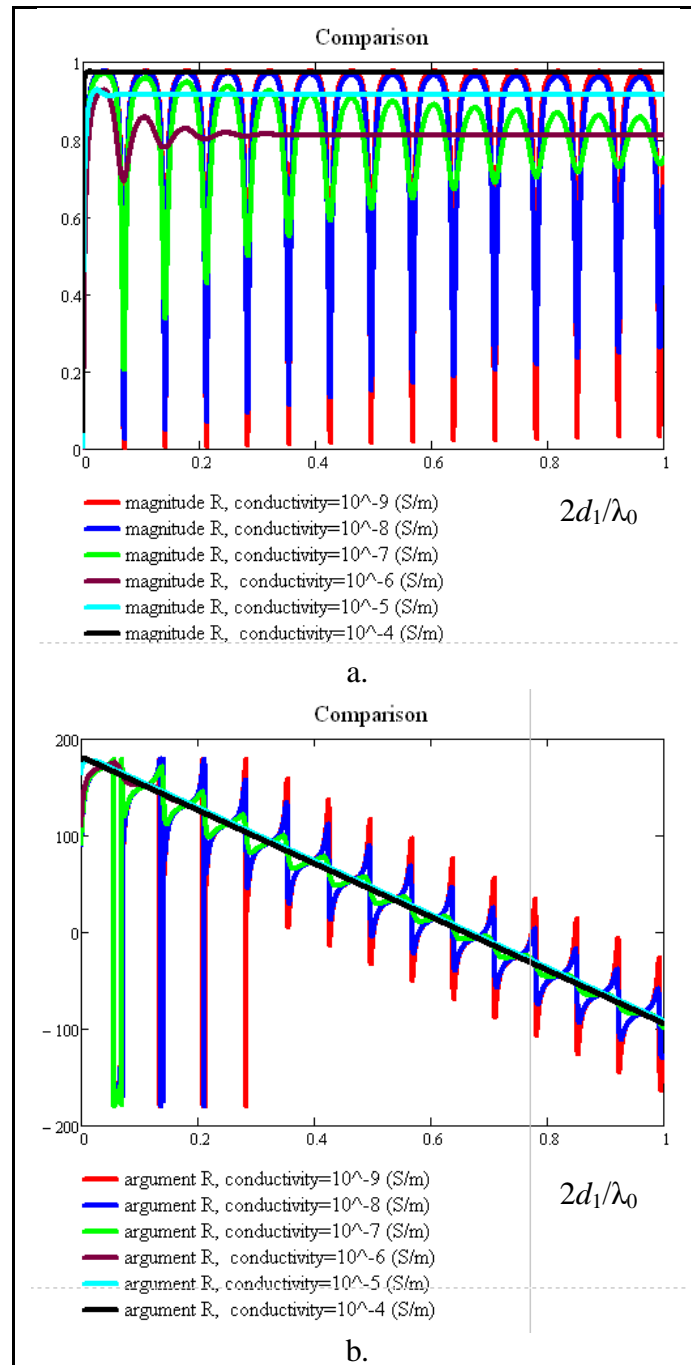
(Figure 2.8).

Figure 2.8. a. Amplitude and b. phase (argument) variations of reflection coefficient (R_0) with respect to ($2d_1/\lambda_0$) for different conductivities of lossy medium$_2$

2.2.2. Determination of the Unknown Thickness of the Slab from Amplitude and Phase Information of Reflected Waves
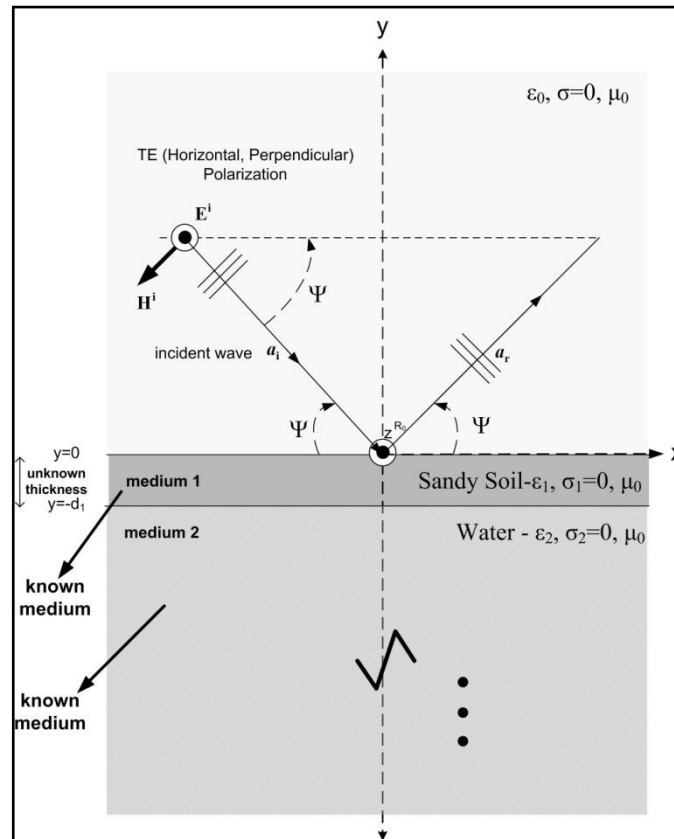
Figure 2.9. Schematic illustration of the problem for the unknown thickness d_1 ($\varepsilon_{r1}=2.548$, and $\varepsilon_{r2}=78.36$)

Analysis of the problem, as shown in Figure 2.9, would be helpful for determining the depth of the water resource that we're looking for, under the sandy soil ground which is also assumed to be planar. In this case, we'd like to investigate the thickness d_1 as an unknown parameter. For $N=2$, if one sweeps amplitude of the calculated reflection coefficient (R_0) with respect to d_1 up to 4.5 m depth, as shown in Figure 2.10, one can obtain 10 different possible d_1 values (0.31481 m, 0.62693 m, 1.243 m, 1.576 m, 2.2037 m, 2.5 m, 3.124 m, 3.444 m, 4.06 m, 4.3889 m) for the calculated reflection coefficient amplitude with ($d_1=2.5$ m). That calculated magnitude value (0.652) of R_0 is expected to be measured in the practical case.
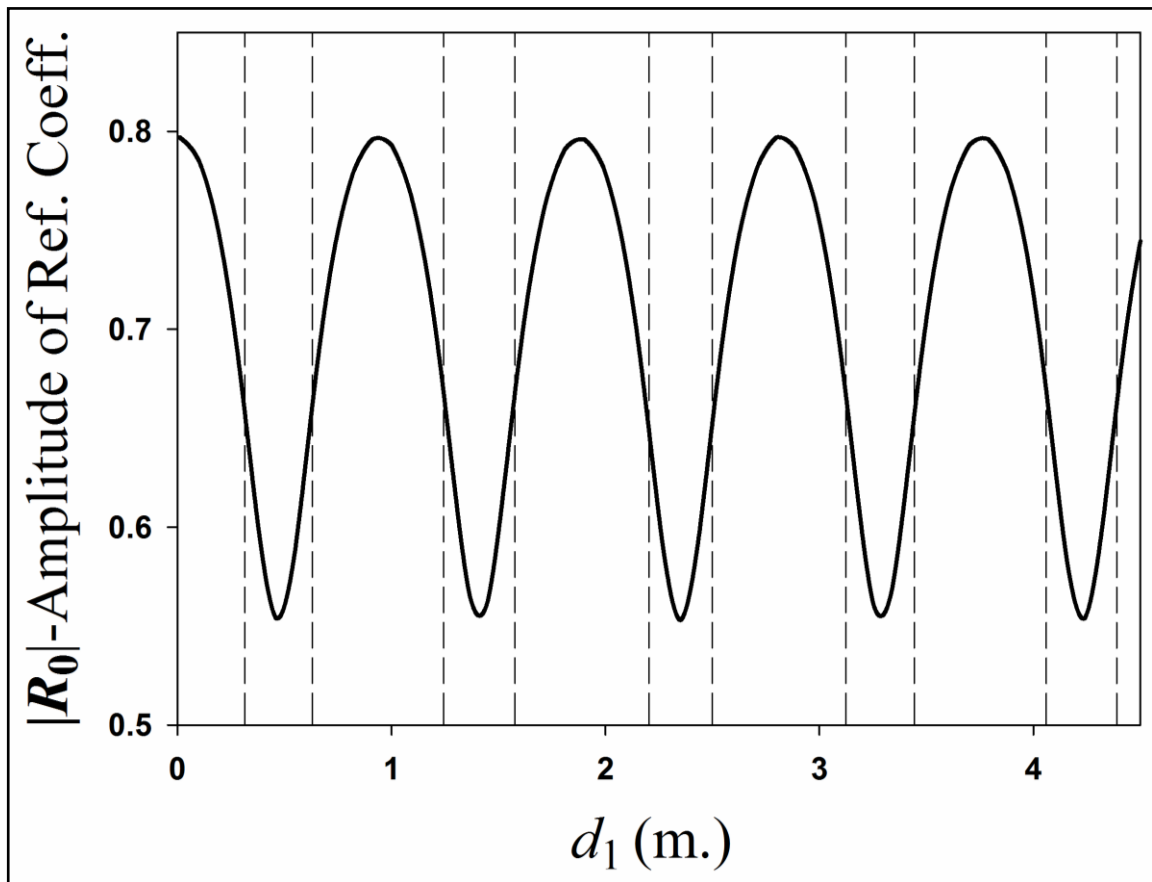
Figure 2.10. Amplitude of the calculated reflection coefficient (R_0) with respect to d_1, for 100 MHz operation frequency and normal incidence case

If one sweeps phase of the calculated reflection coefficient (R_0) with respect to d_1 up to 4.5 m depth, as shown in Figure 2.11, different possible common d_1 values decrease down to four (0.62693 m, 2.5 m, 3.444 m, 4.3889 m) for the calculated reflection coefficient phase with (d_1=2.5 m). That calculated argument value (-85.726°) of R_0 is expected to be measured in the practical case.

Then, the operation frequency is changed as 150 MHz. If one sweeps phase of the calculated reflection coefficient (R_0) with respect to d_1 for 150 MHz, different possible common d_1 values decrease down to three (0.62693 m, 2.5 m, 4.3889 m). Finally, different possible common d_1 values decrease down to only one (2.5 m), if one continues sweeping for 140 MHz. Therefore, the unknown thickness is obtained as 2.5 m by increasing the operation frequency and analyzing both amplitude and phase of the reflection coefficient.
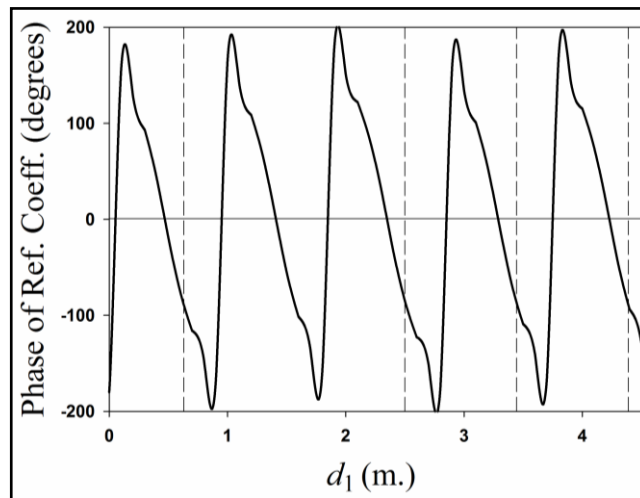
Figure 2.11. Phase of the calculated reflection coefficient (R_0) with respect to d_1, for 100 MHz operation frequency and normal incidence case

2.2.3. Determination of the Thickness of the Slab and Dielectric Constant of the Underground Medium from Amplitude and Phase Information of Reflected Waves
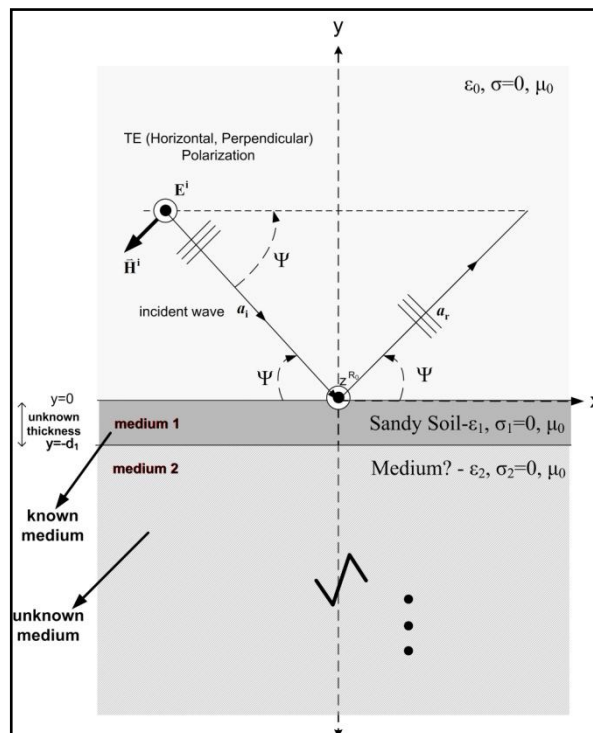
Figure 2.12. Schematic illustration of the problem for the unknown thickness d_1 and unknown dielectric constant of the medium$_2$-ε_{r_2}
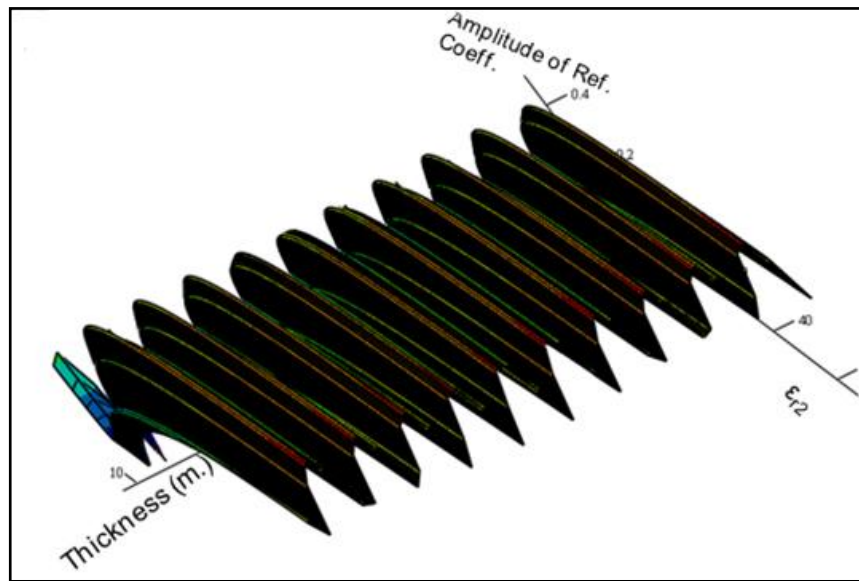
Figure 2.13. Surface plot of the amplitude of the calculated reflection coefficient (R_0) with respect to d_1 and ε_{r2}, for 100 MHz operation frequency and normal incidence case

The phase information is more convenient than the amplitude information for converging the unknown parameter quickly, as it's experienced in this study. Therefore, only phase information will be analyzed to investigate the unknown parameters in this section.

In this case, we'd like to investigate the thickness d_1 and ε_{r2} as unknown parameters (Figure 2.12). For $N=2$, if one sweeps phase of the calculated reflection coefficient (R_0) with respect to d_1 and ε_{r2} as a surface plot (Figure 2.13), one can obtain 41 different possible (d_1, ε_{r2}) pairs for the calculated reflection coefficient phase with (d_1=2.5 m, ε_{r2}=78.36 and ψ=90°), at 100 MHz. That calculated phase value is expected to be measured in the practical case. If more operation frequencies are applied such as 140, 180, 205 MHz, different possible common (d_1, ε_{r2}) pairs decrease down to 14. If one fixes the operation frequency at 205 MHz and then changes the incidence angles (ψ) as 60°, 30°, 20° and 75°, different possible common (d_1, ε_{r2}) pairs decrease down to nine (d_1=2.5 m, ε_{r2}=78.32-78.40). Therefore, the unknown (d_1, ε_{r2}) pair is approximately converged by changing both the operation frequency and incidence angle [87].

2.3. ANALYSIS OF THE ELECTROMAGNETIC FIELD SCATTERED BY A SPHERICAL TUMOR MODEL

In order to obtain the information about the existence and position of the malignant tumor, it is important to understand the electromagnetic scattering phenomenon of the tumor. Previously, cylindrically and spherically shaped tumor models have been presented to estimate the electromagnetic scattering features [88-93]. In one of the most recent analytical studies [92], the tumor was considered to have dimensions which were significantly smaller than the used wavelength assuming the case of an early stage cancer. In this sub-section, the previous methods of scattering analysis is extended to investigate the electromagnetic scattering from a lossy and dispersive dielectric spherical tumor with arbitrary diameter (in the 1-8 GHz frequency range) inside a lossy and dispersive dielectric breast fat tissue by using spherical vector wave functions. The dependence of the scattered field pattern on the tumor diameter and frequency, as well as polarization features of scattered fields are all presented. Comparable results of the scattered fields by the tumor inside breast fat and fibro-glandular tissues are also discussed.

2.3.1. Analytical Study for Perfectly Electric Conductor (PEC) Object

First of all, the scattering fields of a perfectly electric conductor (PEC) object (see Figure 2.14) is investigated as follows:
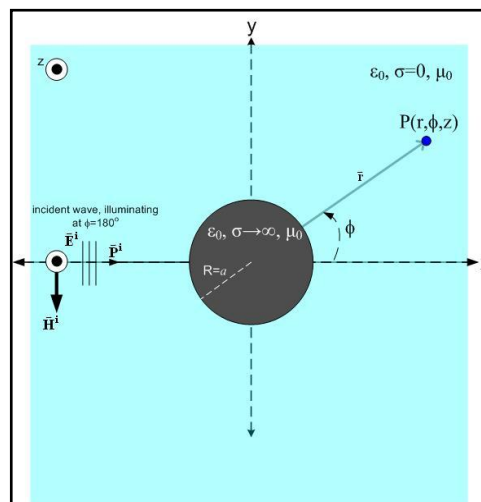
Figure 2.14. Illustration of an incident electromagnetic wave on a PEC object inside air

For a plane wave incident in positive *z*-axis direction, incident electric field can be expressed as:

$$\mathbf{E}^i = e^{-jk_0 z}\, \boldsymbol{a}_x = e^{-jk_0\left(r\cos(\theta)\right)}\, \boldsymbol{a}_x \tag{2.22}$$

The vector fields, **A** and **F** produce TM and TE (with respect to *r*) mode fields, respectively. The sum of the incident and scattered magnetic and electric vector potentials can be expanded as series [94]:

$$A_r = \frac{E_0}{\omega\mu}\cos(\phi)\sum_{n=1}^{\infty}\left[a_n\,\hat{J}_n\left(k_0 r\right)+b_n\,\hat{H}_n^{(2)}\left(k_0 r\right)\right]P_n^1\left(\cos(\theta)\right) \tag{2.23}$$

$$F_r = \frac{E_0}{k_0}\sin(\phi)\sum_{n=1}^{\infty}\left[a_n\,\hat{J}_n\left(k_0 r\right)+c_n\,\hat{H}_n^{(2)}\left(k_0 r\right)\right]P_n^1\left(\cos(\theta)\right) \tag{2.24}$$

where $\hat{J}_n(k_0 r) = k_0 r\, j_n(k_0 r)$, $\hat{H}_n^{(2)}(k_0 r) = k_0 r\, h_n^{(2)}(k_0 r)$, $k_0 = \sqrt{\omega^2\varepsilon_0\mu_0}$, $P_n^1(\cos(\theta)) = \partial P_n(\cos(\theta))/\partial\theta$, $a_n = j^{-n}(2n+1)/n(n+1)$.

Then, electric and magnetic fields can be obtained by;

$$
\begin{aligned}
E_r &= \frac{1}{\sigma+j\omega\varepsilon}\left(\frac{\partial^2}{\partial r^2}+k^2\right)A_r \\
E_\theta &= \frac{-1}{r\sin(\theta)}\frac{\partial F_r}{\partial\phi}+\frac{1}{r(\sigma+j\omega\varepsilon)}\left(\frac{\partial^2 A_r}{\partial r\,\partial\theta}\right) \\
E_\phi &= \frac{1}{r}\frac{\partial F_r}{\partial\theta}+\frac{1}{r\sin(\theta)(\sigma+j\omega\varepsilon)}\left(\frac{\partial^2 A_r}{\partial r\,\partial\phi}\right)
\end{aligned}
\tag{2.25}
$$

$$H_r = \frac{1}{j\omega\mu}\left(\frac{\partial^2}{\partial r^2}+k^2\right)F_r$$

$$H_\theta = \frac{1}{r\sin(\theta)}\frac{\partial A_r}{\partial\phi}+\frac{1}{r(j\omega\mu)}\left(\frac{\partial^2 F_r}{\partial r\,\partial\theta}\right)$$

$$H_\phi = -\frac{1}{r}\frac{\partial A_r}{\partial\theta}+\frac{1}{r\sin(\theta)(j\omega\mu)}\left(\frac{\partial^2 F_r}{\partial r\,\partial\phi}\right)$$

(2.26)

Since we have two unknowns b_n and c_n; then, only at least two boundary conditions are needed to be satisfied at $r=a$ on the sphere surface. Tangential components of electric field intensities, inside and outside the sphere are equal to each other. Then the unknown coefficients are found as:

$$b_n = -a_n\frac{\hat{J}'_n(ka)}{\hat{H}^{(2)\prime}_n(ka)}$$

$$c_n = -a_n\frac{\hat{J}_n(ka)}{\hat{H}^{(2)}_n(ka)}$$

(2.27)

Then, the scattering fields at far-fields can be obtained by using Equations (2.23), (2.24), (2.25), (2.26) and (2.27) as:

$$E_{\theta s} = -\frac{E_0}{kr}\cos(\phi)\frac{1}{\sin(\theta)}\left[\sum_{n=1}^{\infty}\left[c_n\,\hat{H}^{(2)}_n(kr)\right]P_n^1(\cos(\theta))\right]$$
$$+\frac{-E_0}{jkr}\cos(\phi)\sin(\theta)\left(\sum_{n=1}^{\infty}\left[b_n\,\hat{H}^{\prime(2)}_n(kr)\right]P'^1_n(\cos(\theta))\right)$$

(2.28)

$$E_{\phi s} = \frac{-E_0\sin(\theta)\sin(\phi)}{kr}\left[\sum_{n=1}^{\infty}\left[c_n\,\hat{H}^{(2)}_n(kr)\right]P'^1_n(\cos(\theta))\right]$$
$$+\frac{-E_0}{kr\sin(\theta)(j)}\sin(\phi)\left(\sum_{n=1}^{\infty}\left[b_n\,\hat{H}^{(2)\prime}_n(kr)\right]P_n^1(\cos(\theta))\right)$$

(2.29)

The comparisons of the total scattering field amplitudes with respect to ϕ in polar plot, for PEC objects with different radii (a) are successfully obtained by using both analytical and simulation results, as shown in Figure 2.15.
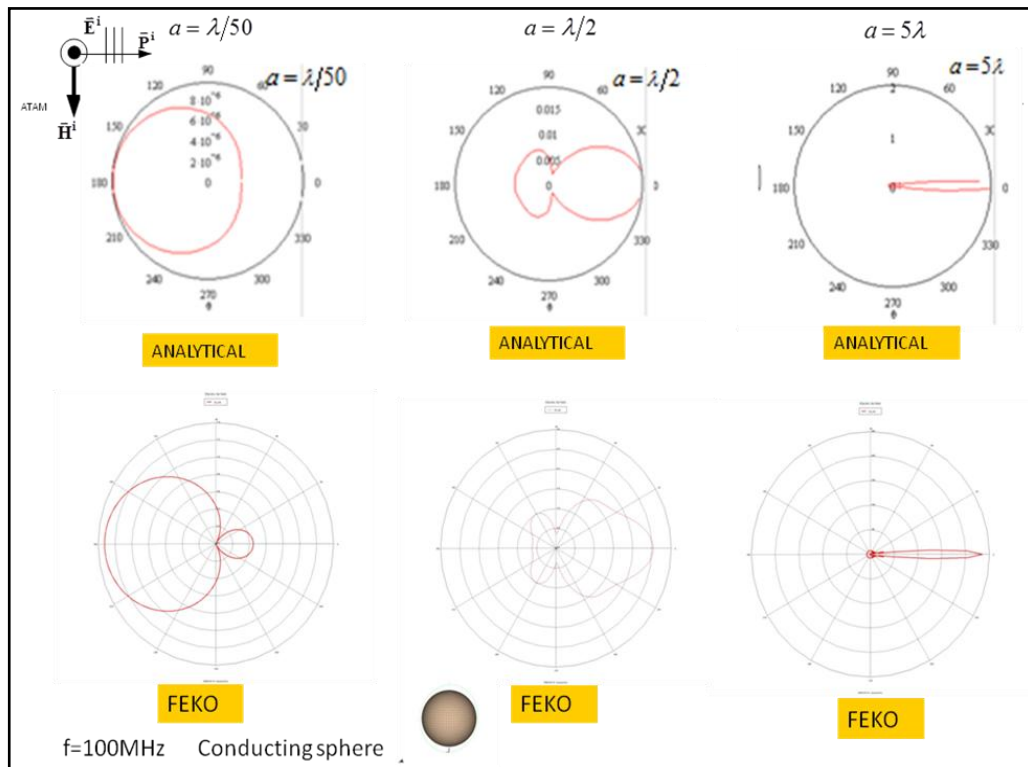
Figure 2.15. Comparisons of the total scattering field amplitudes with respect to ϕ in polar plot, for PEC objects with different radii a

2.3.2. Analytical Study for Spherical Tumor Model

For a plane wave incident in positive z-axis direction (see Figure 2.16), incident electric and magnetic fields can be expressed as:

$$\mathbf{E}^i = E_0\, e^{-jkz}\, \boldsymbol{a}_x$$
$$\mathbf{H}^i = H_0\, e^{-jkz}\, \boldsymbol{a}_y$$

(2.30)

The vector potentials can be written as,

$$\mathbf{A} = A_r\, \boldsymbol{a}_r$$
$$\mathbf{F} = F_r\, \boldsymbol{a}_r$$

(2.31)
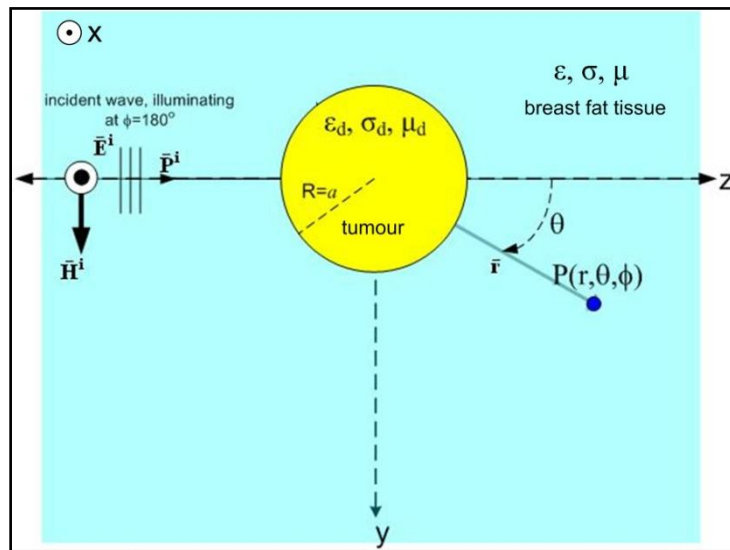
Figure 2.16. Illustration of an incident electromagnetic wave on a lossy and dispersive
dielectric tumor inside a lossy and dispersive breast fat tissue

A and **F** produce TM and TE (with respect to r) mode fields, respectively. The sum of the incident and scattered magnetic and electric vector potentials can be expanded as series [94]:

$$
\begin{aligned}
A_r^+ &= \frac{E_0}{\omega\mu}\cos(\phi)\sum_{n=1}^{\infty}\left[a_n\,\hat{J}_n(kr)+b_n\,\hat{H}_n^{(2)}(kr)\right]P_n^1\!\left(\cos(\theta)\right)\\
F_r^+ &= \frac{E_0}{k}\sin(\phi)\sum_{n=1}^{\infty}\left[a_n\,\hat{J}_n(kr)+c_n\,\hat{H}_n^{(2)}(kr)\right]P_n^1\!\left(\cos(\theta)\right)
\end{aligned}
\tag{2.32}
$$

for outside the spherical tumor ($r>a$), and

$$
\begin{aligned}
A_r^- &= \frac{E_0}{\omega\mu}\cos(\phi)\sum_{n=1}^{\infty}d_n\,\hat{J}_n(k_d r)P_n^1\!\left(\cos(\theta)\right)\\
F_r^- &= \frac{E_0}{k}\sin(\phi)\sum_{n=1}^{\infty}e_n\,\hat{J}_n(k_d r)P_n^1\!\left(\cos(\theta)\right)
\end{aligned}
\tag{2.33}
$$

for inside the spherical tumor ($r<a$), where $k = \sqrt{\omega^2\varepsilon\mu - j\sigma\omega\mu}$, and $k_d = \sqrt{\omega^2\varepsilon_d\mu_d - j\sigma_d\omega\mu_d}$.

Then, electric and magnetic fields can be obtained by using Equation (2.25) and (2.26). With the continuity of tangential components of electric and magnetic fields at $r=a$, one can obtain the closed form equations of the unknown constants; b_n, c_n, d_n and e_n.

$$b_n = a_n \frac{\xi \hat{J}_n'(ka)\hat{J}_n(k_d a) - \xi_d \hat{J}_n(ka)\hat{J}_n'(k_d a)}{\xi_d \hat{H}_n^{(2)}(ka)\hat{J}_n'(k_d a) - \xi \hat{H}_n^{(2)'}(ka)\hat{J}_n(k_d a)} \tag{2.34}$$

$$c_n = a_n \frac{k \mu_d \hat{J}_n(k_d a)\hat{J}_n'(ka) - k_d \mu \hat{J}_n'(k_d a)\hat{J}_n(ka)}{k_d \mu \hat{J}_n'(k_d a)\hat{H}_n^{(2)}(ka) - k \mu_d \hat{J}_n(k_d a)\hat{H}_n^{(2)'}(ka)} \tag{2.35}$$

$$d_n = a_n \frac{\xi \hat{H}_n^{(2)'}(ka)\hat{J}_n(ka) - \xi \hat{H}_n^{(2)}(ka)\hat{J}_n'(ka)}{\xi \hat{H}_n^{(2)'}(ka)\hat{J}_n(k_d a) - \xi_d \hat{H}_n^{(2)}(ka)\hat{J}_n'(k_d a)} \tag{2.36}$$

$$e_n = a_n \frac{k \mu_d \hat{H}_n^{(2)'}(ka)\hat{J}_n(ka) - k_d \mu \hat{H}_n^{(2)}(ka)\hat{J}_n'(ka)}{k \mu_d \hat{H}_n^{(2)'}(ka)\hat{J}_n(k_d a) - k_d \mu \hat{H}_n^{(2)}(ka)\hat{J}_n'(k_d a)} \tag{2.37}$$

Where $\xi = k / (\sigma + j\omega\varepsilon)$ and $\xi_d = k_d / (\sigma_d + j\omega\varepsilon_d)$. Detailed derivation of the coefficients are given in Appendix A.

The resulting scattering field components are as follows:

$$\begin{aligned} E_{rs} = {} & \frac{E_0 k \xi}{\omega\mu}\cos(\phi)\left[\sum_{n=1}^{\infty} b_n \hat{H}_n^{(2)}(kr) P_n^1(\cos(\theta)) \right] \\ & + \frac{E_0 k \xi}{\omega\mu}\cos(\phi)\left(\sum_{n=1}^{\infty} b_n \hat{H}_n^{(2)''}(kr) P_n^1(\cos(\theta)) \right) \end{aligned} \tag{2.38}$$

$$\begin{aligned} E_{\theta s} = {} & -\frac{E_0}{kr}\cos(\phi)\frac{1}{\sin(\theta)}\left[\sum_{n=1}^{\infty}\left[c_n \hat{H}_n^{(2)}(kr) \right] P_n^1(\cos(\theta)) \right] \\ & + \frac{-E_0 \xi}{r\omega\mu}\cos(\phi)\sin(\theta)\left(\sum_{n=1}^{\infty} b_n \hat{H}_n^{(2)'}(kr) P_n^{1'}(\cos(\theta)) \right) \end{aligned} \tag{2.39}$$

$$E_{\phi s} = \frac{-E_0 \sin(\theta)\sin(\phi)}{kr}\left[\sum_{n=1}^{\infty}\left[c_n\,\hat{H}_n^{(2)}(kr)\right]P_n^{1\prime}(\cos(\theta)) \right]$$
$$+ \frac{-E_0\,\xi}{r\,\omega\,\mu\sin(\theta)}\sin(\phi)\left(\sum_{n=1}^{\infty}b_n\,\hat{H}_n^{(2)\prime}(kr)\,P_n^1(\cos(\theta)) \right)$$

(2.40)

In order to validate the accuracy of the analytical derivations, a full-wave electromagnetic solver FEKO is used for simulations (Figure 2.17). To include the frequency dependence of dielectric properties of the breast fat, tumor and fibro-glandular tissues, the first Debye dispersion model has been applied assuming the values such as $\varepsilon_{r\infty}$, ε_{rs} and σ_s, as in [7, 14], as shown in Table 2.9 and Table 2.12.
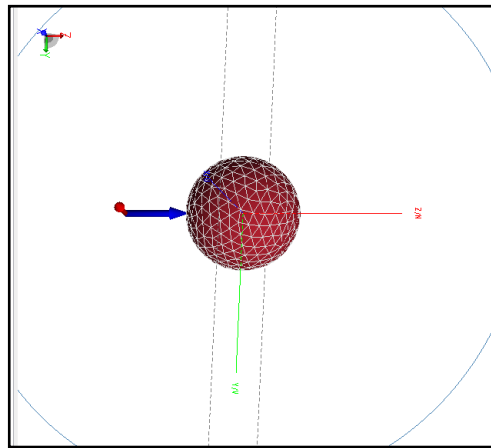
Figure 2.17. Simulation model of a lossy and dispersive dielectric tumor inside a lossy and dispersive breast fat tissue, on FEKO

The analytical and simulation (FEKO) results of amplitude and phase of the scattered field ($E_{\phi s}$) with respect to θ are successfully compared to each other, as shown Figure 2.18 and Figure 2.19, respectively. The magnetic permeability of both breast fat and tumor are taken as ($\mu_d = \mu = \mu_0 = 4\pi10^{-7}$ H/m), which is the common case. E_0 is taken as 1 V/m and radial measurement distance r is taken as 30 mm for all calculations and simulations, which are taken on y-z plane with $\phi=\pi/2$.
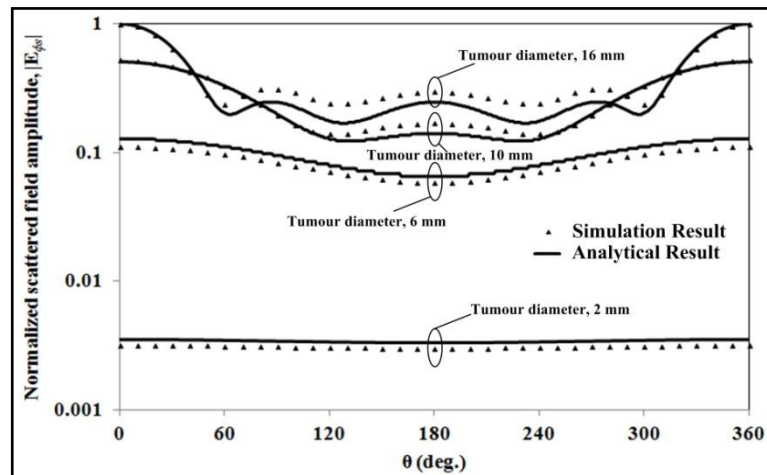
Figure 2.18. Normalized scattered field magnitude of $E_{\phi s}$ with respect to θ, for different diameters of spherical tumor models
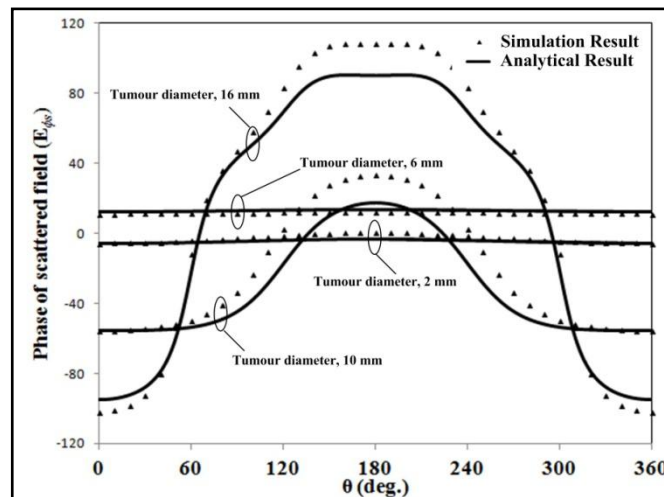
Figure 2.19. Phase of scattered field $E_{\phi s}$ (in degrees) with respect to θ, for different diameters of spherical tumor models

If one investigates the scattered field pattern with respect to θ for different operation frequencies, for tumor diameters of both 2 mm and 10 mm (see Figure 2.20 and Figure 2.21), it's observed that the scattered field pattern is almost uniformly distributed around the tumor for low frequencies. As the operation frequency increases, the back-scattered fields become highly dependent on θ. On the other hand, the scattered fields are generally greater for bigger tumors, especially at $\theta=0^o$.
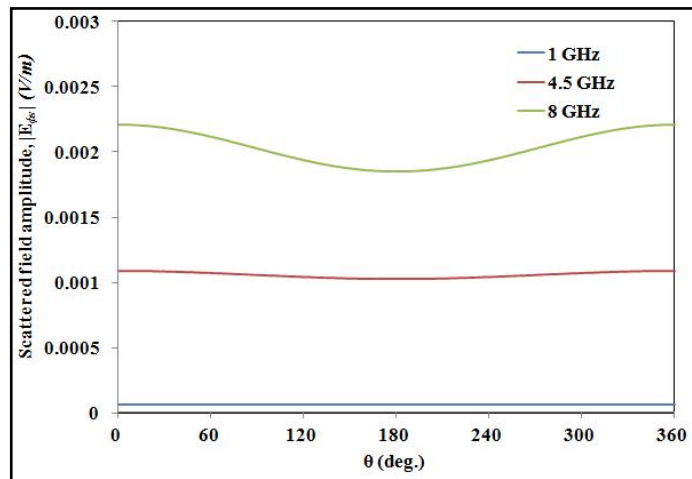
Figure 2.20. Scattered field magnitude of $E_{\phi s}$ with respect to θ, for different operation frequencies for tumor diameter of 2 mm
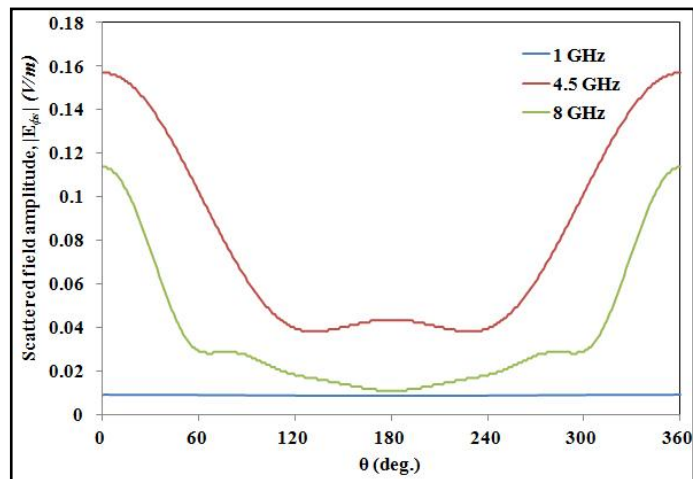
Figure 2.21. Scattered field magnitude of $E_{\phi s}$ with respect to θ, for different operation frequencies for tumor diameter of 10 mm

The back-scattered field amplitude with respect to different operation frequencies (1-8 GHz) has been also investigated for tumors with different diameters, as shown in Figure 2.22. As it's expected, the value of the back-scattered field for small tumors increases approximately with the square of the frequency, [91].
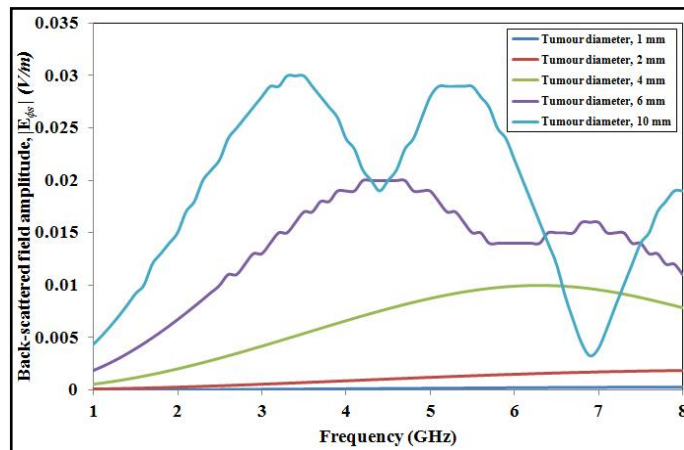
Figure 2.22. Back-scattered field magnitude of $E_{\phi s}$ with respect to frequency, for different diameters of spherical tumor models

For bigger tumors, oscillations in Figure 2.22 correspond to the resonance region between Rayleigh and optical approximations [94]. On the other hand, expected increment of the scattered fields by especially small tumors with frequency may have a positive impact on the dynamic range of an UWB microwave imaging system as the propagation loss of the incident and scattered field increases with the frequency [91].

If we compare the scattered field pattern results of tumor with 8 mm diameter inside breast fat and fibro-glandular tissues, the scattered field level is decreased for the tumor inside the fibro-glandular tissues; because of higher permittivity and conductivity values of the fibro-glandular tissue (Figure 2.23).

The scattered fields have all of the three r-, θ- and ϕ-components, as in Equations (2.38)-(2.40). However, in this sub-section only ϕ-component of the scattered field has been analysed because other cross-polarized θ- and r-components of the scattered field have negligible values compared to the co-polarized one, in y-z plane. Some of the researchers tried to use the co- and cross-polarized scattered fields to estimate the existence of the tumor [96]. However, the cross-polarized scattered field components seem to have a very low value. On the other hand, one should also investigate the scattering properties of the tumor inside a more realistic heterogeneous breast model from polarization point of view. It would be helpful to design perfectly polarized antennas to the tumor, for increasing dynamic range of a microwave imaging system [52].
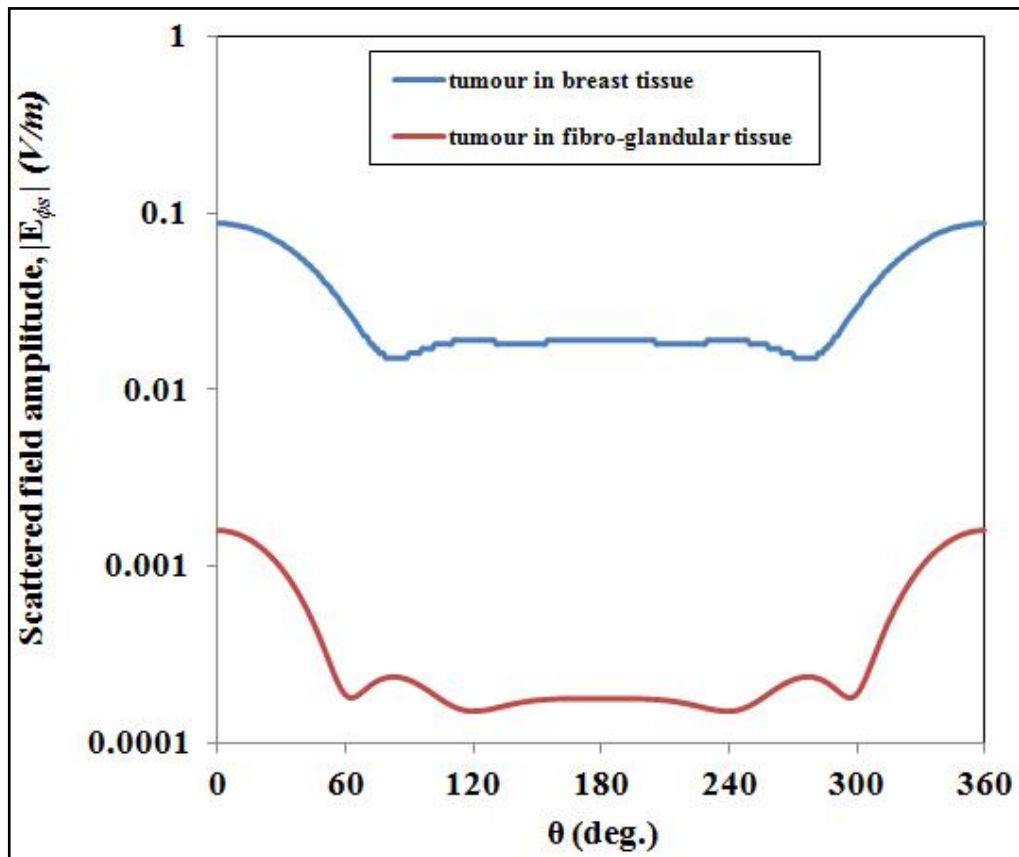
Figure 2.23. Comparison of scattered field by the tumor with 8 mm diameter inside breast fat and fibro-glandular tissues

2.4. MUTUAL COUPLING ANALYSIS BETWEEN ARBITRARILY ORIENTED THIN DIPOLE ANTENNAS OF UNEQUAL LENGTHS, LOCATED IN DISPERSIVE MEDIA

An analytical expression for the self and mutual impedance between arbitrarily oriented thin dipole antennas of unequal lengths, operating at any states of polarization located in a dispersive medium has been derived theoretically, by using classical induced EMF (Electromotive Force) method [77, 97-99]. Mutual impedance analyses of different kinds of array configurations of thin dipole antennas that are located and oriented arbitrarily in non-dispersive and dispersive media have been investigated, comparatively.

The general idea is to find the the mutual impedance between two antennas that are arbitrarily orientated outside the origin as shown in Figure 2.24.
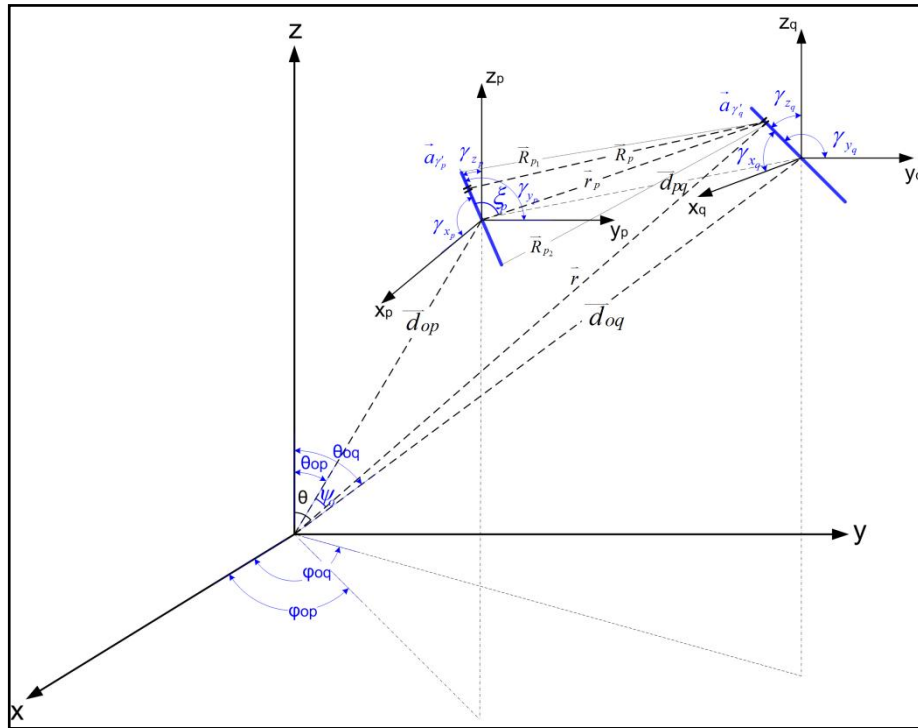
Figure 2.24. Arbitrarily oriented thin dipole antennas of unequal lengths, operating at any states of polarization located in a dispersive medium

The thin dipole antenna at the $(d_{op}, \theta_{op}, \phi_{op})$ point is directed at an angle γ_{x_p} with the x_p axis, angle γ_{y_p} with the y_p axis, angle γ_{z_p} with the z_p axis in the (x_p, y_p, z_p) coordinate system. The dipole source at the $(d_{oq}, \theta_{oq}, \phi_{oq})$ point, directed at an angle γ_{x_q} with the x_q axis, angle γ_{y_q} with the y_q axis, angle γ_{z_q} with the z_q axis in the (x_q, y_q, z_q) coordinate system. For a straight very thin dipole antenna oriented along the arbitrarily γ_p'-axis, the current distribution can be written as [77]:

$$I_p\left(\gamma_p'\right)=\begin{cases}I_{0p}\sin\left[k\left(\dfrac{L_p}{2}-\gamma_p'\right)\right], & 0<\gamma_p'<L_p/2\\[2mm] I_{0p}\sin\left[k\left(\dfrac{L_p}{2}+\gamma_p'\right)\right], & -L_p/2<\gamma_p'<0\end{cases} \tag{2.41}$$

In Equation (2.41), L_p corresponds to the p. antenna length and k corresponds to the propagation constant of the dispersive and lossy medium in which antennas are embedded [98]:

$$k = \sqrt{\omega^2 \left(\varepsilon' - j\,\varepsilon'' \right)\mu - j\sigma\omega\mu} \qquad (2.42)$$

The retarded vector potential (**A**) can be calculated as [98]:

$$\mathbf{A} = \boldsymbol{a}_{\gamma'_p}\left[\frac{\mu}{4\pi} \int_{0}^{L_p/2} \frac{I_0 \sin\left[k\left(\frac{L_p}{2} - \gamma'_p \right) \right]}{R_p} e^{-jkR_p} d\gamma'_p \right]$$
$$+ \boldsymbol{a}_{\gamma'_p}\left[\frac{\mu}{4\pi} \int_{-L_p/2}^{0} \frac{I_0 \sin\left[k\left(\frac{L_p}{2} + \gamma'_p \right) \right]}{R_p} e^{-jkR_p} d\gamma'_p \right] \qquad (2.43)$$

where R_p is the amplitude of the position vector from the origin of the (x_p, y_p, z_p) coordinate system to the infinite small $d\gamma'_p$ part, as shown in Figure 2.24.

The corresponding electric field intensity of the p. antenna effecting on the q. antenna $(E_{qp}(\gamma'_q))$ can be calculated by using Maxwell's equations [97, 98]. Once the electric field is known, taking the integral over the length of the q. antenna will give the mutual impedance regarding the use of the current distribution of the q. antenna, as in [77, 97]:

$$Z_{qp} = -\frac{1}{I_{0p} I_{0q}} \int_{-L_q/2}^{L_q/2} I_q(\gamma'_q) E_{qp}(\gamma'_q) d\gamma'_q \qquad (2.44)$$

Antenna lengths (L_p and L_q) can be selected arbitrarily, too. As the two antennas start to align in the same axis, the mutual coupling resistance and reactance values increases, as shown in Figure 2.25. On the other hand, those values decrease as the separation of the antennas increases, too. The mutual impedance is affected by the dispersive and lossy medium in which the antennas are embedded, like snow as in the case of Figure 2.26, as well as the operation frequency [77]. Those analyses would be helpful for investigations on the antenna array design for the microwave imaging system for breast cancer detection in

Section 4. The mutual coupling effects of an antenna array element can also be directly observed by measuring S_{21} scattering parameter, too.
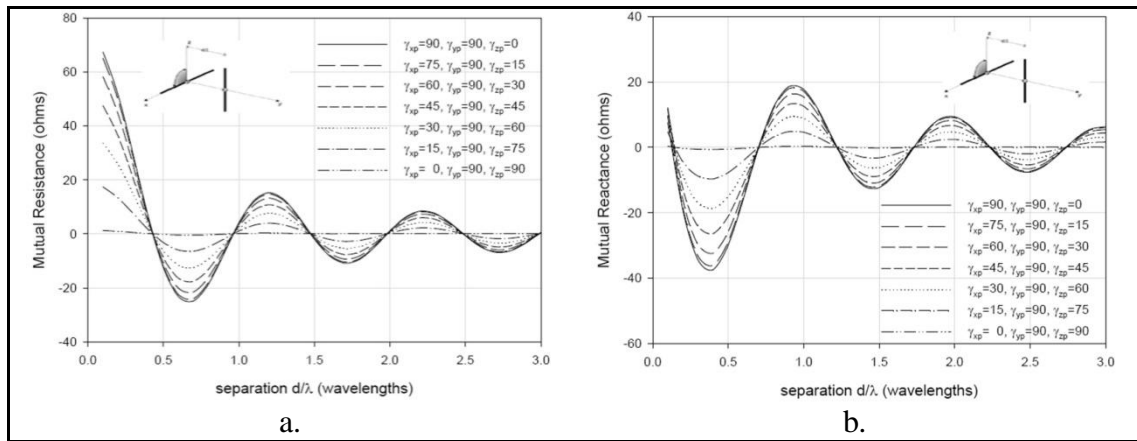
Figure 2.25. a. Mutual resistance (R_{21}) and b. mutual reactance (X_{21}) curves of two $\lambda/2$ thin dipole antennas operating in free space as a function of distance between them, while the first antenna orientated different angles above *x-z* plane
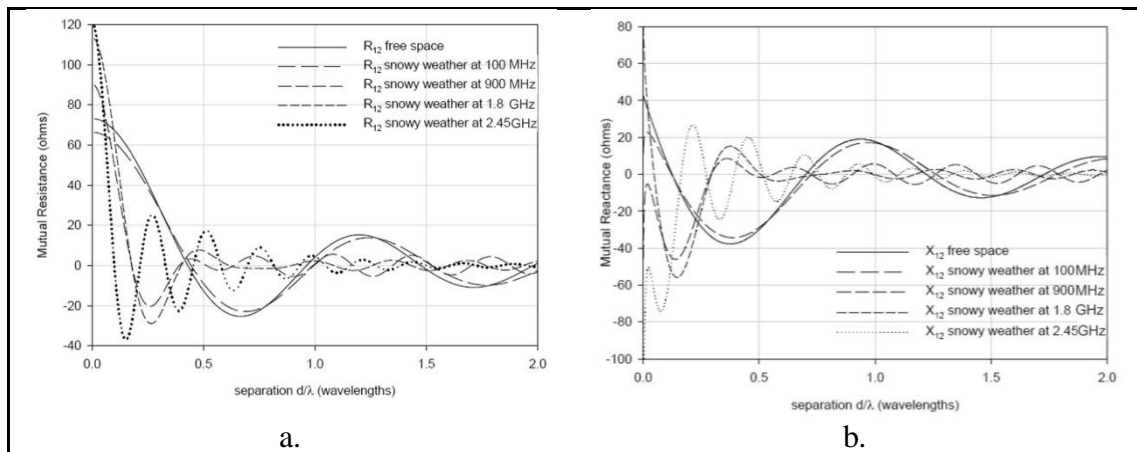
Figure 2.26. Comparison of a. mutual resistance (R_{21}) and b. mutual reactance (X_{21}) curves of two $\lambda/2$ thin dipole antennas operating in free space and in dispersive snow as a function of distance between them, for different operation frequencies

3. PRELIMINARY MICROWAVE IMAGING STUDIES

In this section, one of a microwave imaging system that has been tested and realized at the Scientific and Technological Research Council-BILGEM, is introduced [69]. A stacked patch antenna has been designed, fabricated and tested in operation in the experimental setup consisting of a spectrum analyzer (with vector network analysis option) and a planarly layered breast phantom model with tumor. Images are successfully obtained by using scattering electromagnetic waves from the tumor (S_{11}).

In the experimental measurement setup as shown in Figure 3.1, the stacked microstrip patch antenna is located 1 cm above the surface of a homogeneous planarly layered breast phantom model with tumor. The stacked patch antenna is connected to a handheld spectrum analyzer (R&S®FSH8, 100 kHz-8 GHz, with tracking generator and internal VSWR bridge) to transmit and receive microwave signals, and it is sequentially scanned in 1 cm increments to 361 different positions in a 19 cm × 19 cm array. The layered breast phantom model is illuminated by the patch antenna, and the backscattered signal (S_{11}) is recorded in the frequency range of 4.6-5.0 GHz. Electromagnetic absorbing materials within a box are located under the experimental setup to reduce ambient reflections (Figure 3.1).

Figure 3.1. Experimental setup of the microwave imaging system

3.1. STACKED MICROSTRIP PATCH ANTENNA

3.1.1. General Description and Characteristics of Microstrip Antennas

The idea of the microstrip antenna dates back to the 1950's, but it was not until the 1970's that serious attention was given to this antenna. The basic configuration of a microstrip antenna is a metallic patch printed on a thin, grounded dielectric substrate. Originally, the element was fed with either a coaxial line through the bottom of the substrate, or by a coplanar microstrip line. This latter type of excitation allows feed networks and other circuitry to be fabricated on the same substrate as the antenna element [100].

There are many advantages of the microstrip antennas. The microstrip antenna radiates a relatively broad beam, broadside to the plane of the substrate. Thus the microstrip antenna has a very low profile, and can be fabricated using printed circuit techniques. This implies that the antenna can be made conformable, and potentially at low cost. Other advantages include easy fabrication into linear or planar arrays, and easy integration with microwave integrated circuits [100].

Since the original configuration was proposed, literally dozens of variations in patch shape, feeding techniques, substrate configurations, and array geometries have been developed by researchers throughout the world. The variety in design that is possible with microstrip antennas probably exceeds that of any other type of antenna element. Another interesting feature is that microstrip antennas can be fabricated rather easily in universities or other research laboratories, which have been a source of novel designs [100]. Also they have weight and size benefit. They can be used in space applications for their aerodynamic profiles with aircrafts, rockets or spacecrafts. Composite systems can be developed by adding some semiconductor components such as oscillator, amplifier, attenuator, switches, modulator, mixers, phase shifter, etc. onto the ground plane appropriately. In practical applications, they are developed to operate between 400 MHz - 38 GHz, and it's hoped to increase this frequency limit up to 60 GHz. They are also conformable to planar and nonplanar surfaces.

However, disadvantages of the original microstrip antenna configurations include narrow

bandwidth, spurious feed radiation, poor polarization purity, limited power capacity, and tolerance problems. Much of the development work in microstrip antennas has gone into trying to overcome these problems, in order to satisfy increasingly stringent systems requirements. This effort has involved the development of novel microstrip antenna configurations, and the development of accurate and versatile analytical models for the understanding of the inherent limitations of microstrip antenna, as well as for their design and optimization [100]. Other disadvantages are low gain (low efficiency), radiation only in one half plane, excitation of surface waves, poor end-fire radiator and complex feed structures required for high-performance arrays.

The most common application areas are as follows [100, 101]:

- Radar, communications, navigation, altimeter, landing systems on aircrafts
- Radar, telemetry on missiles
- Communications, direct broadcast TV, remote sensing radars and radiometers on satellites
- Radar, communications, navigation on ships
- Mobile satellite telephone, mobile radio on land vehicles
- Biomedical systems, intruder alarms
- GPS

The most common substrates used for the microstrip antennas are as follows:

- Polytetrafluoroethylene(PTFE) with glass net
- Polytetrafluoroethylene(PTFE) with fiber net
- Glass Bounded Mica
- Semiconductors
- Ceramic substrates, etc.

Microstrip antennas, as shown in Figure 3.2, consist of a very thin metallic strip (patch) placed a small fraction of a wavelength, within the substrate ($h << \lambda$, usually $0.003\lambda \leq h \leq 0.05\lambda$), above a ground plane. The microstrip antenna is designed so its pattern maximum

is normal to the patch (broadside radiator). This is accomplished by properly choosing the mode (field configuration) of excitation beneath the patch. End-fire radiation can also be accomplished by judicious mode selection. For a rectangular patch, the length L of the element is usually $\lambda/3 < L < \lambda/2$. The patch and the ground plane are separated by a dielectric sheet (substrate) [97].
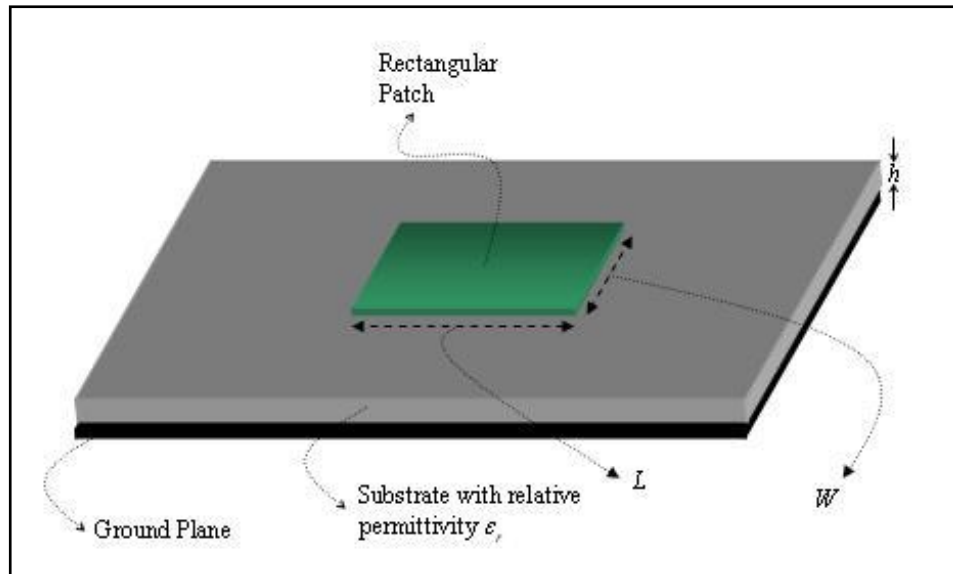
Figure 3.2. Microstrip antenna with rectangular patch

Consider a basic rectangular microstrip antenna with a probe feed. When operating in the transmitting mode, the antenna is driven with a voltage source between the feed probe and the ground plane. This excites current on the patch and the ground plane. The dielectric substrate is usually electrically thin ($h < 0.05\lambda$), so electric field components parallel to the ground plane must be very small throughout the substrate. The patch element resonates when its length is near $\lambda/2$, leading to relatively large current and field amplitudes.

The antenna can be viewed as a cavity with slot-type radiators with equivalent magnetic currents, radiating in the presence of the grounded dielectric substrate. Alternatively, radiation can be considered as being generated by the induced surface current density on the patch element in the presence of the grounded dielectric substrate. In either case, the equivalent sources produce a broadside radiation pattern.

The radiating patch may be square, rectangular, circular, elliptical, triangular, or any other arbitrary shaped structure. Square, rectangular, dipole (strip), and circular are the most common because of ease of analysis and fabrication, and their attractive radiation characteristics, especially low cross-polarization radiation. Microstrip dipoles are attractive because they inherently possess a large bandwidth and occupy less space, which makes them attractive for arrays.

3.1.2. Bandwidth Enhancement Techniques

Microstrip antennas have been studied for many years because of their low cost, thin profile, light weight, ease of fabrication, their capability of being mounted on curved surfaces and being integrated in active devices. The most important drawback of microstrip antennas is narrow bandwidth (2 per cent-5 per cent). Various methods have been studied to overcome this drawback. The most direct method of increasing the bandwidth of the microstrip element is to use a thick, low dielectric constant substrate. But this leads to unacceptable spurious feed radiation, surface wave generation, or feed inductance. Since the bandwidth of the element is usually dominated by the impedance variation (the pattern bandwidth is generally much better than the impedance bandwidth), it is often possible to design a planar impedance matching network to increase bandwidth. Bandwidths of 9 per cent-12 per cent have been obtained in this manner of probe-fed and microstrip line-fed elements. If the matching network is coplanar with the antenna element, spurious radiation from the matching network may be a concern [100].

Increased bandwidth can be obtained in a variety of ways by using parasitically coupled elements. Bandwidths of 10 per cent-20 per cent have been obtained with probe-fed stacked patches, and 18 per cent-23 per cent bandwidths have been achieved for aperture coupled stacked patches [100]. Stacked patch antenna concept is one of the methods to increase the bandwidth of the antenna. Stacked patch antenna generally consists of a parasitic patch on another layer so that bandwidths of about 25 per cent can be achieved. In this study, a stacked microstrip patch antenna has been chosen as a good candidate for UWB microwave imaging of breast tumor detection. The measurement result of the antenna is shown in Figure 3.3.b [69].
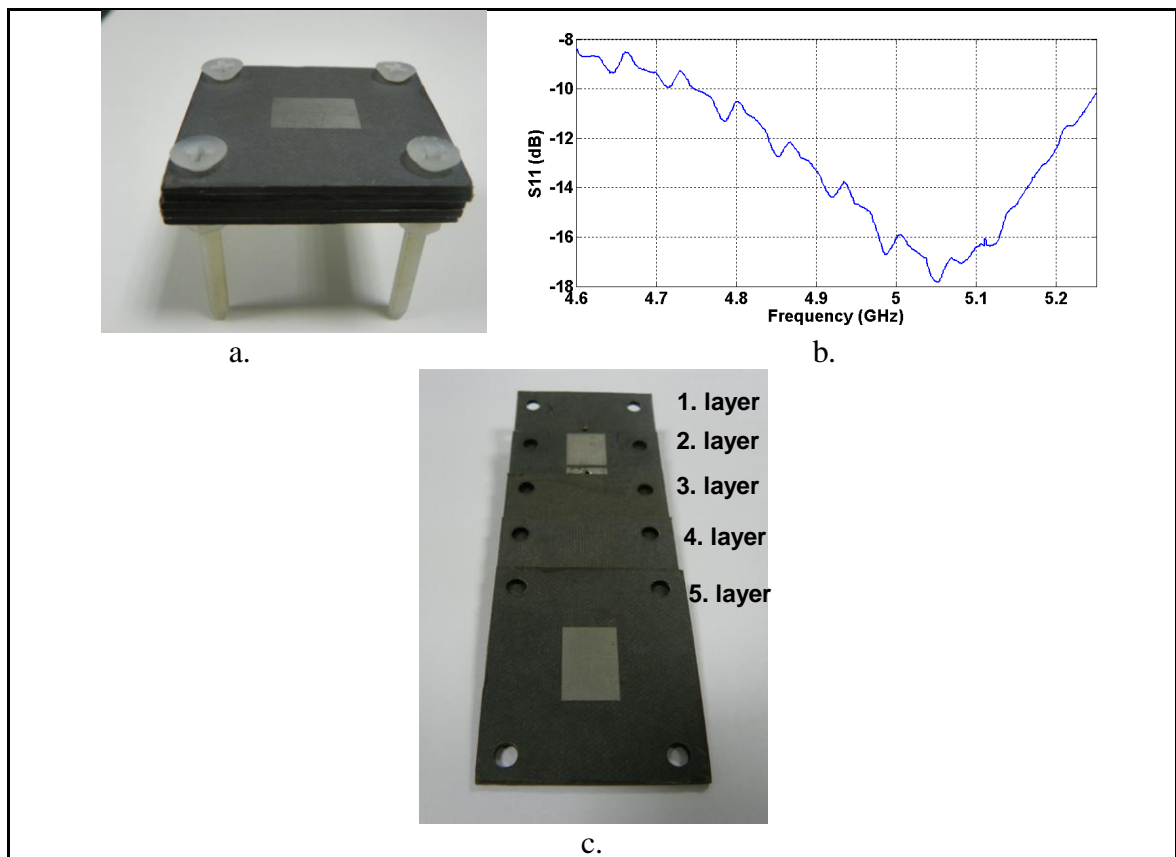
Figure 3.3. a. Stacked patch antenna, b. measurement of return loss of the stacked patch antenna, c. views of each layer of the stacked patch antenna

3.2. LAYERED PLANAR BREAST PHANTOM MODEL

The layered breast phantom consists of a container (plexiglass) filled with planar layers of breast fat tissue simultant, skin tissue simultant, and also spherical objects embedded at the bottom of the breast fat tissue simultant (Figure 3.4). For the experimental tests, appropriate materials for the layered breast phantom model with tumor have been determined based on the proposed phantom model studies in [24, 102, 103]. Soybean oil is used as the breast fat tissue simultant [24]. The soybean oil is contained in the 30 cm × 30 cm × 5 cm tank. The skin layer in the phantom is created using a simple moisturizing lotion [102]. These breast fat and skin simultants are inexpensive and nontoxic with dielectric properties that mimic roughly those of actual tissues [24, 102]. Two spherical objects both with 2 cm diameters are used, such that one of them is simulating tumor, and the other is chosen as PEC object for distinguishing them in the imaging results. The tumor

simulating one is elastic and it's constructed based on the procedure suggested for preparing tumor tissue-mimicking materials in [103].
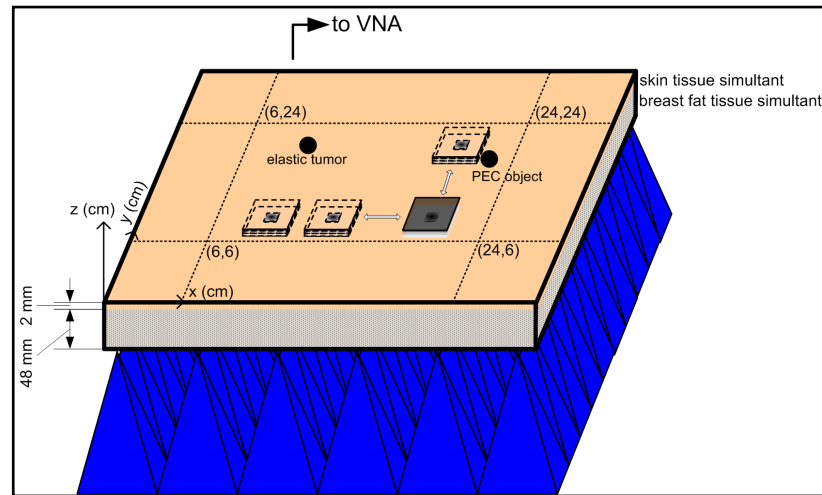
Figure 3.4. Schematic representation of layered breast phantom model

3.3. CONSTRUCTION OF ELASTIC TUMOR SIMULTANT

The elastic tumor is constructed based on the procedure suggested for preparing tumor tissue-mimicking materials in [103], at the laboratories of the Genetics and Bioengineering Department of Yeditepe University. The materials and quantities for tumor phantom are as follows (See Figure 3.5):

- 100 ml desionised tridistilled water
- 60 ml ethanol
- 1 g NaCl
- 1.5 g agarose

The construction procedures for tumor phantom are as follows:

- Measure the quantity of the materials required for the phantom (See Figure 3.6)
- Mix desionised tridistilled water with NaCl (See Figure 3.6)
- Add ethanol to the mixture (See Figure 3.6)

- Heat the compound and add, at 80°, agarose. (See Figure 3.7)

Figure 3.5. The materials and quantities for tumor phantom construction

a. b.
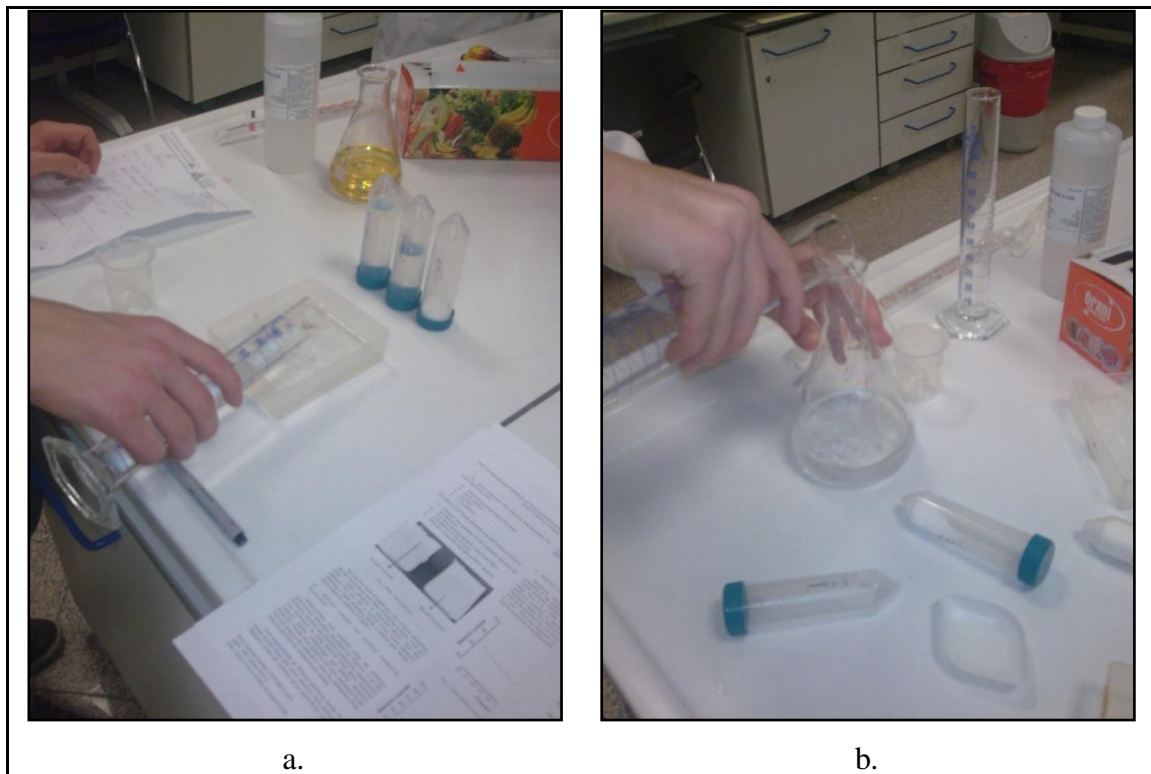
Figure 3.6. Preparation of the materials and the compound before the heating process
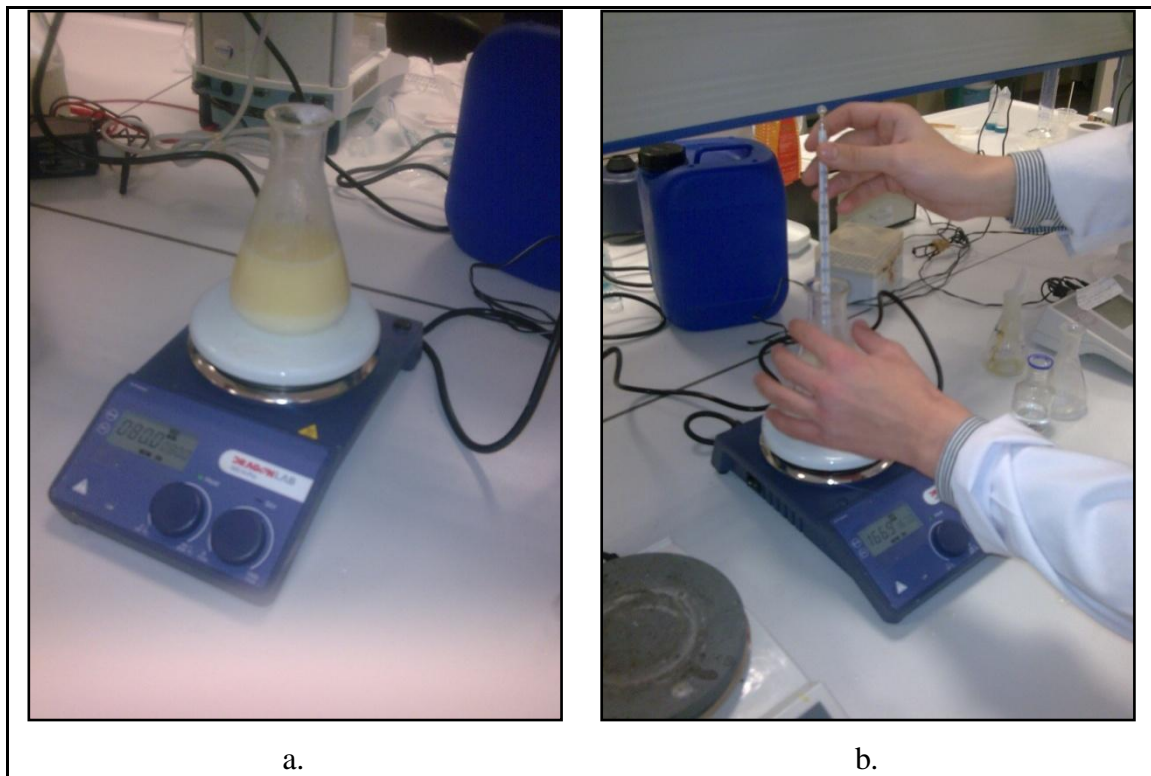
Figure 3.7. a. The heating process, b. checking the temperature before adding agarose

After the construction procedures are finished, the final mixture is waited for being cooled and becoming jelly, for one day.

3.4. EXPERIMENTAL STUDY AND SIMULATION RESULTS

In UWB microwave radar system, signal processing algorithms such as delay-and-sum (DAS) beamforming, penalized least-squares optimal beamforming, a generalized likelihood ratio test, time-reversal techniques, MIST and MAMI algorithms are generally applied to the recorded backscattered microwave signals to localize and characterize malignant breast tumors [28, 105]. In this study, a simpler microwave imaging method is used. The designed stacked microstrip patch antenna is sequentially scanned in 1 cm increments and the backscattered signal (S_{11}) is recorded in the frequency range of 4.6–5.0 GHz. Measured frequency-domain data is recorded at 631 frequency points, and its time/space domain equivalent is obtained by using inverse FFT. Then, images of the computed signal energies are created as a function of position, which is a similar procedure

like Inverse Synthetic Aperture Radar (ISAR) [104]. The tumor is successfully detected as shown in Figure 3.8.
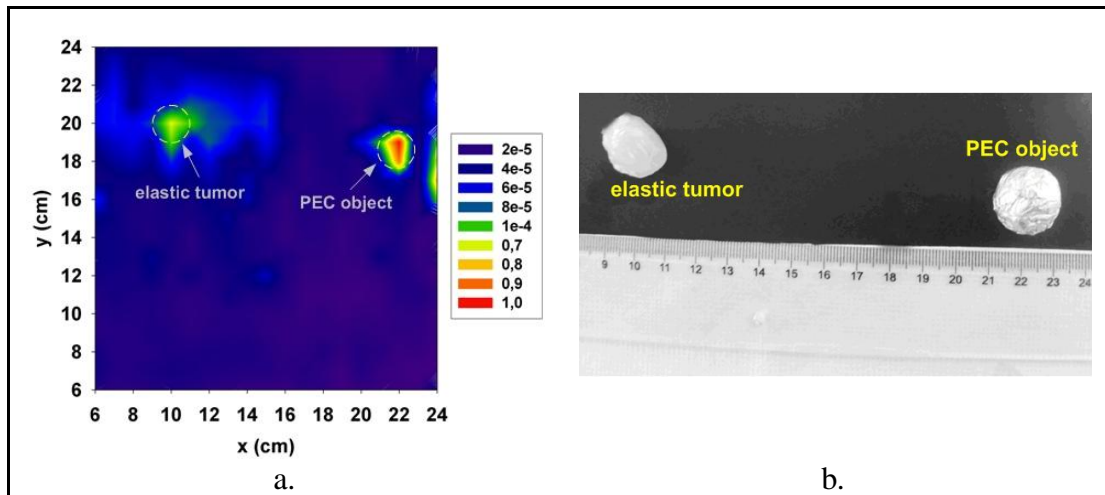
Figure 3.8. a. Color image of the backscattered energies with actual locations of tumor and PEC object drawn by yellow circles, b. real dimensions of constructed elastic tumor and PEC object

CST Microwave Studio® software has been used for the simulation study to compare and verify the experimental results (Figure 3.9). The backscattered frequency-domain signals (S_{11}) are recorded in the frequency range of 4.6–5.0 GHz, at 1001 discrete frequency points. The stacked patch antenna is automatically scanned in 1 cm increments for 361 different location points in the 19 cm × 19 cm area (Figure 3.9). The computation time is 20 min. for each location point and totally, around five days to complete the simulation.
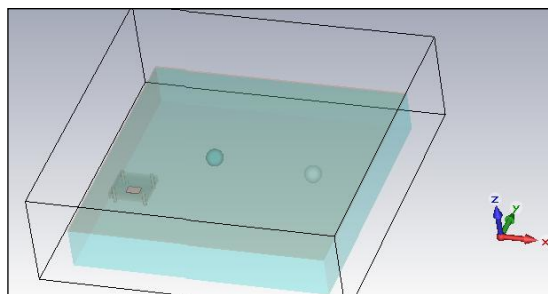
Figure 3.9. Simulation model of the layered planar breast phantom model and the stacked patch antenna in CST Microwave Studio®

If one compares the imaging result obtained with the simulation study, it's very close to the obtained one with the experimental result (Figure 3.10). Since the dielectric properties of the phantoms used in the experiments are not completely equal to those of the phantom models in the simulation study, there exist some little differences in the results, too.
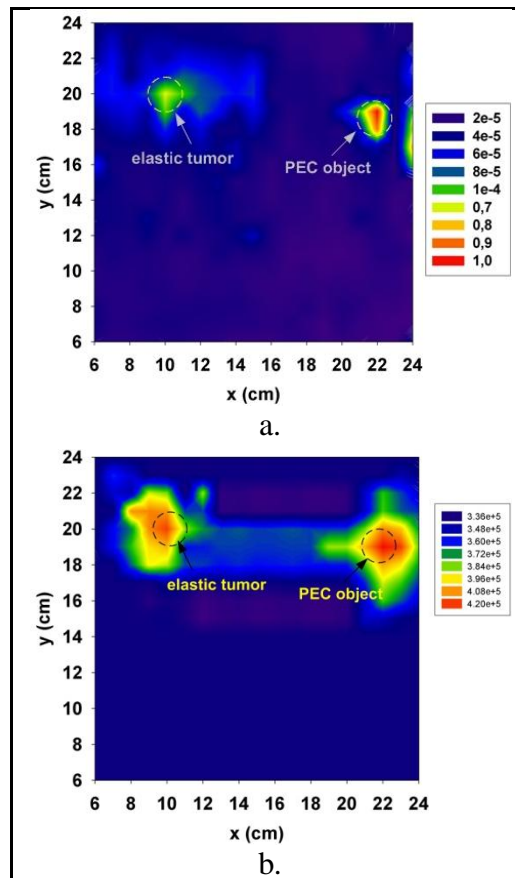
Figure 3.10. a. Experimental imaging result with actual locations of tumor and PEC object drawn by yellow circles, b. imaging result obtained by simulation with actual locations of tumor and PEC object drawn by black circles

Experimental feasibility of the UWB microwave imaging system is demonstrated using an initial imaging setup and a layered breast phantom. The antenna designed for the microwave imaging system is measured. We were able to detect the elastic tumor model with 2 cm diameter by using so many frequency and position dependent raw data, although dielectric properties of tumor and breast are close to each other compared to the PEC object. The imaging results obtained by the simulation study are approximately equal to the one obtained by the experimental study. Initial imaging results are promising; however

more extensive work is required with more realistic phantom models, improved and fast imaging algorithms.

3.5. INVESTIGATIONS ON ELECTROMAGNETIC IMMUNITY OF A MICROWAVE IMAGING SYSTEM WITH CIRCULAR CONFORMAL MICROSTRIP PATCH ANTENNAS FOR PEOPLE WHO USE PACEMAKERS

In this study, electromagnetic immunity analysis of a microwave imaging system designed with circular conformal patch antennas for people who use pacemakers [106]. The full-wave electromagnetic simulator (CST Microwave Studio®), which is based on the finite integration technique (FIT), is used to calculate the near fields around the modeled pacemaker of the conformal antennas located encircling the realistic dispersive human breast model. The computed near field results are successfully compared to threshold levels of the power density noted in the standards.

Electromagnetic fields are one of the most important factors that can affect the operation of pacemakers. They can induce currents along the electrode of pacemaker that can affect the heart beat rate of the pacemaker directly [107]. Moreover, there are other potential hazardous effects, too. The pacemaker can move under high static fields. As the power density of the applied electromagnetic fields increases over the pacemaker, the pacemaker itself can be heated, as well as the nearby tissues around the pacemaker that may cause the probability of burning of the tissues nearby the pacemaker [108]. If the electronic circuit of the pacemaker is affected by the electromagnetic fields, it can arbitrarily reprogram itself [109]. On the other hand, every pacemaker can be affected by the electromagnetic fields, differently [109].

People who use pacemakers should denote that they use pacemakers before they're applied the MRI. But, it's difficult to apply MRI for the people who use pacemakers, because of possible hazardous effects mentioned above. The pacemaker production firms cover them with titanium material or use electromagnetic filtering. There are some new generation pacemakers produced that are compatible to MR equipments. However, MR equipments continue to be a risk factor for pacemakers.

Breast cancer is the most frequent cause of cancer related to death for women in both developed and developing countries. Early diagnosis and treatment are the hot keys to survive from breast cancer. MRI is either less effective or is too costly for this purpose, beside its high risk factor for people who use pacemakers. Other available screening techniques such as X-ray mammography and ultrasound technique are more confidential for people who use pacemakers. Since they have a lot of disadvantages as mentioned in Section 1, microwave imaging techniques are developing for breast cancer detection, alternatively. In this study, it's intended to investigate the electromagnetic immunity characteristics of the microwave imaging system designed with circular conformal patch antennas for people who use pacemakers [106].

If an incoming electromagnetic field is induced currents along the electrode of a pacemaker, a voltage is induced at the input port of the pacemaker which can affect the operation of the pacemaker. The effects of electromagnetic interference on pacemakers as well as the procedures for electromagnetic immunity tests are given in the ANSI/AAMI PC69:2007 (US) test standard [110]. The effect level of pacemakers depends on the applied frequency of the electromagnetic field, application time, power level, modulation type and the patient himself.

First of all, a half-spherical conformal antenna array encircling the breast as part of a microwave imaging system operating between 2.4 and 2.5 GHz has been design with 17 spherical conformal microstrip patch antennas, as shown in Figure 3.11.
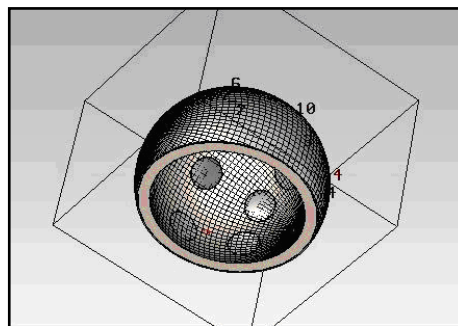
Figure 3.11. Simulation model of the spherical conformal microstip patch antenna array in CST Microwave Studio®

In CST Microwave Studio® (full electromagnetic simulator), the antennas are located as encircling the realistic dispersive female body (voxel) model, which is also already loaded in the CST (Figure 3.12). The dielectric properties of the female voxel model are also defined for the operation frequency of 2.4 GHz in the CST.
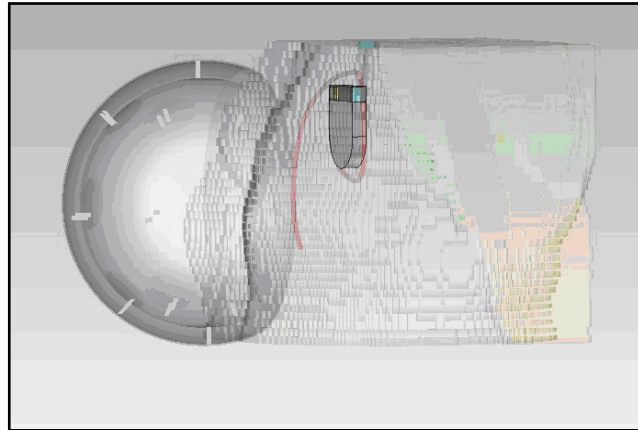
Figure 3.12. Simulation model of the realistic dispersive female body (voxel) model, pacemaker model and the antenna array in CST Microwave Studio®

A pacemaker is modeled in CST Microwave Studio® with the approximate dimensions of 40 mm × 30 mm × 7.5 mm [111]. The length of the electrode is 37.35 cm. The covering of the battery and the electronic circuitry of the pacemaker is selected as PEC (Figure 3.13).
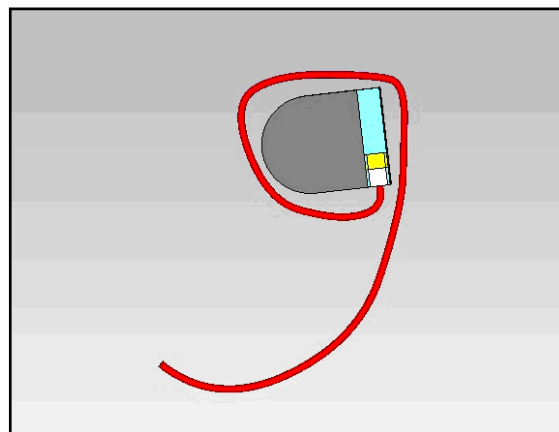
Figure 3.13. Simulation model of the pacemaker in CST Microwave Studio®

The output power of each antenna is selected as 1 mW. As a worst case, all of the antennas

are operated at the same time. The simulation results of near field power density distribution over the antenna array and the pacemaker is given in Figure 3.14. The simulation result of induced current distribution along the pacemaker electrode is also given in Figure 3.15.
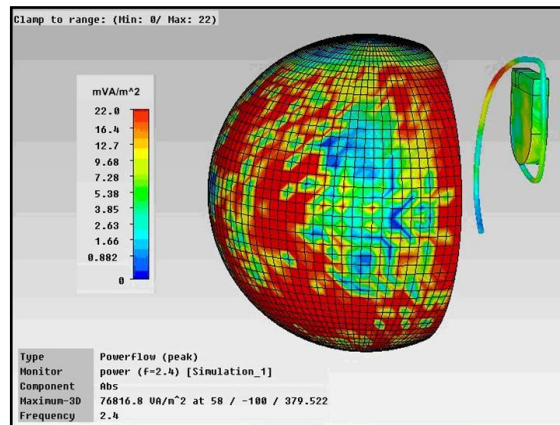
Figure 3.14. Simulation result of electromagnetic power density distribution over the antenna array and the pacemaker
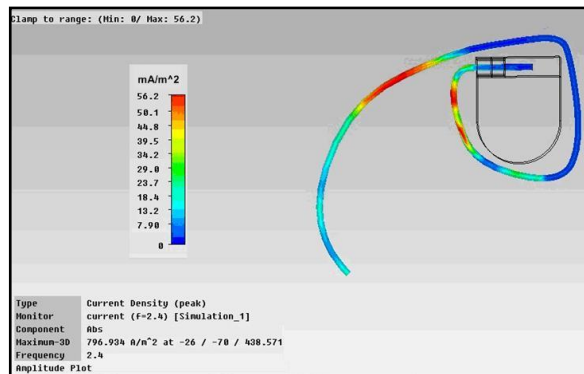
Figure 3.15. Simulation result of induced current distribution along the pacemaker electrode

The induced current levels are more in some regions along the electrode. Maximum power density level is obtained 2.2 μW/cm^2, near around the pacemaker electrode. This level is below the threshold level (1 mW/cm^2) [112]. However, the standard threshold levels change with respect to years and new researches, too. It's obviously seen that the effect of the microwave imaging system is expected to be negligible for the pacemakers.

4. DESCRIPTION OF THE UWB MICROWAVE IMAGING SYSTEM

4.1. LAYERED HALF-SPHERICAL BREAST PHANTOM MODELS

Layered breast phantom model consists of a skin tissue layer with thickness of 2 mm and three different half-spherical tissues with radius of 58 mm under the skin, such as homogeneous fatty breast, quasi-heterogeneous mix of fibro-glandular and fatty breast, and homogeneous fibro-glandular tissues (Figure 4.1). The homogeneous fatty breast, quasi-heterogeneous and homogeneous fibro-glandular phantom models represent "mostly fatty", "heterogeneously dense" and "very dense" phantom models, respectively.

The breast phantom is surrounded by a coupling medium in which antennas are placed. Antennas are immersed in the coupling medium in order to get a good impedance matching with the breast. Non-dispersive relative permittivity ε_r and complex conductivity σ^* values of skin, ducts, fatty breast, fibro-glandular and tumor tissues are selected from Tables 2.1, 2.2, 2.3, 2.4, and 2.7; as summarized in Table 4.1. Moreover, dielectric constant of the lossless coupling medium is selected as $\varepsilon_r=9$ [60] (Table 2.8).
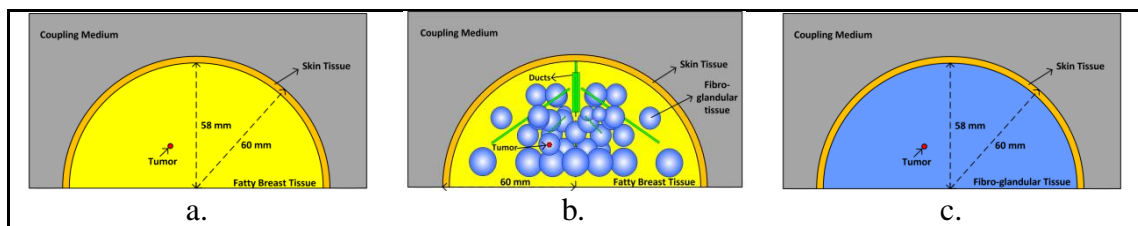
Figure 4.1. Schematic illustration of layered half-spherical breast phantom models with a. homogeneous fatty breast tissue, b. quasi-heterogeneous mix of fibro-glandular and fatty breast tissues, and c. homogeneous fibro-glandular tissue

Differently sized glands of spherical (radius, 8.5 mm $< r_g <$ 12.5 mm) shape [113] are embedded in the fatty breast tissue for the quasi-heterogeneous phantom model, as shown in Figure 4.1(b). As the DAS algorithm is not found to be suitable for the frequency dispersive tissues [20], only non-dispersive properties are used in the simulations. The dispersive effects of of breast phantom model on UWB microwave imaging are also discussed in Section 4.4.2.

Table 4.1. Non-dispersive dielectric properties of the tissues

Tissue	ε_r	σ^* (S/m)
Skin [15, 22, 25]	36	4
Ducts [73]	37.96	4.5
Fatty Breast Tissue [22, 60, 70, 80, 81]	9	0.4
Glandular Tissue [73]	21.5	1.7
Tumor [16, 71, 80]	50	7

4.2. DELAY-AND-SUM (DAS) ALGORITHM

When one of the seven antennas in the array is excited by sine-modulated Gaussian pulse, back-scattered time-domain signals (S_{ii} and S_{ij}, i≠j) are recorded (Figure 4.2). This procedure is repeated by feeding each antenna sequentially, for cases with and without 2 mm diameter tumor. Therefore, 49 time-domain signals coming from different antennas are recorded for each case. Tumor response signals S_{ij}^T are obtained by calibrating the recorded signals as in Equation (4.1):

$$S_{ij}^T = S_{ij}\big|_{with\,tumor} - S_{ij}\big|_{without\,tumor} \qquad (4.1)$$

The tumor response signals are additionally compensated for $1/r$ attenuation of electric fields inside the breast and electromagnetic scattering from spherical tumor with different signal levels at different angles [52].

When 1. antenna is fed and signal is received from 3. antenna, one can easily compute time delay for the possible tumor location depicted in Figure 4.2. Accordingly, time delay between the transmitted signals from 1. antenna and the received signal by 3. antenna can be computed as in Equation (4.2), regarding phase velocities of electromagnetic fields in different media, individually.
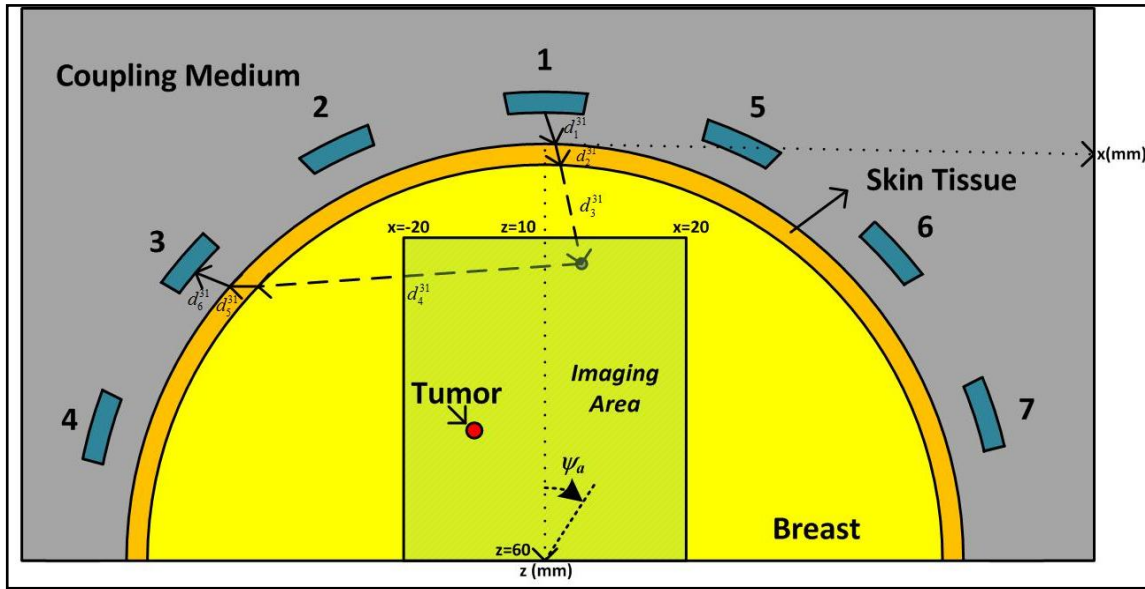
Figure 4.2. Schematic illustration of breast phantom model and antenna placements for computing time delays

$$\tau_{31}^{d}(\vec{r}) = \frac{d_1^{31}(\vec{r})}{v_{coupling}} + \frac{d_2^{31}(\vec{r})}{v_{skin}} + \frac{d_3^{31}(\vec{r})}{v_{breast}} + \frac{d_4^{31}(\vec{r})}{v_{breast}} + \frac{d_5^{31}(\vec{r})}{v_{skin}} + \frac{d_6^{31}(\vec{r})}{v_{coupling}} \qquad (4.2)$$

Total tumor response for each pixel is obtained, as in Equation (4.3), regarding computed time delays between each antenna and pixel points, one by one [8]. Then, images of the computed scattered signal energies for each pixel are created as a function of position.

$$T(\vec{r}) = \left[\sum_{i=1}^{7} \sum_{j=1}^{7} S_{ij}^{T}\left(\tau_{ij}^{d}(\vec{r})\right) \right]^2 \qquad (4.3)$$

In a typical confocal breast imaging system using DAS algorithm, the set back-scattered signals are time-shifted to achieve coherent addition for a specific focal point within the breast, as shown in Figure 4.3. The focal point is then scanned throughout the breast by adjusting the relative amount of time-shift applied to each backscattered signal. It only seeks to identify and locate the presence of strong scatterers within the breast. If one scans a point on which the tumor does not exist ($r \neq r_0$) would lead incoherent sum of the time-shifted signals.
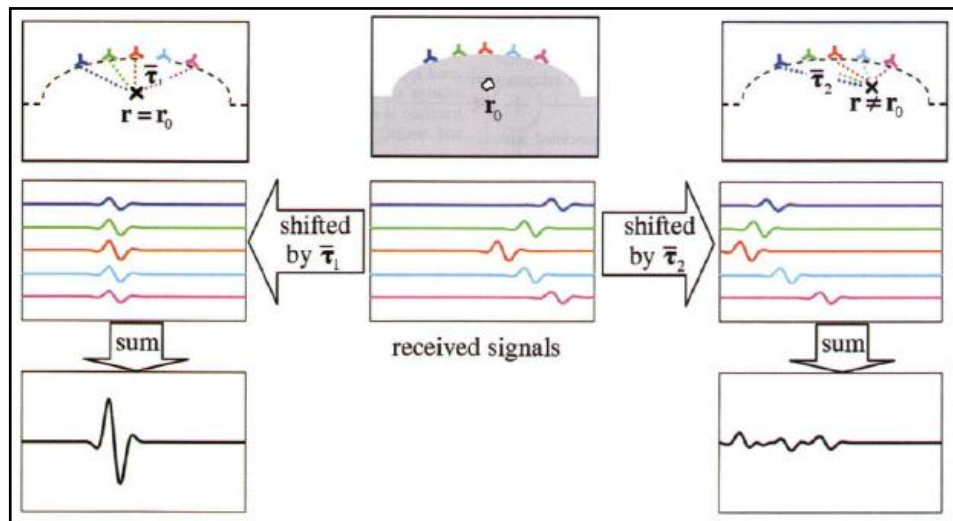
Figure 4.3. Illustration for explanation of DAS algorithm showing coherent and incoherent sum of the back-scattered signals [25]

As an example, the stacked patch antenna (in Section 3) is used to investigate the coherent and incoherent sums for a basic monostatic radar measurement set-up, as shown in Figure 4.4.
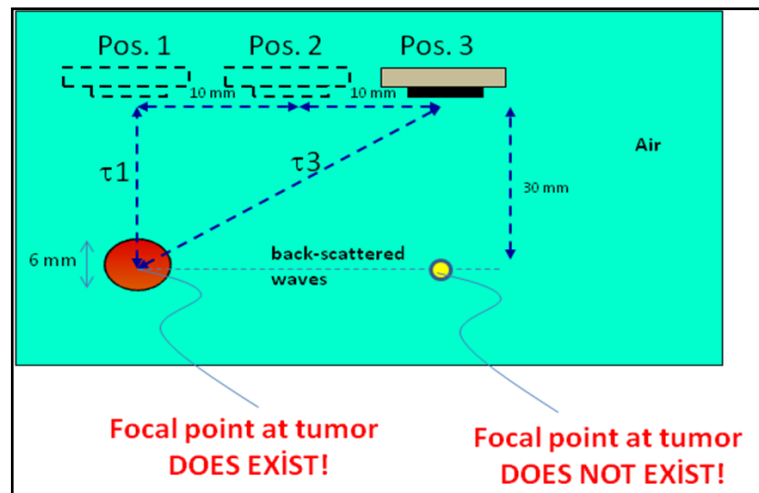
Figure 4.4. Illustration of a basic monostatic radar measurement set-up

In this case, only the S_{11} signals for the 1. and 3. antenna positions are analyzed as in Figure 4.5.
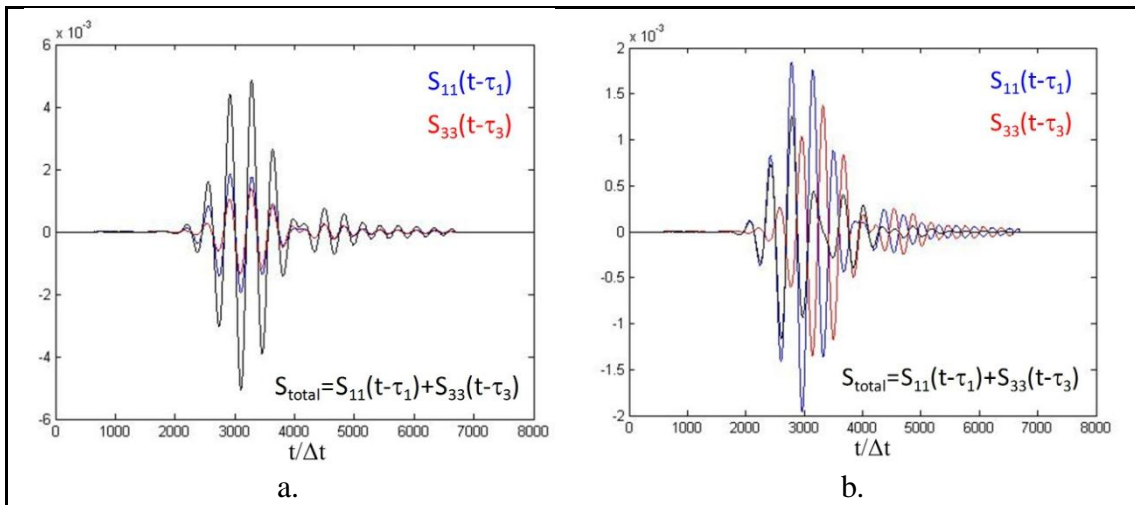
Figure 4.5. a. Coherent sum of the time-shifted signals for the focal point in which the tumor exists, and b. incoherent sum of the time-shifted signals for the focal point in which the tumor does not exist (Δt is time-step)

4.3. PRELIMINARY IMAGING STUDY WITH THE STACKED MICROSTRIP PATCH ANTENNAS
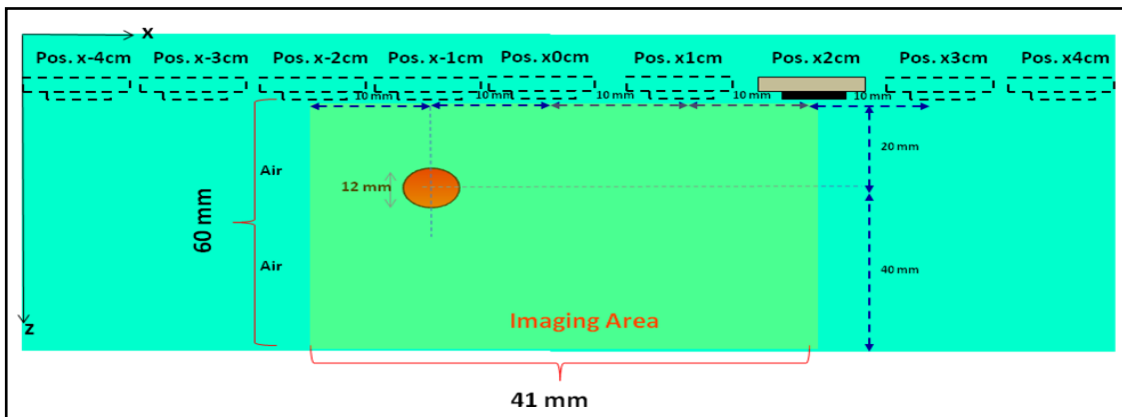
Figure 4.6. A monostatic radar based microwave imaging scenario

Nine stacked microstrip patch antennas (in Section 3) is used for the monostatic radar based microwave imaging application, as shown in Figure 4.6. Each antenna is moved along a straight line on the x-axis by 1 cm increments. The medium that antennas as well as the tumor are located is air (free space). The tumor with the diameter of 12 mm is located at 20 mm depth. Focal points (pixels) are selected as 2 mm away from each other, resulting

2 mm resolution in the imaging area. Each antenna in the array is excited by sine-modulated Gaussian pulse with an UWB frequency of 1-6 GHz, and only back-scattered time-domain signals (S_{ii}) are recorded (Figure 4.6). The imaging result successfully obtained by the DAS algorithm is given in Figure 4.7.
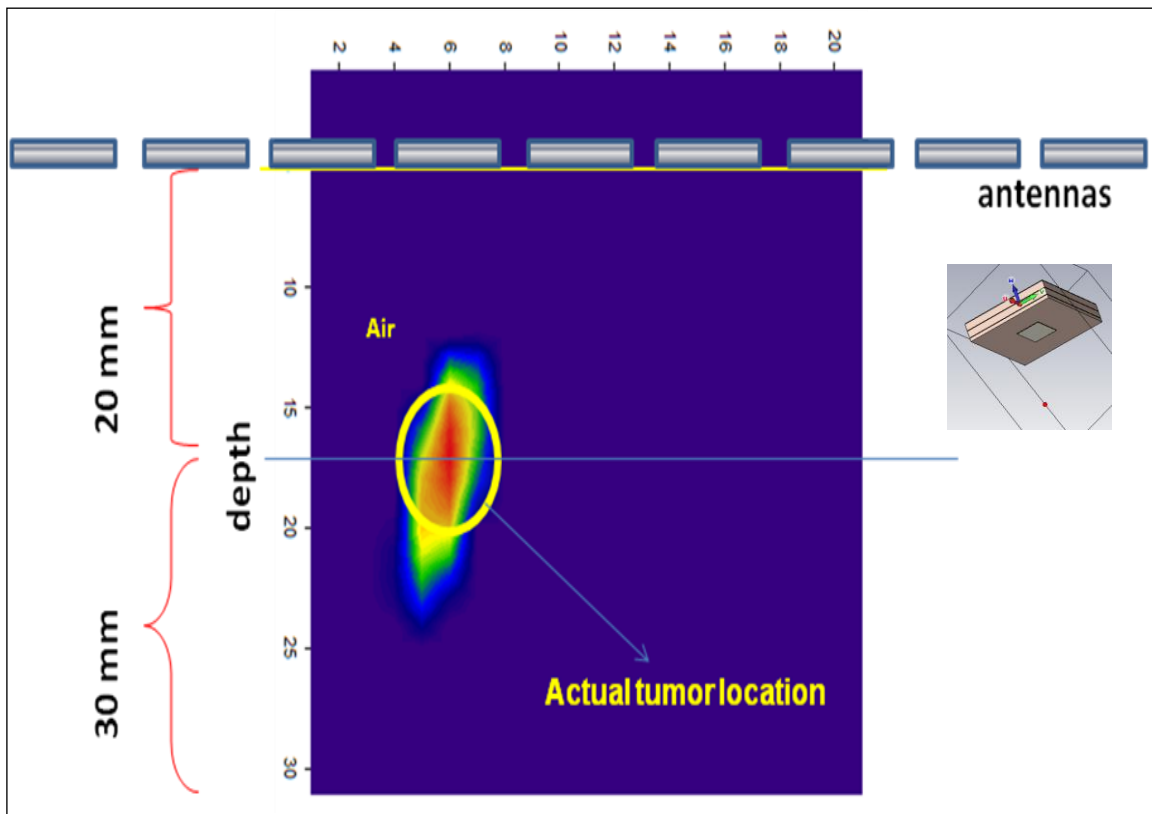
Figure 4.7. The imaging results of the monostatic radar based microwave imaging scenario with the antennas aligned along a straight line

Same antennas are also moved in a half-circular line along which each is separated by 18° for another monostatic radar-based microwave imaging system. The tumor with the diameter of 2 mm is located at 30 mm depth. The imaging result successfully obtained by the DAS algorithm is also given in Figure 4.8.
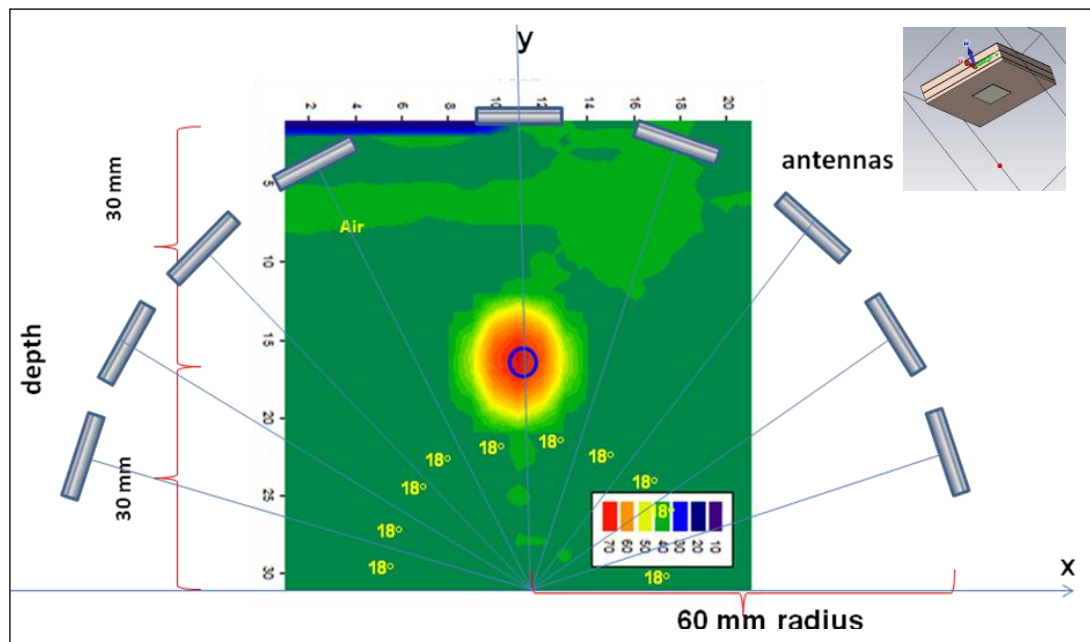
Figure 4.8. A monostatic radar based microwave imaging scenario with the antennas aligned along a circular line

It's experienced that tumor detection sensitivity has been increased around 2.5-3.0 dB when the scanning configuration along the circular line is used, compared to that along the straight line. These results coincide with the literature. The UWB antennas developed for breast cancer detection in literature were generally used and tested in planar, cylindrical or spherical scanning surfaces, as a single element or in an antenna array. There are also a lot of advantages of using circular or hemispherical antenna array configurations compared to planar ones; such as increased tumor detection sensitivity, enhancement on signal reception [114], increased illuminated coverage area inside the breast [115], better signal-to-clutter (S/C) ratio [80], etc. However, mutual coupling effects of array elements can negatively impact antenna performance and imaging results, too [76].

Moreover, five stacked patch antennas are tested for a multistatic radar-based microwave imaging system by using CST Microwave Studio©, as shown in Figure 4.9. These antennas are located in a half-circular line along which each is separated by 40° for the monostatic radar-based microwave imaging system. Each antenna in the array is excited sequentially by sine-modulated Gaussian pulse with the UWB frequency of 1-6 GHz, and back-scattered time-domain signals (S_{ii} and S_{ij}, i≠j) are recorded.
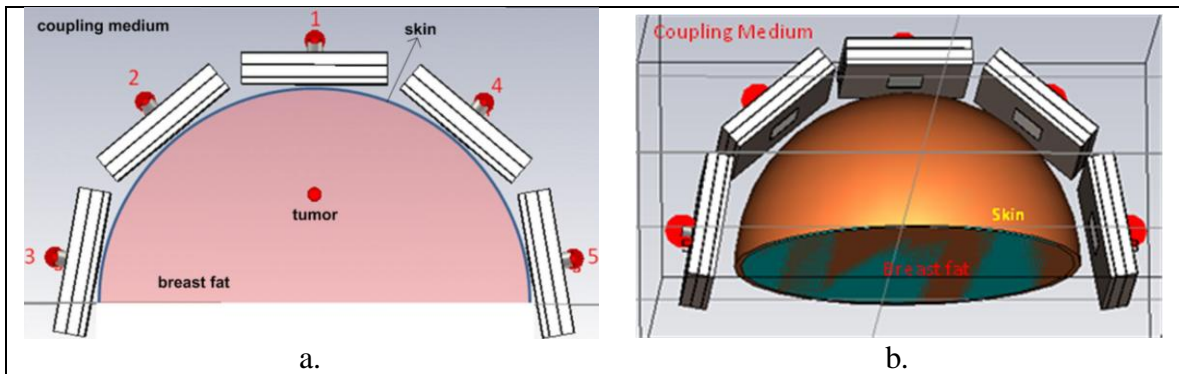
Figure 4.9. A multistatic radar based microwave imaging scnerio with the stacked microstrip patch antennas aligned along a circular line

Tumor response signals S_{ij}^T are obtained by calibrating the recorded signals as in Equation (4.1). Some of the uncompensated tumor response signals of S_{11}^T, S_{31}^T, S_{34}^T are given in Figure 4.10. It's successfully observed that time-delays between the three tumor response signals are found to be the expected theoretical values.
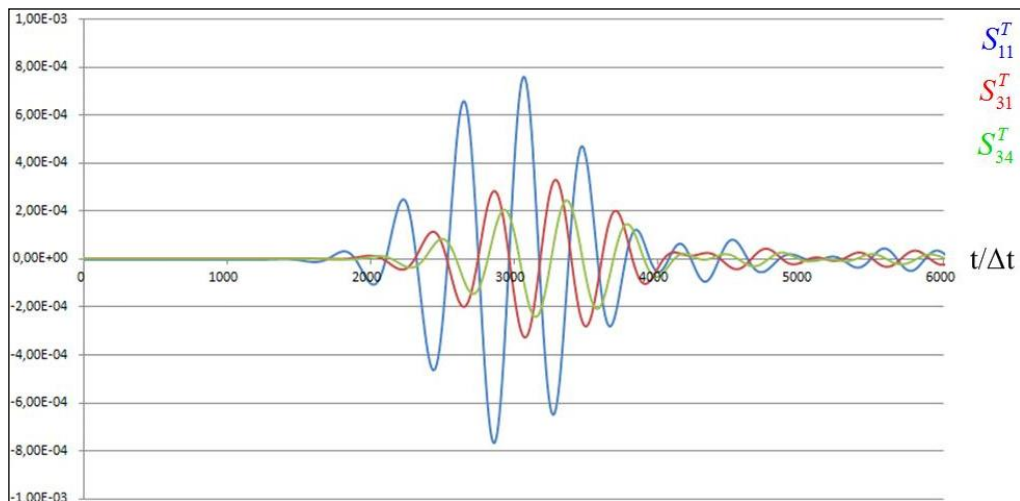
Figure 4.10. Uncompensated tumor response signals of S_{11}^T, S_{31}^T, S_{34}^T (Δt is time-step)

Although the time-delay values are correctly determined in the simulation study, this stacked microstrip patch antenna does not seem to be appropriate for microwave imaging system for breast cancer detection, because of its large size (4 cm × 4 cm) unsatisfactory bandwidth.

4.4. IMAGING STUDY WITH PLANAR BOW-TIE ANTENNAS

4.4.1. Planar Bow-Tie Antenna Design as an Array Element

The bow-tie antenna (26 mm × 40 mm), which is a basic wideband dipole antenna, presented in this sub-section is aimed to be used as an UWB probe element of a half-spherical antenna array as a part of the microwave imaging system which is operating between 1 and 8 GHz. We're interested in the 1–8 GHz frequency range; which guarantees balance between reasonable contradictory needs of better spatial resolution, better penetration depth [73], less attenuation of electromagnetic waves through the breast and smaller dimensions of a multi-function active imaging system. The selected frequency range is expected to provide reasonable tumor detection capabilities.

In particular, since the skin reflections back to the antenna adversely affect imaging results, better penetration of electromagnetic waves into the breast tissue will be determined by operating the antenna in a coupling medium whose dielectric properties are close to the breast tissue. Therefore, the array is immersed in a coupling medium to achieve the best possible matching with the breast tissue [7]. Antenna size would also be selected to be smaller since the wavelength in the coupling medium will be smaller than air. Non-dispersive dielectric properties of the coupling medium will be used in this sub-section.
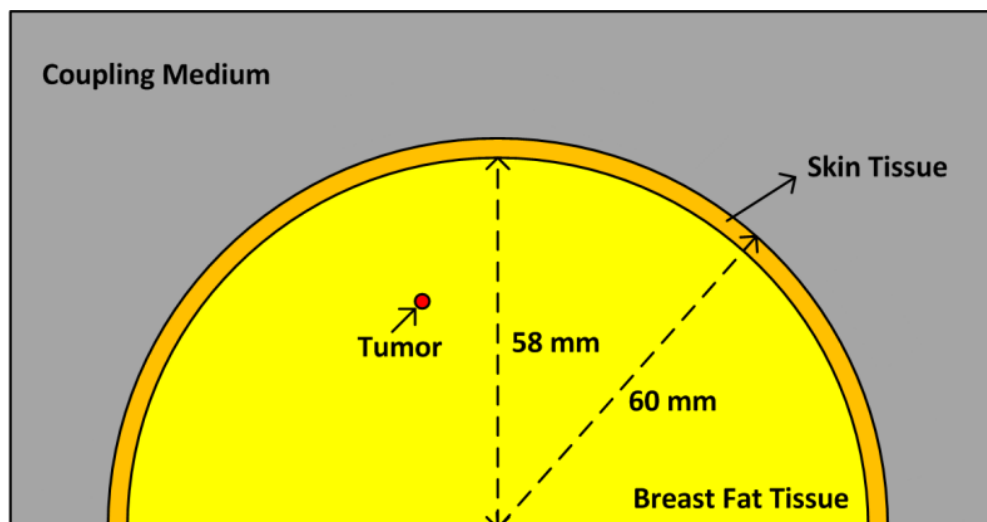
Figure 4.11. Illustration of layered homogeneous half-spherical breast phantom model

The layered breast phantom model used in this sub-section consists of a skin tissue layer with thickness of 2 mm and a half-spherical breast fat tissue model with radius of 58 mm under the skin (Figure 4.11). The model does not include spatial inhomogeneity of the breast. The homogeneous breast phantom is surrounded by a coupling medium in which antennas would be placed. The dielectric properties of the breast phantom will be selected as both non-dispersive (Table 4.1) and dispersive (Table 2.9).
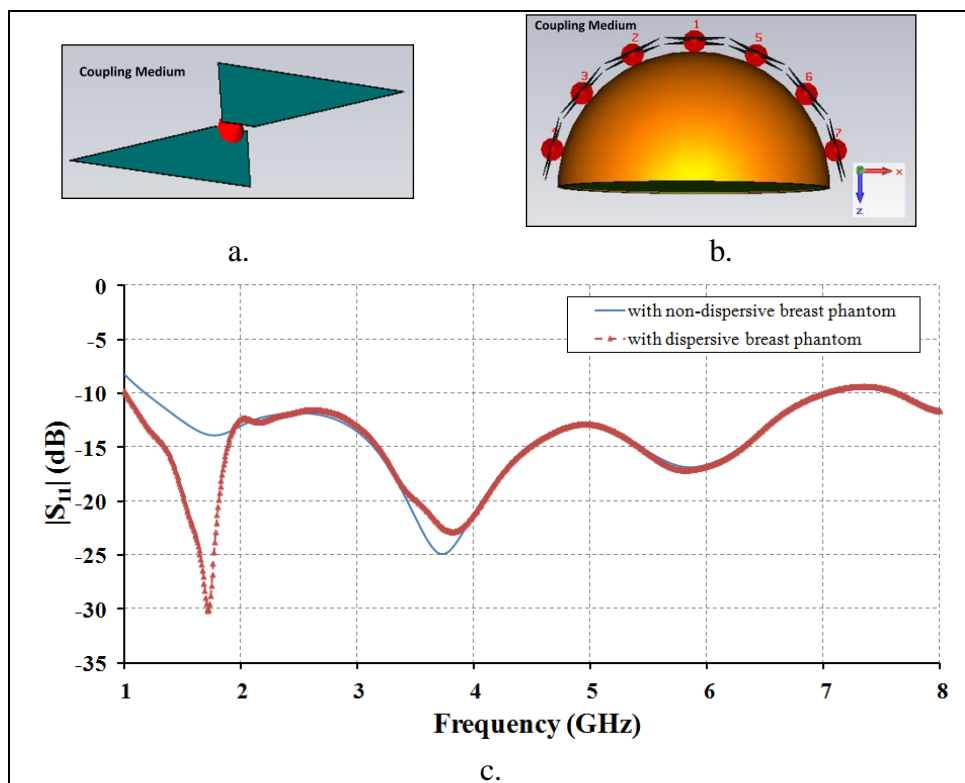
Figure 4.12. a. Bow-tie antenna, b. Simulation model of bow-tie antenna array designed in front of the breast phantom, c. Simulation results of return loss of the bow-tie antenna in the half-spherical antenna array encircling the non-dispersive and dispersive breast

The bow-tie antenna (Figure 4.12.a) is designed when it operates with other antenna elements in the half-spherical antenna array and also in front of the non-dispersive breast phantom model (Figure 4.12.b). Seven UWB bow-tie antennas are located above the homogeneous half-spherical breast phantom that is modeled on a full-wave electromagnetic simulator (CST Microwave Studio®). The design objective was optimizing the antenna geometry and size to obtain return loss less than -10 dB over the bandwidth from 1 to 8 GHz. Comparative results of return loss of the bow-tie antenna in

the half-spherical antenna array encircling the non-dispersive and dispersive breast phantom are shown in (Figure 4.12.c). Simulation results are obtained for the 1. antenna located at the center of the half-spherical antenna array, as shown in Figure 4.12.b.

The results show that the -10 dB bandwidth of the antenna which is operating in the half-spherical antenna array surrounding the breast phantom extends from around 1 GHz to above 8 GHz, with the exception of a small (around 0.7 dB) mismatch centered at 7.37 GHz, which has not been found to be important in imaging results.

The performance of the antenna while immersed in the coupling medium is also tested for cases of antenna in the array operating with non-dispersive phantom, antenna alone operating with non-dispersive phantom and antenna alone operating without non-dispersive phantom, respectively (Figure 4.13).
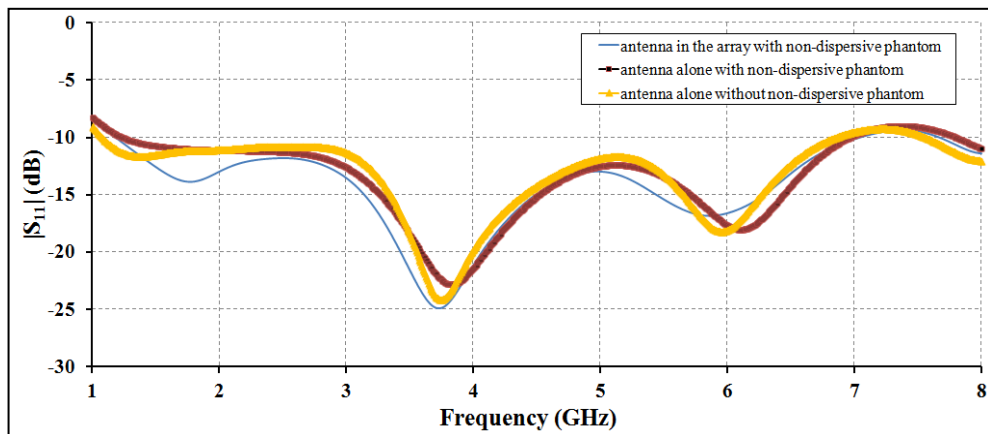
Figure 4.13. Comparative simulation results of return loss of the bow-tie antenna in the array operating with non-dispersive phantom, antenna alone operating with non-dispersive phantom and antenna alone operating without non-dispersive phantom

Slightly better matching results have been obtained for the antenna operating with dispersive breast phantom, in all, at different resonance frequencies. According to the results in Figure 4.12 and Figure 4.13, these resonance frequencies are slightly affected by dispersive properties of breast phantom as well as other antenna elements in the half-spherical array configuration. The presence of the phantom also affects them, too. However, the overall UWB performance of the bow-tie antenna in the presence of the

phantom and other array elements has been kept same over the bandwidth from 1 to 8 GHz.

The wavelength at the center frequency (4.5 GHz) is 22 mm inside the coupling medium. The antenna-skin distance has been obtained as 4.71 mm, by optimizing the distance with parametric sweep for the purpose of best matching over the bandwidth. This value is close to the expected distance which is theoretically quarter-wavelength at the center frequency [98].

4.4.2. Analysis of Dispersive Effects on Tumor Detection Capability of UWB Microwave Imaging System

It's been reported that frequency dispersive dielectric properties of surrounding coupling medium affect antenna performance as well as tumor detection capability of the microwave imaging system [116]. Dielectric properties of human body tissues vary over a considerable UWB operation frequency band [14, 79]. As electromagnetic pulse propagates in a dispersive medium, it's distorted inside the medium depending on the frequency dispersive behaviour of the dielectric properties of the medium [117, 118]. Therefore, dispersive properties of breast phantom as well as surrounding coupling medium should also be considered for the microwave imaging system.

As the UWB microwave imaging system operates in the time domain by sending a narrow pulse to penetrate the breast and measure the scattered pulses, the bow-tie antenna used in our system should introduce low distortion in the time domain [7]. It's important to study distortion when the radiated pulse propagates through the breast tissues. For this purpose, the transmitted pulse from the 1. antenna located at the center of the half-spherical antenna array is monitored at different distances normal from the antenna aperture. The time domain performance of the antenna when it operates in front of the phantom is shown in Figure 4.14 for the cases with dispersive and non-dispersive breast phantom models, respectively.
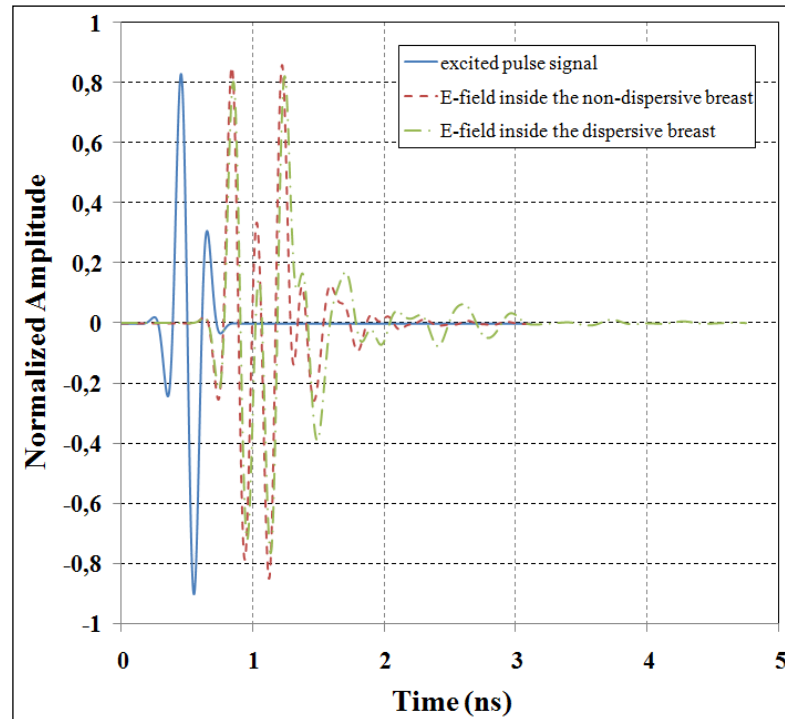
Figure 4.14. The excited and transmitted pulses inside the dispersive and non-dispersive breast phantoms, at 30 mm depth

In order to find out the distortion level in the transmitted pulses inside the breast phantom model, the fidelity factor is calculated at different locations within the breast phantom. The fidelity factor is defined as the maximum magnitude of the cross correlation between the observed pulse ($s_R(t)$) at a certain distance and the excitation pulse ($s_T(t)$) [119]:

$$F = \max_{\tau^d} \frac{\int\limits_{-\infty}^{\infty} s_T(t) s_R\left(t - \tau^d\right) dt}{\sqrt{\int\limits_{-\infty}^{\infty} \left|s_T(t)\right|^2 dt \cdot \int\limits_{-\infty}^{\infty} \left|s_R(t)\right|^2 dt}} \tag{4.4}$$

where τ^d is the required time delay for obtaining maximum magnitude of the cross correlation.

The result in Figure 4.15 indicates an increasing pulse distortion as the signal propagates through the breast phantom due to the reflections in the layered phantom model. For the case with dispersive breast phantom, the fidelity factor decreases more and it becomes

63.93 per cent at 30 mm depth inside the breast. However, the fidelity factor is kept at slightly higher values when the breast phantom is non-dispersive. It's more than 68.10 per cent at 30 mm depth inside the breast. The fidelity factor of the case with dispersive breast phantom is less than the case with the non-dispersive one, as expected, due to increasing pulse distortion in dispersive dielectric tissues [117]. If the phantom model would be heterogeneous including gland tissues inside the breast, the fidelity factor is expected to decrease sharply due to the multiple reflections in the heterogeneous phantom [7]. On the other hand, for the bow-tie antenna presented in this paper, the fidelity factor is within reasonable values (more than 60 per cent) even inside the breast phantom [84].
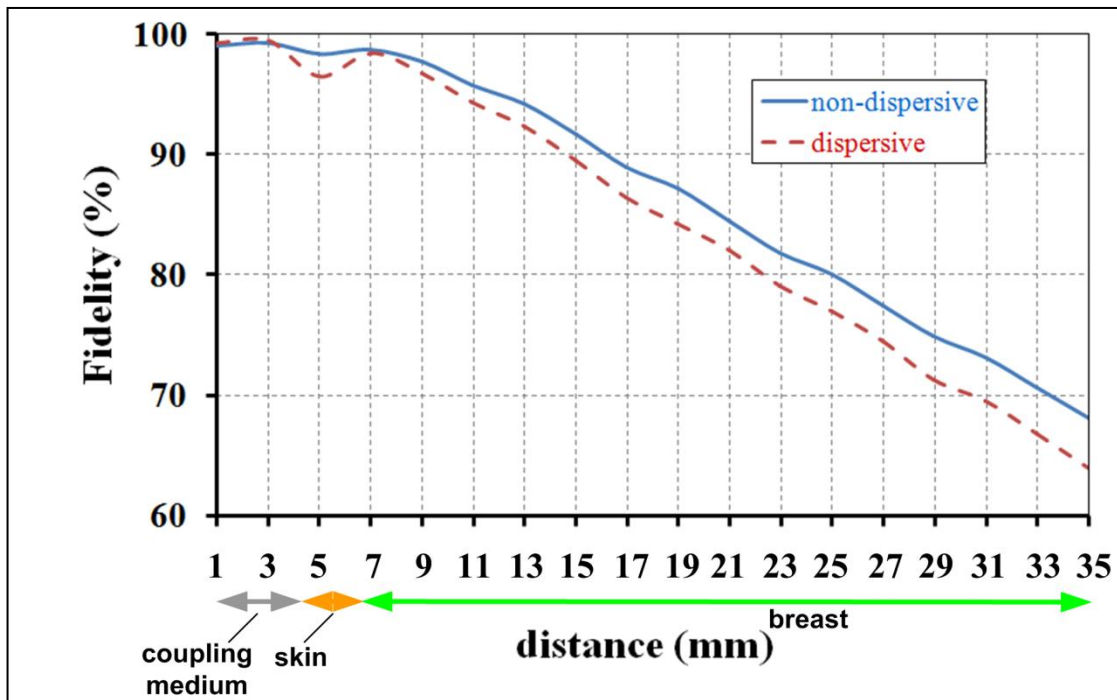
Figure 4.15. Calculated fidelity factor with respect to distance from the antenna, in the presence of non-dispersive and dispersive breast phantoms

When one of the seven UWB bow-tie antennas in the array is excited by sine-modulated Gaussian pulse, back-scattered time-domain signals (S_{ii} and S_{ij}, $i \neq j$) are recorded. This procedure is repeated by feeding each antenna sequentially, for the cases with and without 2 mm diameter tumor. 49 time-domain signals coming from different antennas are recorded for each case. Tumor response signals s_{ij}^{T} are obtained by calibrating the recorded signals as in Equation (4.1).

Imaging results of breast cancer tumor with 2 mm diameter are obtained by using the DAS algorithm (Figure 4.16). The tumor with 2 mm diameter is successfully detected at its actual location, for the non-dispersive case, as shown in Figure 4.16.a. On the other hand, it is also detected at a distance around 6 mm far away from its actual location, with decreased signal levels for the dispersive case, as shown in Figure 4.16.b. Frequency dispersive phase velocities of electromagnetic fields had been kept constant as it was done in the non-dispersive case. Therefore, the reason of detection of the tumor at a faulty location obviously depends on wrong computation of time delays used in the DAS algorithm.
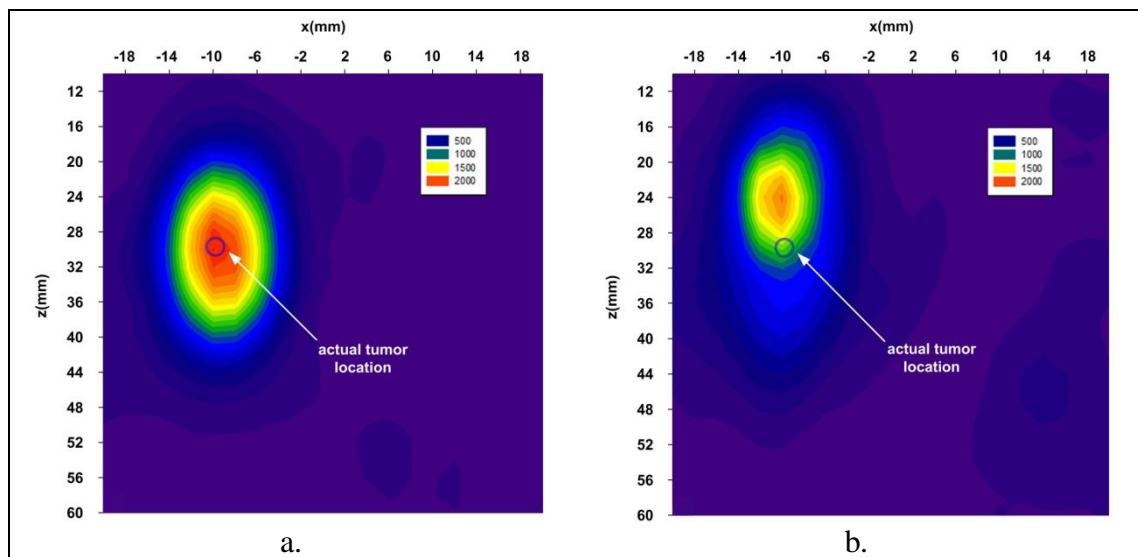
Figure 4.16. Images of breast cancer tumor with 2 mm diameter for the cases with a. non-dispersive and b. dispersive breast phantoms

Moreover, if one compares the dispersive breast phantom to the non-dispersive phantom from calculated total tumor response levels point of view, signal reduction of 0.628 dB is observed in the dispersive case. This reduction is possibly related with slightly worse pulse distortion performance of the antenna operating with the dispersive breast phantom, and also incoherent summing of the inaccurate delayed signals, because of the frequency dispersive phase velocities of electromagnetic fields. Therefore, new imaging algorithms compensating the dispersive effects, such as "Microwave Imaging via Space-Time" (MIST) beamforming [24], should be used in the design of the microwave imaging system. On the other hand, more realistic values of dispersive dielectric properties [62] and spatial

inhomogeneity [7, 73, 120] should be included in the breast phantom model to observe the feasibility of the microwave imaging system better.

In this sub-section, an UWB bow-tie antenna array surrounding the breast has been designed and tested on a full-wave electromagnetic simulator, in order to investigate the effects of frequency dispersive dielectric properties of the half-spherical breast phantom on breast cancer tumor detection capability of the microwave radar-based imaging system. Obtained simulation results are reasonably reliable. Time domain behavior of the antenna operating with the dispersive breast phantom has indicated slightly worse pulse distortion performance through the breast. Images of the detected spherical tumor with 2 mm diameter have been formed by using the DAS algorithm which is not found to be suitable for the frequency dispersive breast tissues. Therefore, better imaging algorithms compensating the dispersive effects are needed to be used with more realistic heterogeneous breast phantom models, too.

4.5. IMAGING STUDY WITH SPHERICAL CONFORMAL BOW-TIE ANTENNAS

4.5.1. Spherical Conformal Bow-Tie Antenna Design as an Array Element

Several different types of antennas have been considered and reported over the past decade by research groups involved in radar-based UWB breast imaging; such as UWB planar bow-tie [70], ridged pyramidal horn [24], cross-polarized types [71, 72], U-slot [73, 74], antipodal Vivaldi [75], stacked microstrip patch [69, 74], tapered slot [7], dielectric resonator antennas [4], and MEMS-steerable antennas [4], etc. These antennas were generally used and tested in planar, cylindrical or spherical scanning surfaces, as a single element or in an antenna array.

Although an antenna array system is applicable and mostly preferred for real breast tumor detection systems, mutual coupling effects between array elements would certainly affect the measurement results [76]. If one antenna element of the array sends UWB electromagnetic waves through the breast, unwanted currents are induced on the nearby antenna elements which results distortion of the measurement results (See Figure 1.11). In

order to detect the weak reflections from small tumors located in tissues ranging from fatty breast to glandular, a high sensitive antenna is required to send and receive electromagnetic waves with low pulse distortion and low mutual coupling effects in the array. Since antennas are assumed to be operating in the near field region in which spherical waves exist, antenna geometry and polarization should be appropriately selected to perfectly match with the spherical waves inside the breast, too [78].

For this purpose, this study mainly presents herein spherical conformal bow-tie antennas to improve tumor detection capability of the microwave imaging system. Conventional planar UWB bow-tie antennas are curved onto a hemi-sphere surface to investigate its effects on enhancement of tumor responses and signal energies, as well as that of mutual coupling levels between array elements and pulse distortion performance.

Use of the spherical conformal antenna structure is presented here for breast cancer imaging, and it's aimed to be used as an element of a half-spherical array encircling the breast as part of a microwave imaging system operating between 1 and 8 GHz. The intended use of conformal antenna is expected to increase the dynamic range of the system as well as to diminish mutual coupling effects between array elements and pulse signal distortion through the breast.

The planar bow-tie antenna (26 mm × 40 mm) (in Section 4.4) which is curved onto a hemi-sphere surface is aimed to be used as an UWB probe element of a half-spherical antenna array (Figure 4.17.a). The array is assumed to be immersed in a coupling medium to reduce adverse effects of signal reflections at the antenna-air-breast interface. The antenna-skin distance has been set as 4.71 mm, as it was the same case in Section 4.4.

The conformal bow-tie antenna is designed for operating with other antenna elements in the half-spherical antenna array and also in front of the breast phantom model (Figure 4.17.b). The homogeneous fatty breast, quasi-heterogeneous and homogeneous fibro-glandular phantom models representing "mostly fatty", "heterogeneously dense" and "very dense" phantom models, respectively, will be used for comparative simulation results in this study (Section 4.1). The design objective is optimization of the antenna geometry and size to obtain return loss less than -10 dB over the frequency band from 1 to 8 GHz.

Comparative results of return loss of the conformal bow-tie antenna encircling different breast phantom models are shown in (Figure 4.17.c). The simulation results are obtained for the 1. antenna located at the center of the half-spherical antenna array, as shown in Figure 4.17.b.
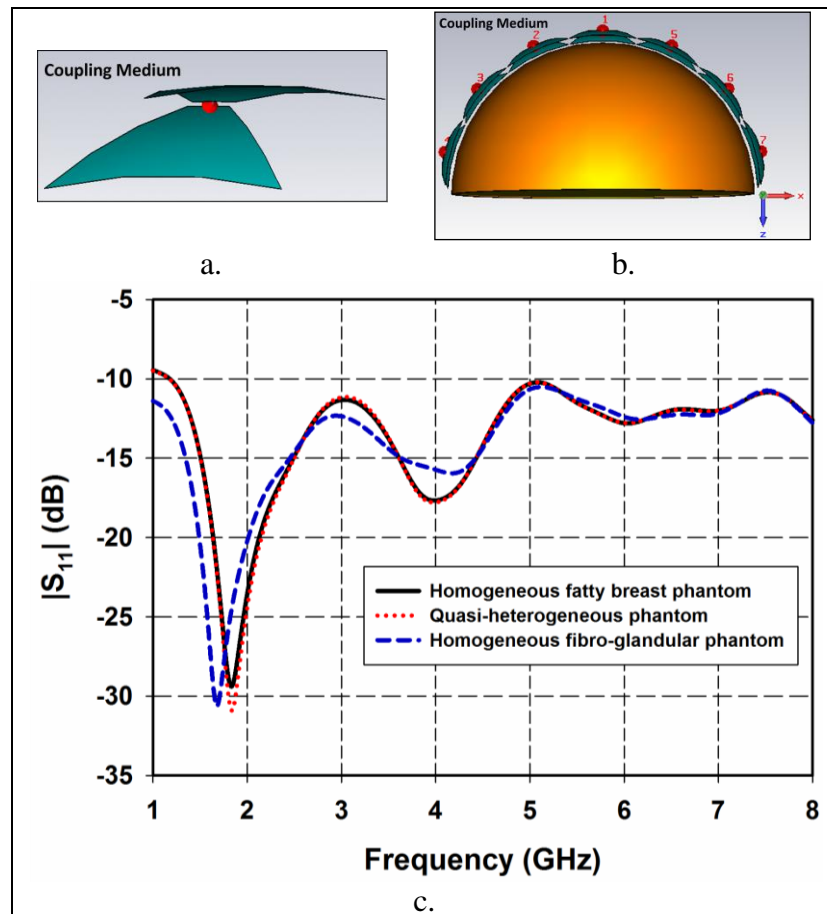
Figure 4.17. a. Spherical conformal bow-tie antenna, b. Simulation model of spherical conformal bow-tie antenna array in front of the breast phantom, c. Return loss of the spherical conformal bow-tie antenna in the half-spherical antenna array encircling different breast phantoms

The results show that the -10 dB bandwidth of the antenna which is operating in the half-spherical antenna array surrounding all kinds of the breast phantom models extends from nearly 1 GHz to above 8 GHz. The radiation pattern results for 1. antenna excited and located at the center of the half-spherical antenna array are given for different operation frequencies, in Figure 4.18.
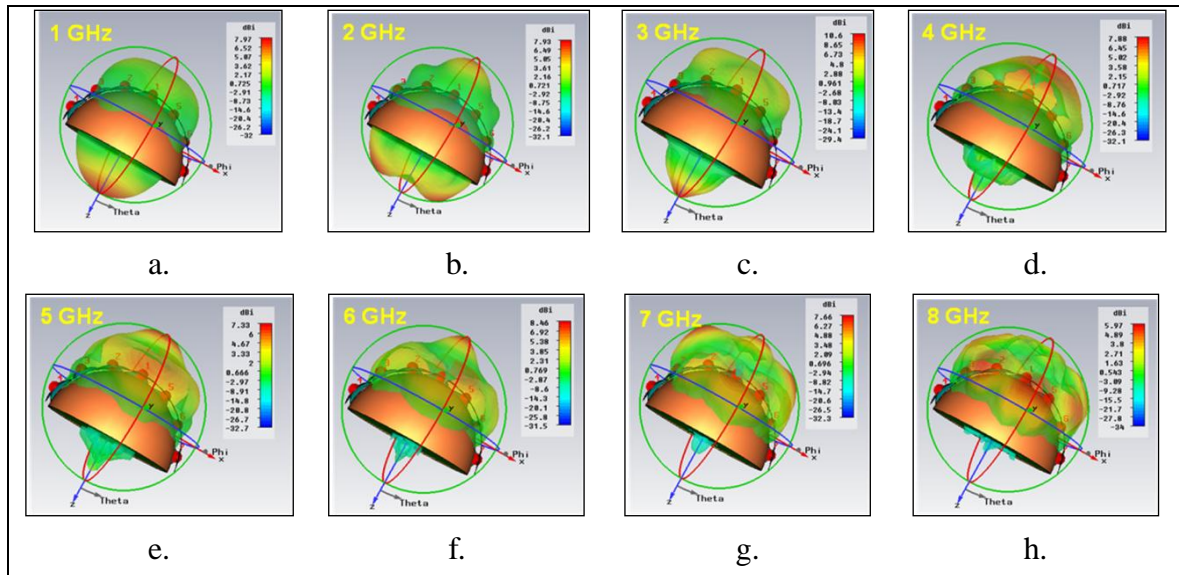
Figure 4.18. Radiation pattern results for 1. antenna excited and located at the center of the half-spherical antenna array are given for different operation frequencies

It's observed that the skin reflection increases as the operation frequency increases. These results also show that there exist still skin reflections at high frequencies, in spite of the use of coupling medium. Although the signal levels decrease inside the breast in some cases, an equalization procedure is done in the imaging algorithm, called "compensation", to overcome this situation, too.

4.5.2. Imaging Results with Different Array Configurations

The tumor detection sensitivity had been increased around 2.5-3.0 dB when the stacked microstrip patch antenna scanning configuration along the circular line was used, compared to that along the straight line, in Section 4.3. Moreover, there are a lot of advantages of using circular or hemispherical antenna array configurations compared to planar ones; such as increased tumor detection sensitivity, enhancement on signal reception, increased illuminated coverage area inside the breast, better signal-to-clutter (S/C) ratio, etc. as mentioned before. In this study, contribution of spherically conformal UWB bow-tie antennas for use in a conformal antenna array configuration on enhancement of image quality and breast tumor detection capability is investigated by simulation studies.
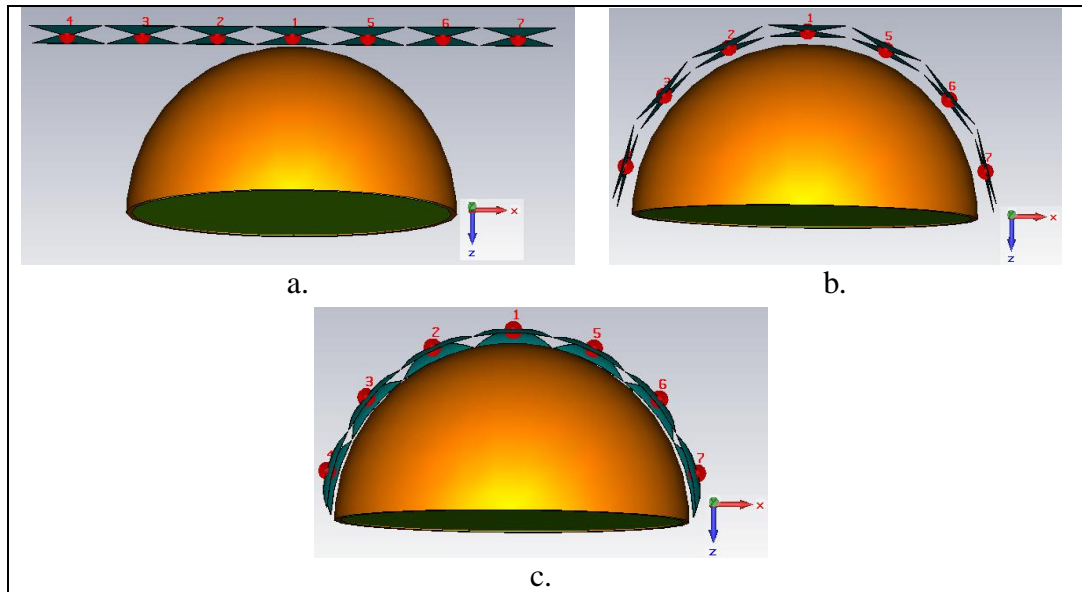
Figure 4.19. Simulation models of a. planar bow-tie antennas aligned along a planar surface tangent onto the hemisphere surface, b. planar bow-tie antennas aligned as encircling the breast phantom, c. spherical conformal bow-tie antennas aligned as encircling the breast phantom

There are three kinds of array configuration models used in this study such as; planar bow-tie antennas aligned along a planar surface tangent onto the hemisphere surface, planar bow-tie antennas aligned as encircling the breast phantom, and spherical conformal bow-tie antennas aligned as encircling the breast phantom [121] (Figure 4.19). The comparison of uncompensated S_{31}^T signals for three different array configurations is given in Figure 4.20, as an example. The computed signal energy as well as peak-to-peak value of the uncompensated S_{31}^T signal which is obtained in the spherical conformal antenna case is found to be greater than that of other two cases. The same situation has been observed for all other S_{ij}^T signals, too.
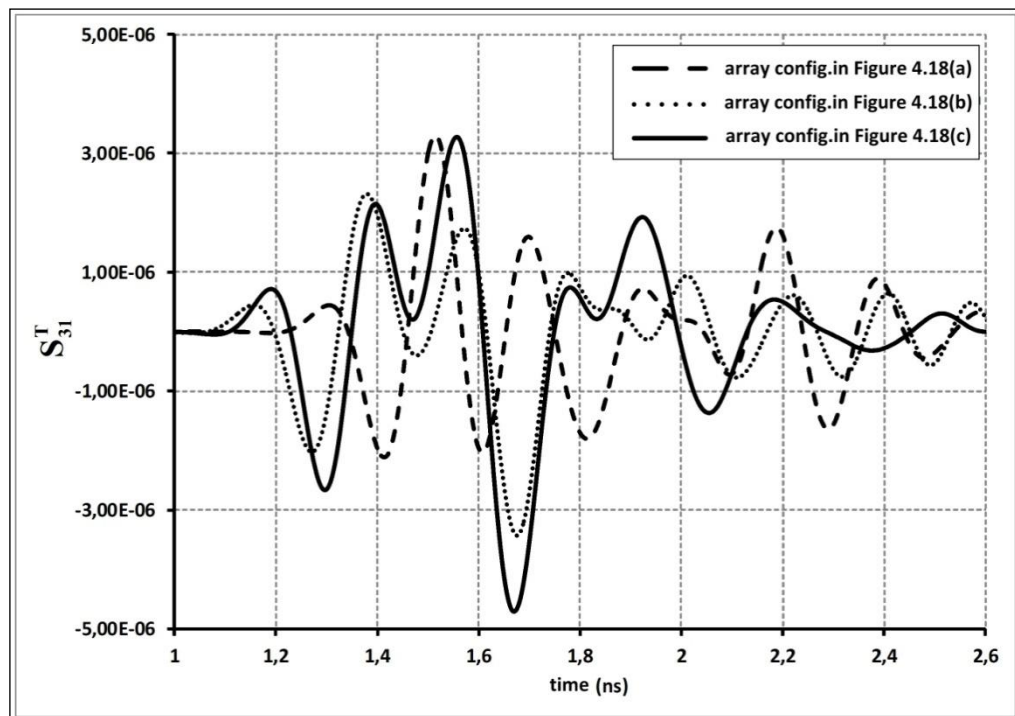
Figure 4.20. Comparison of uncompensated S_{31}^T signals for three different array configurations

If one compares the imaging results, obtained by delay-and-sum (DAS) algorithm for detecting tumor with 2 mm diameter, of these new conformal bow-tie antennas operating in coupling medium and in front of breast phantom model at 1-8 GHz frequency range, with the imaging results of planar bow-tie antennas aligned as encircling the breast and planar bow-tie antennas aligned along a planar surface tangent onto the hemisphere surface, enhancement on signal reception has been observed by around 2.5-3.0 dB. (See Figure 4.21)

These results show that the spherical conformal bow-tie antenna would be an attractive candidate element for radar-based breast cancer detection to achieve good polarization matching with spherical waves inside the breast, because of its spherical conformal geometry.
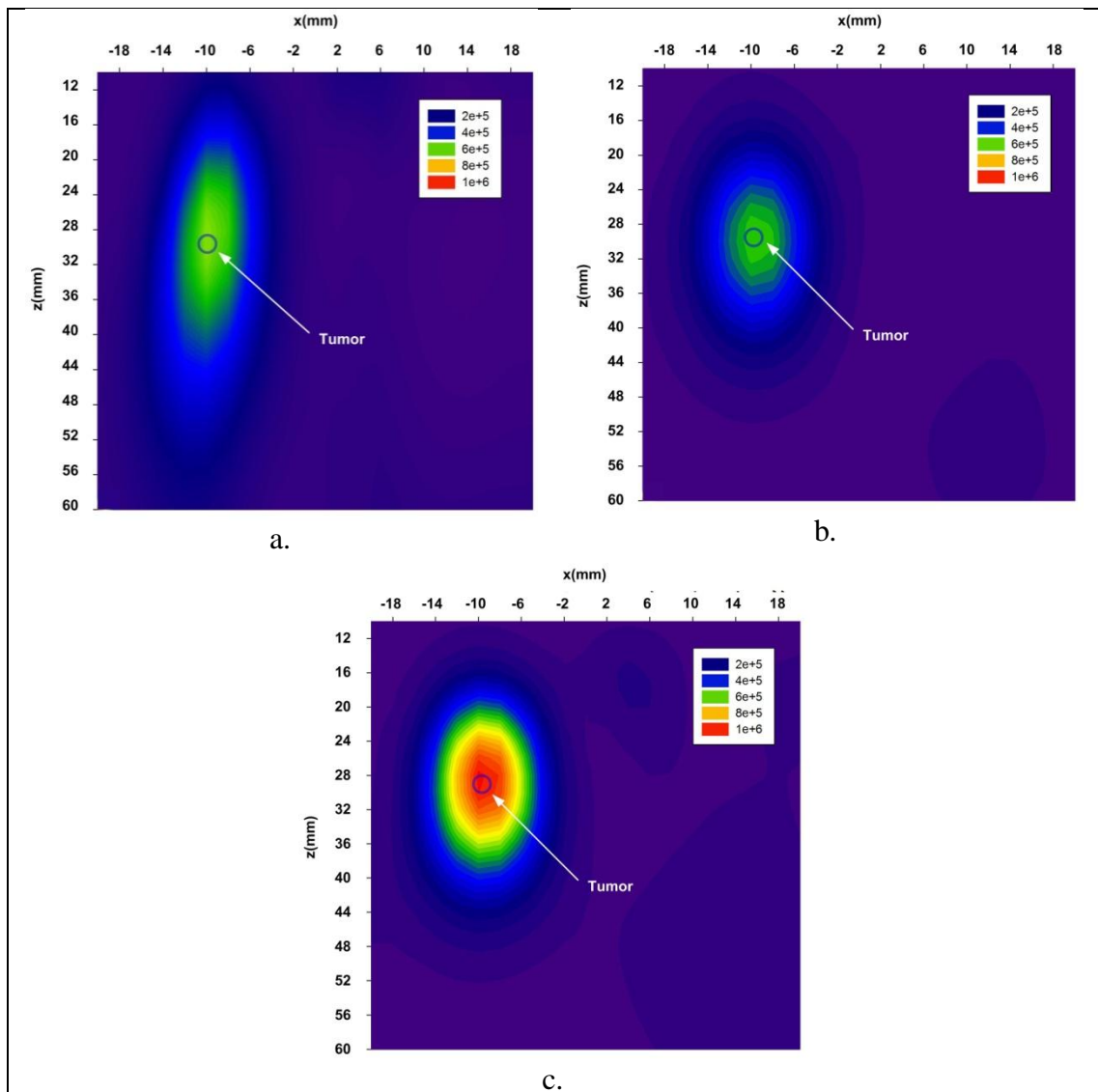
Figure 4.21. Imaging results of a. planar bow-tie antennas aligned along a planar surface tangent onto the hemisphere surface, b. planar bow-tie antennas aligned as encircling the breast phantom, c. spherical conformal bow-tie antennas aligned as encircling the breast phantom

4.5.3. Comparative Analysis of Fidelity and Mutual Coupling Effects for Conformal and Planar Bow-Tie Antennas

As the UWB microwave imaging system operates in the time domain by sending a narrow pulse to penetrate the breast and measures the scattered pulses, it's important to study distortion when the radiated pulse propagates through especially the quasi-heterogeneous breast phantom [7], which is explained in Section 4.1. The time domain performance of the

conformal bow-tie antenna will be compared to that of the planar bow-tie antenna, as in Figure 4.22. For this purpose, the transmitted pulse from the 1. antenna located at the center of the half-spherical antenna array is monitored at different distances normal from the antenna aperture, as shown in Figure 4.23.

a.   b.
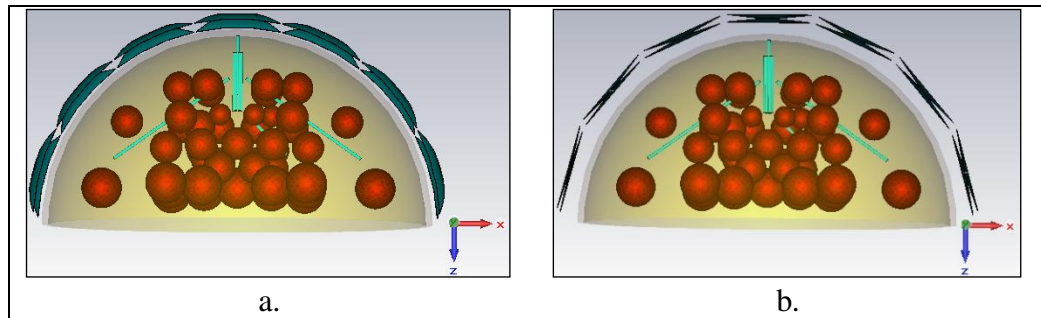
Figure 4.22. a. Spherical conformal bow-tie antennas and b. Planar bow-tie antennas, in the presence of quasi-heterogeneous breast phantom model

In order to find out the distortion level in the transmitted pulses inside the breast phantom model, the fidelity factor is calculated at different locations within the breast, as expressed in Equation (4.4).
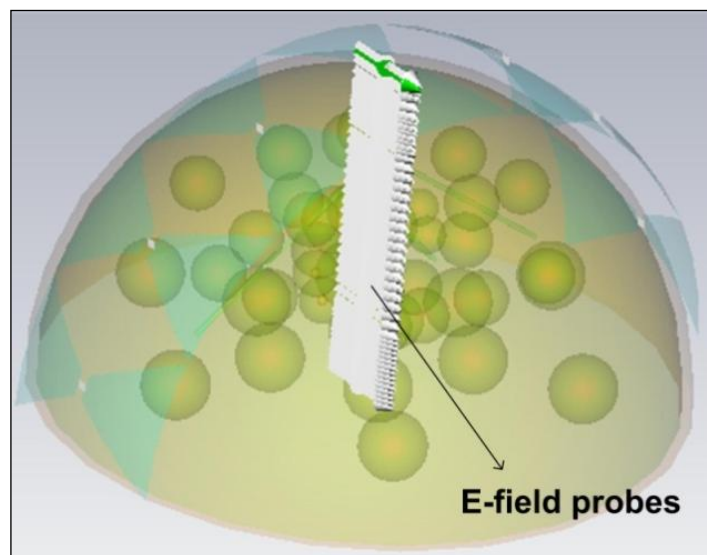
Figure 4.23. The transmitted pulse is monitored via E-field probes in CST Microwave Studio©

The results in Figure 4.24 indicate an increasing pulse distortion as the signal propagates through the quasi-heterogeneous breast phantom due to the multiple reflections inside the phantom model [7].
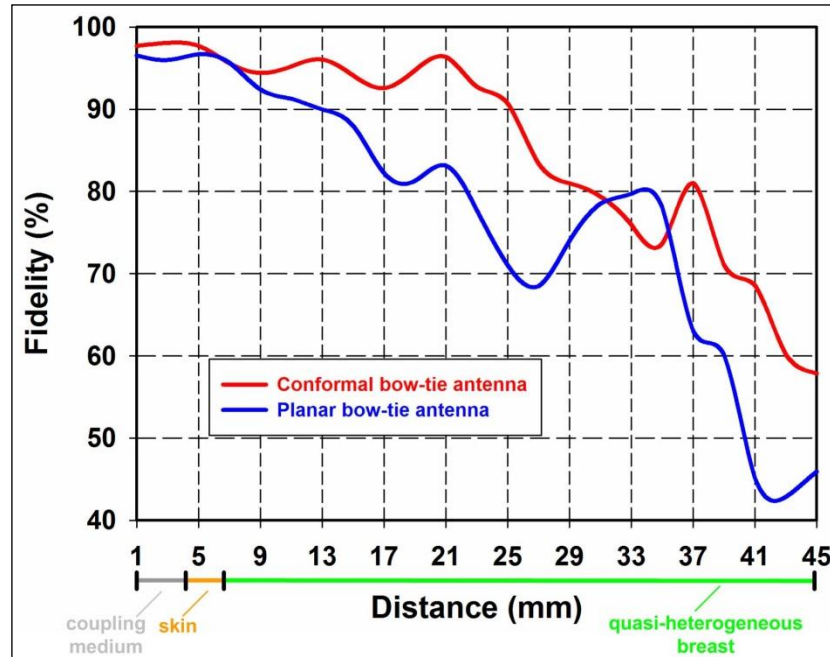
Figure 4.24. Calculated fidelity factors with respect to distance from the antenna, in the presence of quasi-heterogeneous breast phantom model

For the case with planar bow-tie antenna, the fidelity factor decreases more and it becomes 45.16 per cent at 40 mm depth inside the breast (Figure 4.24). On the other hand, the fidelity factor is kept at higher values in overall when the antenna is spherical conformal bow-tie. That's around 58.22 per cent at 40 mm depth inside the breast. Moreover, for the conformal bow-tie antenna presented in this paper, the fidelity factor is within reasonable values (around more than 60 per cent) even inside the breast phantom [84].

In order to find out mutual coupling effects of array elements in Figure 4.22, conformal and planar bow-tie antennas are compared to each other for S_{21} characteristics between 1. and 2. antennas, as shown in Figure 4.25. It's observed that the overall S_{21} characteristics of the conformal antenna show less mutual coupling effects, with the exception of higher coupling effects in around 1-1.3 and 3.6-5 GHz frequency bands. However, these bands correspond to 24 per cent of the whole band. Moreover; the areas under the curves of S_{21}

characteristics versus frequency for the conformal antenna are less than that of the planar antenna, indicating low mutual coupling effects in overall.
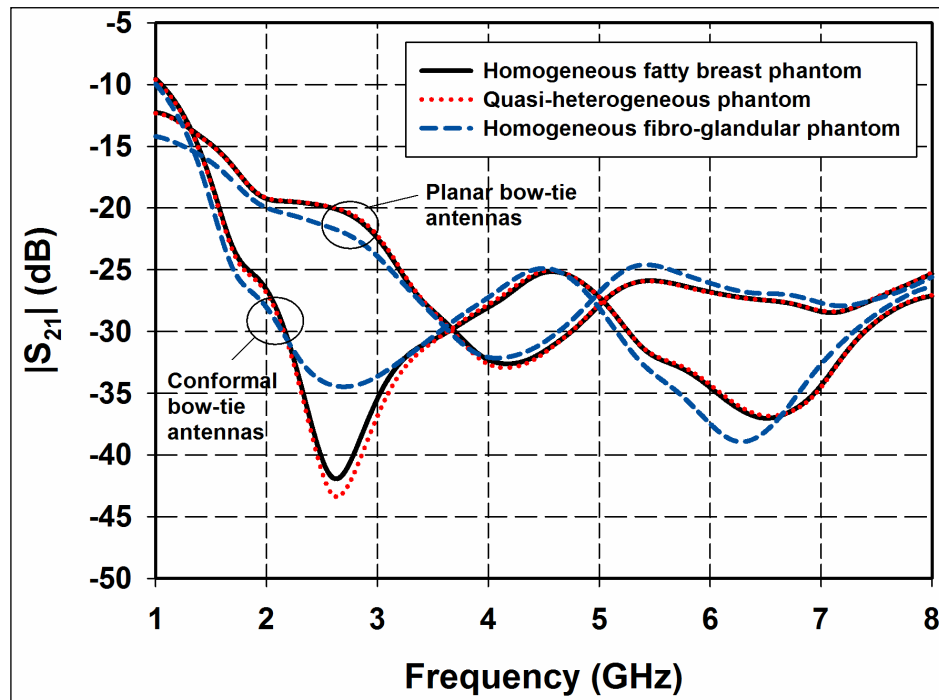
Figure 4.25. Comparable S_{21} characteristics of conformal and planar bow-tie antennas in the half-spherical antenna array encircling different breast phantoms

4.5.4. Comparative Analysis of Tumor Response and Imaging Results for Conformal and Planar Bow-Tie Antennas

Firstly, the effect of spherical conformal antenna structure on the tumor response will be compared to that of the planar bow-tie antenna. Three different breast phantom models are used in the simulations. Since the peak-to-peak voltage of the excitation pulse is 1.73 V, the tumor response (in dB) is calculated using the "uncompensated" time-domain tumor response signals S_{ij}^{T}, as follows [8]:

$$Tumor\ Response\,(dB) = 20 \cdot \log \left(\frac{\left(S_{ij}^{T} \right)_{peak-peak}}{1.73} \right) \qquad (4.5)$$

Tumor responses (in dB) corresponding to highest signal levels S_{i2}^T and lowest signal levels S_{i7}^T, are given in Figure 4.26, with comparable results for conformal and planar bow-tie antennas operating in the presence of different breast phantom models. Each neighbor tumor antenna is separated by 25° with respect to the bottom center of the breast phantom (0, 0, 60 mm). As an example, in the case of S_{42}^T, S_{12}^T and S_{72}^T tumor response signals, ψ_a is equal to -75°, 0°, and 75°, respectively (See Figure 4.2).
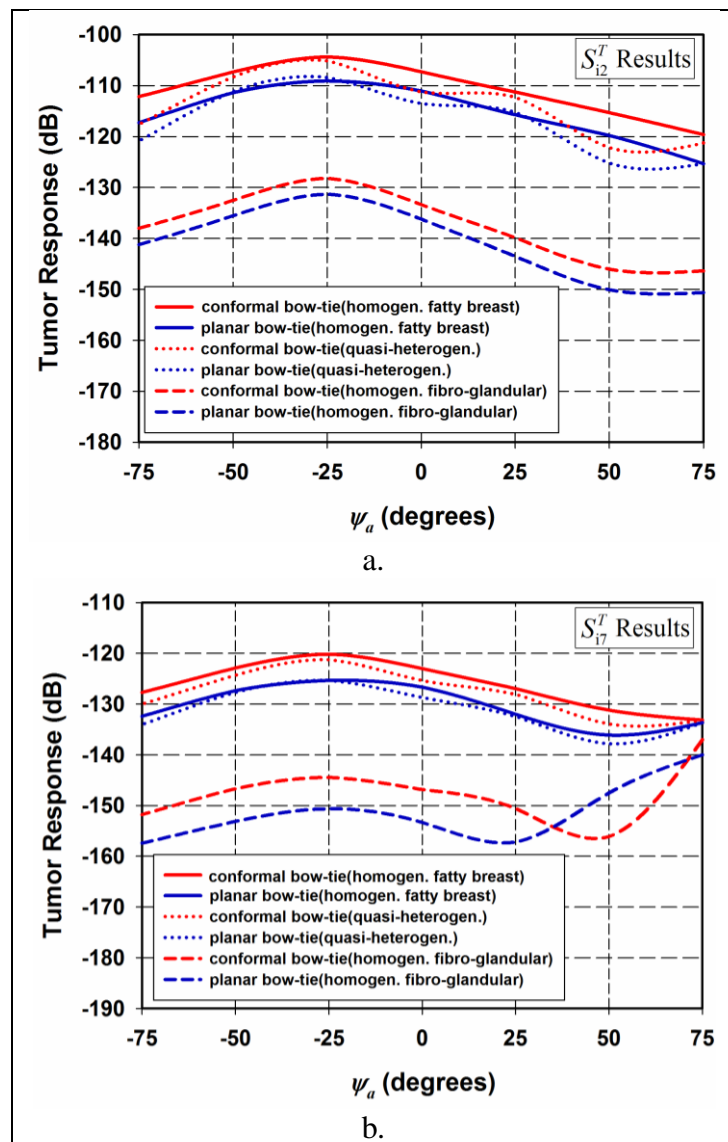
Figure 4.26. Results of tumor responses (dB) corresponding to a. S_{i2}^T and b. S_{i7}^T, with respect to ψ_a

Comparing the calculated tumor response levels of the conformal bow-tie antenna with those of the planar bow-tie antenna, they increase when the conformal antennas are used (Figure 4.26). Signal enhancement is observed between 2.27 dB and 5.70 dB in overall for the conformal antenna case. The reduction of tumor responses in the planar bow-tie antenna case is possibly related with worse pulse distortion and mutual coupling performances. The conformal structure also achieves good polarization matching with spherical waves inside the breast, because of its spherical conformal geometry, too. The tumor response levels of S_{67}^T and S_{77}^T show unexpected increment for the case of antennas operating in the presence of homogeneous fibro-glandular breast phantom, as shown in Figure 4.26.b. Obtained low level signals (S_{67}^T and S_{77}^T) are found to be masked by higher noise level in the simulation software, resulting wrong computation of tumor responses.

On the other hand, the peak tumor responses of the conformal antenna for both S_{i2}^T or S_{i7}^T are found about 1 dB and 23 dB larger when the antenna is operated in the presence of homogeneous fatty breast and quasi-heterogeneous phantoms, respectively, than when it's operated in the presence of homogeneous fibro-glandular breast phantom. The tumor response results, in Figure 4.26, also show dynamic range requirements for the detection of the tumor with 2 mm diameter at 40 mm depth. Since dynamic range of a vector network analyzer can reach down to -140 dB for experimental measurements [122], the tumor responses are not high enough to detect the tumor embedded in the homogeneous fibro-glandular breast, mimicking very dense breast tissue.

Moreover, the area under the curves of tumor responses versus different ψ_a angles decreases as the breast becomes denser with fibro-glandular tissues. As expected, these results also show that detecting tumor in homogeneous fatty breast tissue is easier than in quasi-heterogeneous and homogeneous fibro-glandular tissues, respectively.

Normalized imaging results of breast cancer tumor with 2 mm diameter are presented in logarithmic scale, as shown in Figure 4.27. Normalization is done within each breast phantom case, separately. Comparing the calculated signal energies of the conformal bow-tie antenna with the planar bow-tie antenna, signal levels increase when spherical conformal antennas are used. The increment is 4.76 dB, 6.85 dB and 3.10 dB in the

presence of homogeneous fatty breast, quasi-heterogeneous, and homogeneous fibro-glandular breast phantoms, respectively.
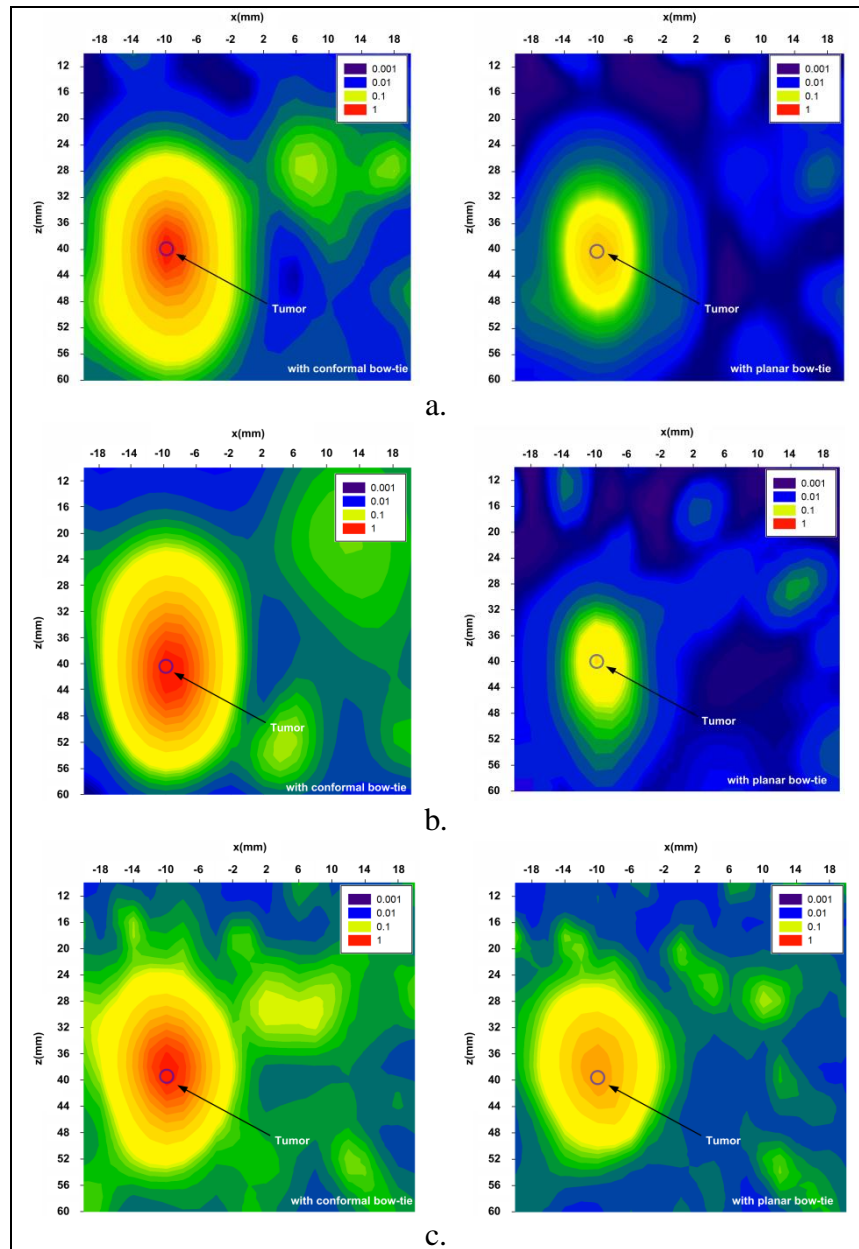
Figure 4.27. Images of breast cancer tumor with 2 mm diameter embedded in a. homogeneous fatty breast, b. quasi-heterogeneous, and c. homogeneous fibro-glandular breast phantoms

More anatomically realistic breast phantom models with dispersive dielectric properties [62, 120] should be included to observe the feasibility of the spherical conformal bow-tie

antennas better for use in the microwave imaging system. However, obtained results are encouraging that an improvement could be also achieved by adding more and smaller conformal antennas to the array encircling the breast, to enhance detection capability of the microwave imaging system more [16].

The proposed bow-tie antenna with spherical curvature would be an attractive candidate element for radar-based breast cancer detection to achieve good polarization matching with spherical waves inside the breast as well as low pulse distortion and low mutual effects between array elements. Time domain behavior of the conformal antenna has indicated better pulse distortion performance through the breast, comparing with the planar bow-tie. The mutual coupling effects of the conformal antenna have been reduced in overall compared to that of the planar antenna, too. Images of the spherical tumor with 2 mm diameter have been successfully formed by using the DAS algorithm. Tumor responses have been increased in between 2.27 dB and 5.70 dB with the use of the spherical conformal antenna.

The phase velocity values of electromagnetic fields inside the breast which are used in the imaging algorithm are obtained separately for the homogeneous fatty breast, quasi-heterogeneous and homogeneous fibro-glandular breast phantoms, by using telemetric information, explained in the latter sub-section.

4.5.5. Compensation of Errors in the Imaging Algorithm Related to Phase Velocities of Electromagnetic Fields inside the Breast

The phase velocity values of electromagnetic fields inside the breast which are used in the imaging algorithm are obtained separately for the homogeneous fatty breast, quasi-heterogeneous and homogeneous fibro-glandular breast phantoms. Telemetric information is obtained in the case of spherical conformal bow-tie antennas, because the results are also same for the planar bow-tie antennas, too.
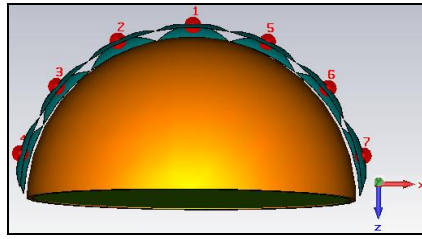
Figure 4.28. Simulation models of spherical conformal bow-tie antennas aligned as encircling the breast phantom

After a lot of trials as it's experienced that; time-delay between the transmitted signal from 4. antenna to 5. antenna (S_{54}) and that from 4. antenna to 7. antenna (S_{74}) is used for determining an appropriate phase velocity value of the electromagnetic field inside the breast, to be used in the imaging algorithm. Since the radar-based microwave imaging algorithm is highly dependent on the phase velocity information, this procedure would be very helpful especially for the heterogeneously dense breast tissues as well as dispersive ones, too.

In the first case, homogeneously fatty breast tissue is used for breast phantom. As time domain pulse is distorted as it propagates through the breast as shown in Figure 4.15 and Figure 4.24, it's also expected for the pulse widths to be widen (dispersed) over the time scale. Therefore, after a lot of trials, correct time delay is measured between S_{54} and S_{74} for the first minimum of the signals, as shown in Figure 4.29.
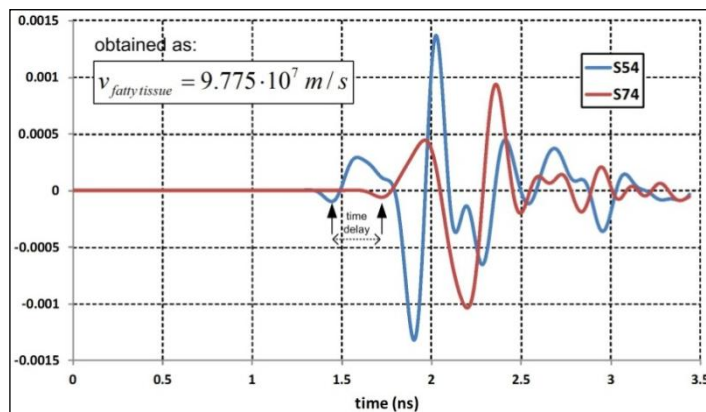
Figure 4.29. Time delay measured between S_{54} and S_{74}, for homogeneously fatty breast tissue

The corresponding obtained phase velocity regarding the time-delay is 9.775×10^7 *m/s*. On the other hand, the theoretical value of the phase velocity of the electromagnetic field inside the homogeneous fatty breast tissue at 4.5 GHz is 9.961×10^7 *m/s*. For pre-testing the appropriateness of the obtained phase velocities in the DAS imaging algorithm is run for only the strongest signals obtained, such as S_{12}, S_{22}, S_{32}, S_{42}, S_{52}, S_{62}, S_{72}. The results of the total signal energy of the processed signals versus row number in the imaging matrix, for the column corresponding to *x*=-10 mm (tumor location), are given in Figure 4.30. The actual tumor location is at *z*=40 mm, which corresponds to the row number of 16, as shown in Figure 4.30.
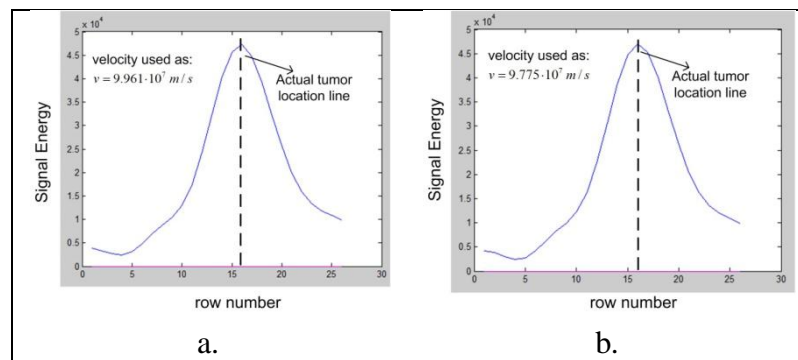
Figure 4.30. Total signal energies of the processed signals versus row number in the imaging matrix, for different phase velocity information in homogeneously fatty breast tissue

In the second case, quasi-heterogeneous breast phantom model is used. The correct time delay is measured between S_{54} and S_{74} for the first minimum of the signals, as shown in Figure 4.31. The corresponding obtained phase velocity regarding the time-delay is 7.991×10^7 *m/s*. On the other hand, the theoretical value of the phase velocities of the electromagnetic field inside the homogeneous fatty breast tissue and homogeneous fibro-glandular tissues at 4.5 GHz are 9.961×10^7 *m/s* and 6.392×10^7 *m/s*, respectively.
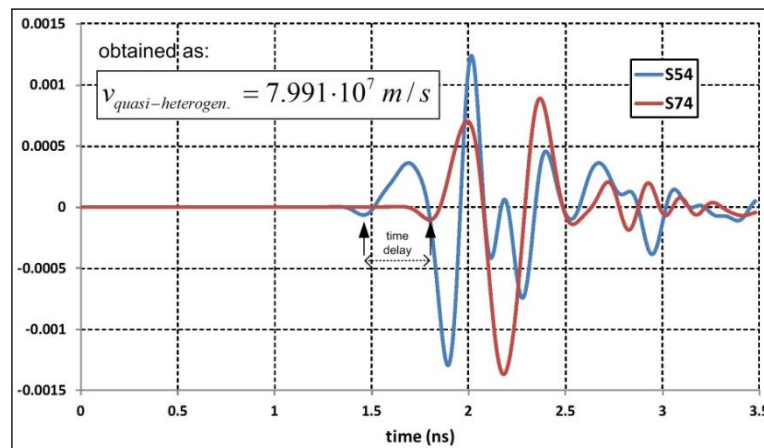
Figure 4.31. Time delay measured between S_{54} and S_{74}, for quasi-heterogeneous breast phantom

The results of the total signal energy of the processed signals versus row number in the imaging matrix are given in Figure 4.32. As it's seen, the tumor location is successfully obtained by 100 per cent when obtained phase velocity information is used by telemetry, as shown in Figure 4.32.b.
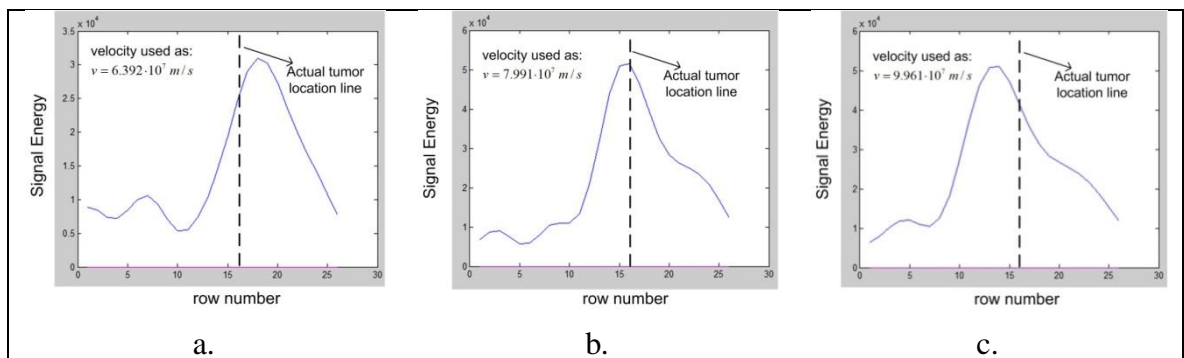
Figure 4.32. Total signal energies of the processed signals versus row number in the imaging matrix, for different phase velocity information in quasi-heterogeneous breast phantom

In the third case, homogeneous fibro-glandular tissue is used for breast phantom. The correct time delay is measured between S_{54} and S_{74} for the first minimum of the signals, as shown in Figure 4.33. The corresponding obtained phase velocity regarding the time-delay is 6.412×10^7 m/s. On the other hand, the theoretical value of the phase velocities of the

electromagnetic field inside the homogeneous fatty breast tissue and homogeneous fibro-glandular tissues at 4.5 GHz are 9.961×10^7 *m/s* and 6.392×10^7 *m/s*, respectively.
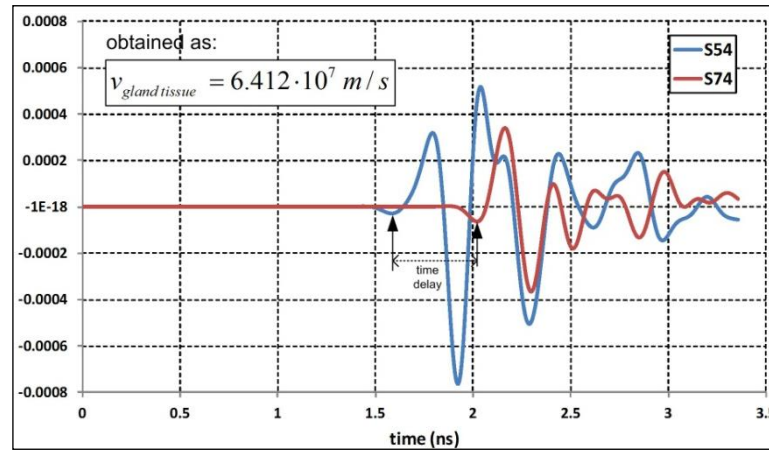
Figure 4.33. Time delay measured between S_{54} and S_{74}, for homogeneous fibro-glandular breast phantom model

The results of the total signal energy of the processed signals versus row number in the imaging matrix are given in Figure 4.34. As it's seen, the tumor location is successfully obtained by 100 per cent, both when obtained phase velocity information by telemetry and the theoretical one is used, as shown in Figure 4.34.b.
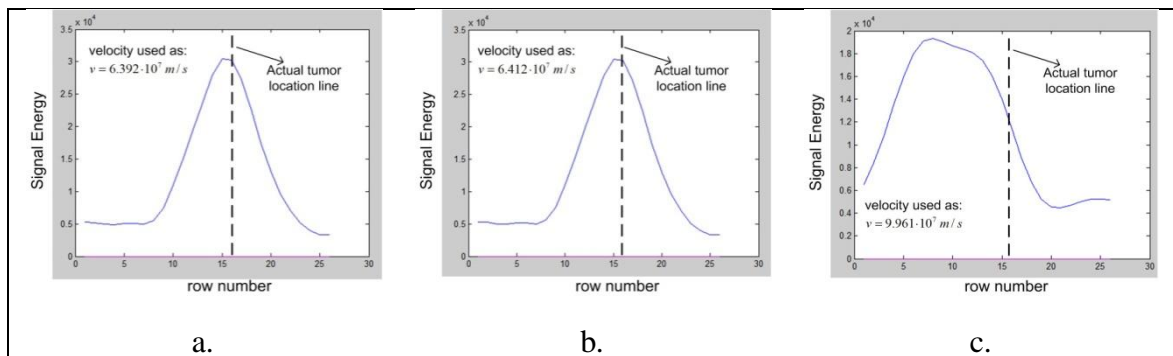
Figure 4.34. Total signal energies of the processed signals versus row number in the imaging matrix, for different phase velocity information in homogeneous fibro-glandular breast phantom model

The phase velocity values obtained by telemetric information had been used in the imaging algorithms before, too.

4.5.6. Comparative Analysis for Different Polarization States of Antennas
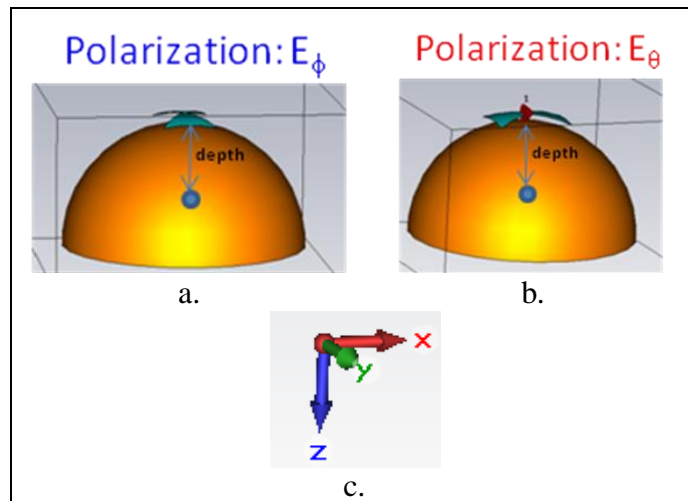
Figure 4.35. a. Case of the polarization state of E_ϕ, b. Case of the polarization state of E_θ, c. Coordinate axes in the CST Microwave Studio©

In this sub-section, a comparative analysis for two different polarization states of the spherical conformal antennas, such as E_ϕ and E_θ, as shown in Figure 4.35. The breast phantom is selected as the homogeneous fatty breast tissue.

The back-scattered co-polarized signals captured in time-domain for the two polarization states are almost close to each other, as it's expected (Figure 4.36). The difference comes from the slightly difference meshing for the same coordinate system, in the simulations program.

The back-scattered cross-polarized signals captured in time-domain for the two polarization states are negligible, as it's expected. These low level signals in Figure 4.37 are found to be masked by higher noise level in the simulation software.
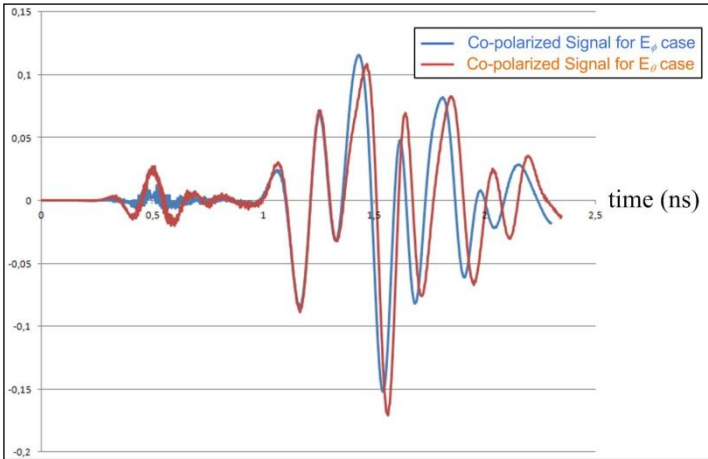
Figure 4.36. Back-scattered co-polarized signals in time domain for the two polarization states
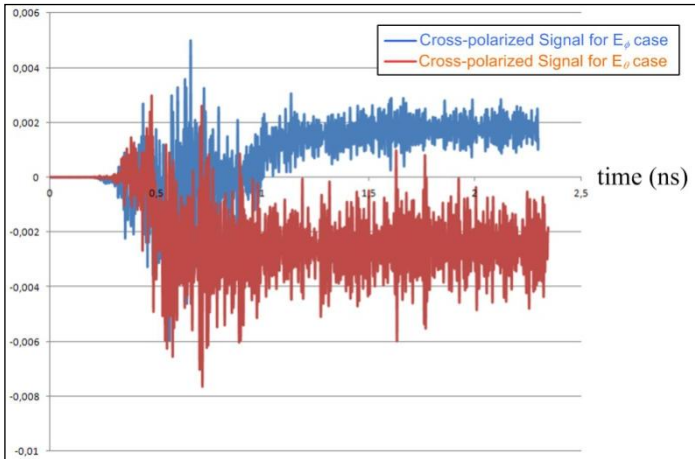
Figure 4.37. Back-scattered cross-polarized signals in time domain for the two polarization states

These findings coincide with the analytical calculations done in Section 2.3, too. Moreover, one can also analyze x-, y-, an z-components of the back-scattered signals for the polarization state of E_ϕ, by locating three E-field probes at (0, 0, -4.715 mm) point which is very close to the antenna port. The results in Figure 4.38 show that the cross-polarized signal (x-component) is very low compared to the others. The z-component of the E-field probe is greater than the co-polarized (y-component) signal by around 12.5 dB in

average. These results would be regarded in the future antenna designs to be able to capture both co-polarized and *z*-polarized waves to increase the tumor response levels.
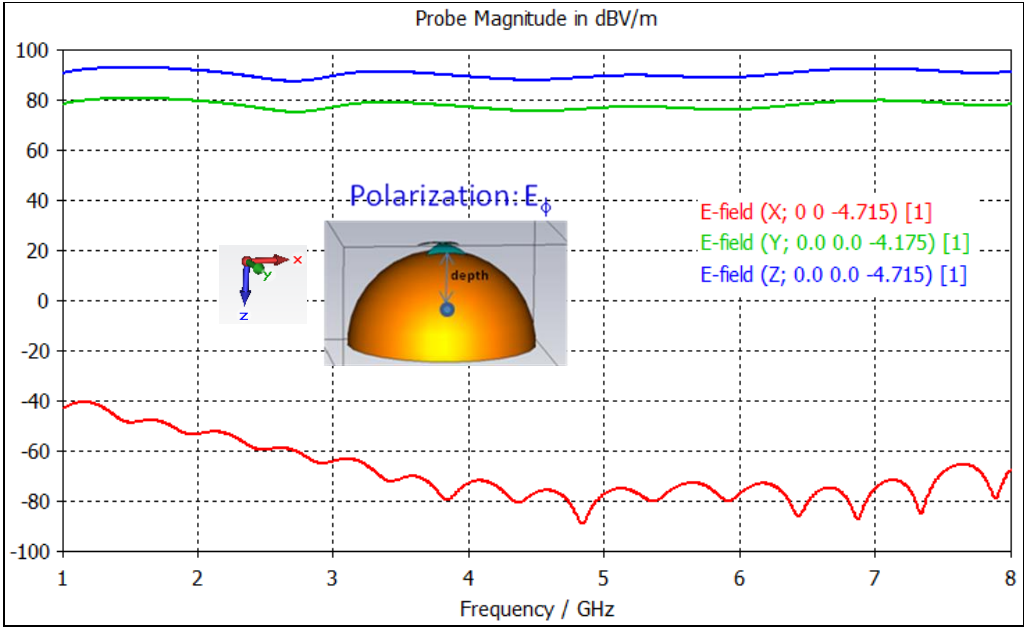
Figure 4.38. *x*-, *y*-, an *z*-components of the back-scattered signals captured by the antenna for the polarization state of E_ϕ

5. EXPERIMENTAL STUDY

5.1. VIVALDI ANTENNA DESIGN AS A SENSOR

In 1979, Gibson proposed a tapered slot antenna also known as a Vivaldi Antenna [123]. In operation, the antenna radiates from the open end of the notch in a direction away from the notch and along the axis of symmetry. The antenna may thus be classed as an end-fire antenna [124].

In theory, tapered slot antenna generally has wide bandwidth, high directivity and is able to produce symmetrical radiation pattern. It has also simple feed structure and easy for fabrication. This type of antenna has been applied to satellite communications, remote sensing, and radio telescope. The advantages of end-fire tapered slot antennas include producing a symmetrical beam in the E- and H-plane or changing beam width by varying the shape, length, dielectric thickness and dielectric constant of the tapered slot antenna [124].

The Vivaldi antenna is one of the classical UWB antennas with many applications. The Vivaldi is a traveling-wave, leaky, end-fire antenna. Theoretically, the Vivaldi antenna has an unlimited range of operating frequencies, with constant beam width over the entire bandwidth. In UWB communications, in addition to achieving a good return loss and radiation efficiency, the UWB antenna should be non-dispersive or dispersive in an acceptable range [125].

Two Vivaldi antennas are considered for the experimental imaging study. We can name these antennas as "Large Vivaldi" and "Small Vivaldi", as shown in Figure 5.1 and Figure 5.2. On both antennas, the tapered microstrip line is applied as the antenna feeder and a 0.5 mm thick FR4 (ε_r=4.4, tanδ=0.025) material is used for both of them as a substrate. The upper and lower layers are copper layer which have a thickness of 0.035 mm. The length and width of Large Vivaldi is 100 mm × 35 mm, and that of Small Vivaldi is 27.34 mm × 14 mm. Design criteria of these antennas are given in Appendix C.
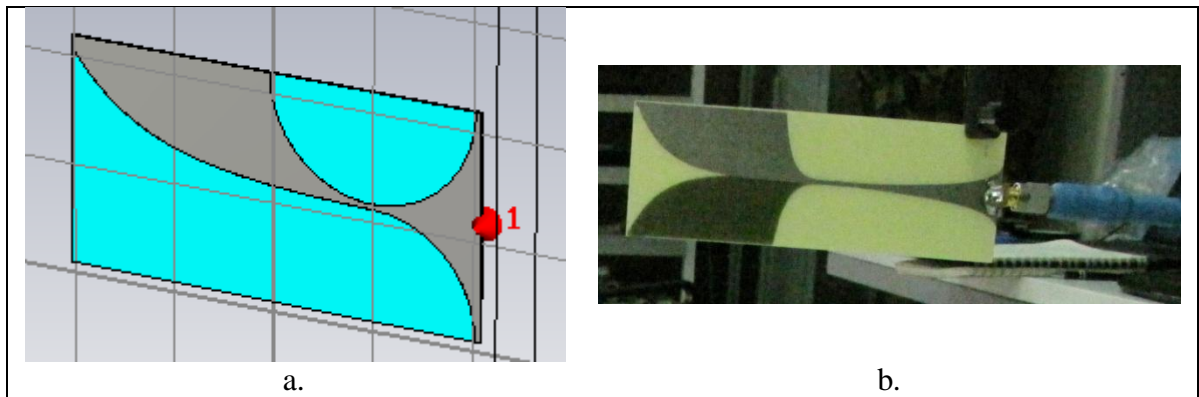
Figure 5.1. a. Simulated and b. fabricated Large Vivaldi antenna (100 mm × 35 mm)
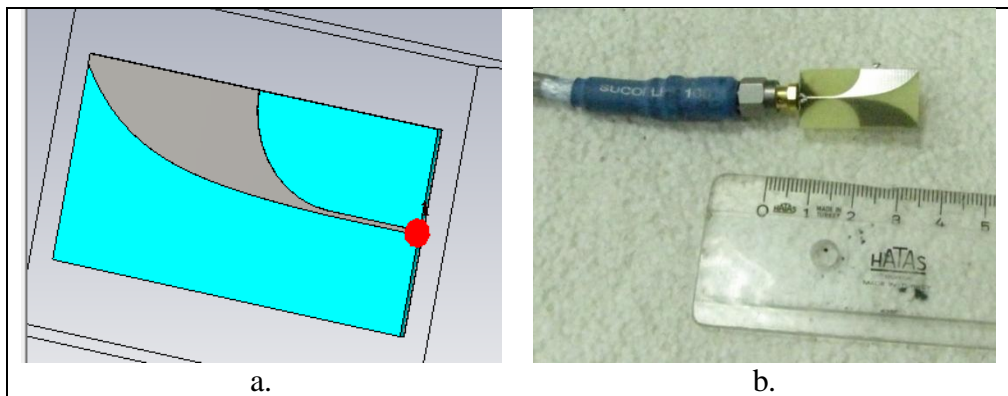
Figure 5.2. a. Simulated and b. fabricated Small Vivaldi antenna (27.34 mm × 14 mm)

The upper and lower layers can be shown in Figure 5.1.a and Figure 5.2.a, respectively. Simulation and experimental results of return loss of the Large Vivaldi antenna operating in air are shown in Figure 5.3. It clearly indicates that the-10 dB return loss bandwidth is very wide spanning from around 5 GHz over 10 GHz. The Large Vivaldi antenna will be operated between 5 and 10 GHz in the experimental measurements. These Vivaldi antennas are designed and fabricated by TÜBİTAK-BİLGEM-UEKAE.

In a microwave imaging system operating with the breast, since the skin reflections back to the antenna can adversely affect imaging results, better penetration of electromagnetic waves into the breast tissue would be determined by operating the antenna in a coupling medium whose dielectric properties are close to the breast tissue. Antenna size would also be selected to be smaller since the wavelength in the coupling medium will be smaller than air. For this purpose, Small Vivaldi antenna has been designed as smaller than Large

Vivaldi, to be able to operate in a coupling medium with ε_r=9 (Table 2.8). Therefore, this Small Vivaldi antenna has been designed in order to operate in the coupling medium.
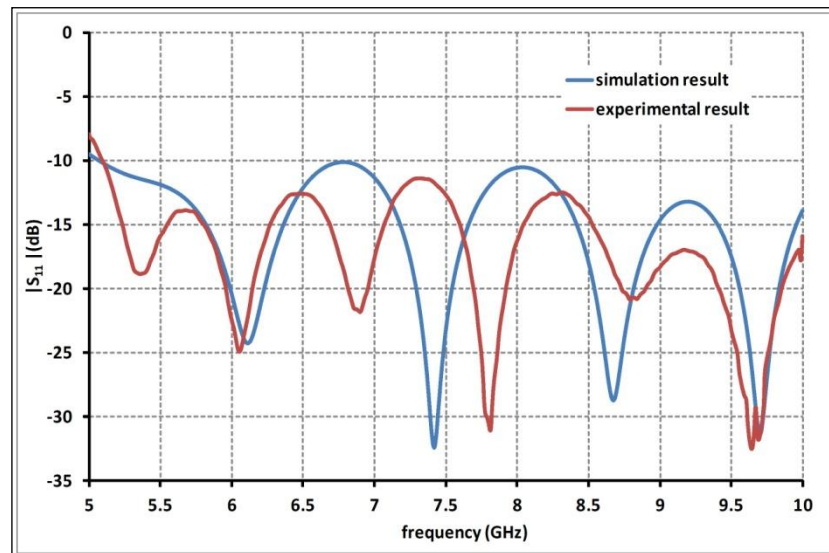
Figure 5.3. Simulation and experimental results of return loss of the Large Vivaldi antenna operating in air
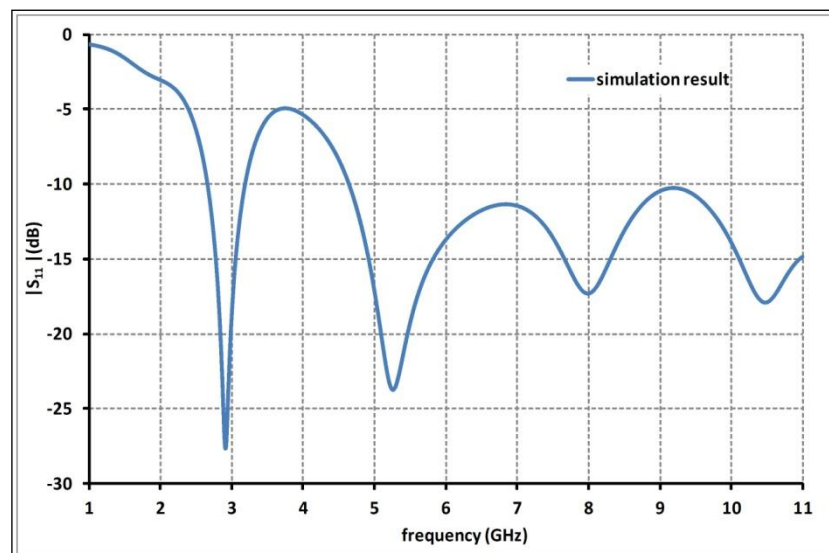
Figure 5.4. Simulation result of return loss of the Small Vivaldi antenna operating in coupling medium

Figure 5.4 indicates that the -10 dB return loss bandwidth is very wide spanning from around 4.5 GHz over 11 GHz. In the preliminary simulation study for microwave imaging, Small Vivaldi antenna is operated between 4.5 and 10.5 GHz. Since an appropriate coupling medium with ε_r=9 isn't found, the experimental test of the antenna is the coupling medium is not available, yet.

5.2. PRELIMINARY SIMULATION STUDY FOR MICROWAVE IMAGING
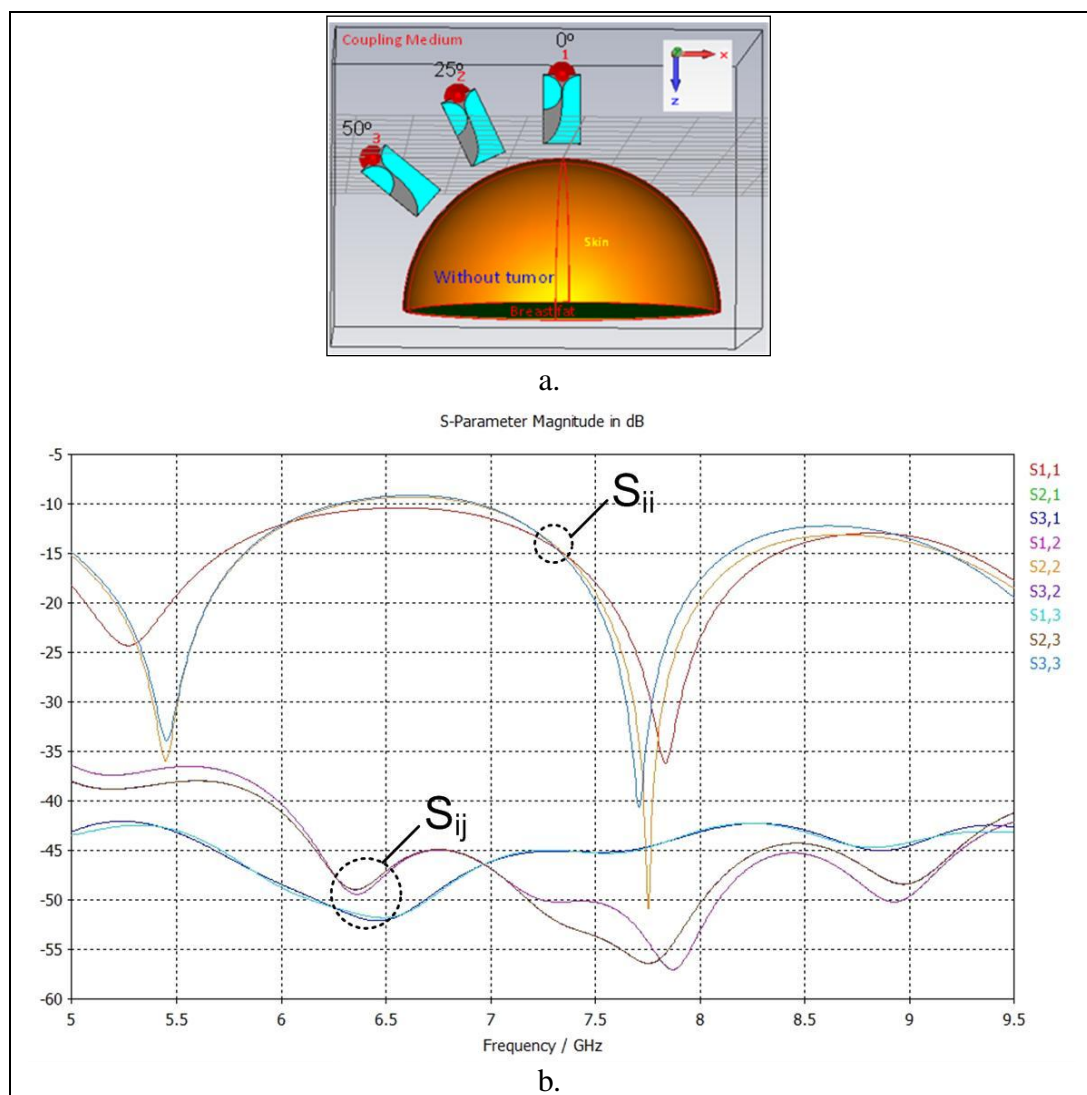
Figure 5.5. a. Simulation model of Small Vivaldi antenna array in front of the breast phantom, b. frequency response of the magnitude of (S_{ii} and S_{ij}, i≠j) for three antennas in the half-spherical antenna array in front of the breast phantom for 5-9.5 GHz

In the first case, three UWB Small Vivaldi antennas are located optimally 5.82 mm above the breast phantom with homogeneous fatty breast tissue that is modeled on CST Microwave Studio®, to calculate the performance of the antennas (Figure 5.5.a). A sine-modulated Gaussian pulse excitation signal with the 4.5–10.5 GHz frequency range is used; that guarantees balance between reasonable contradictory needs of better spatial resolution, better penetration depth, less attenuation of electromagnetic waves through the breast and smaller dimensions of a multi-function active imaging system (Figure 5.6). The selected frequency range is expected to provide reasonable tumor detection capabilities, too. The antenna-skin distance is optimally selected as 5.82 mm.
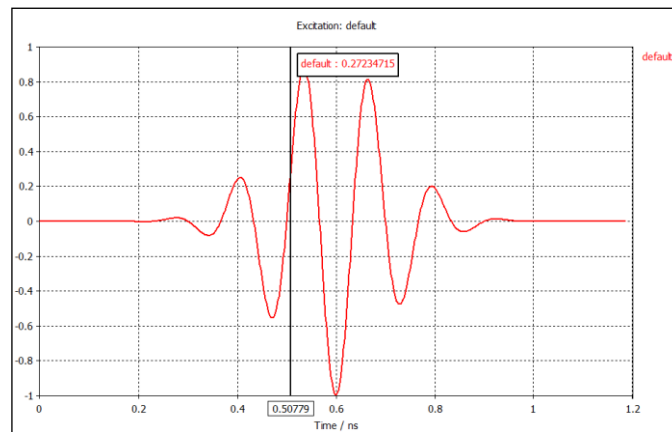
Figure 5.6. Sine-modulated Gaussian pulse excitation signal with the 4.5–10.5 GHz frequency range

All of nine time-domain and frequency-domain signals (S_{ii} and S_{ij}, $i{\neq}j$) coming from three antennas are obtained from the simulation model with and without 2 mm diameter tumor inside breast phantom model by feeding each antenna sequentially. The frequency response of the magnitude of (S_{ii} and S_{ij}, $i{\neq}j$) for the antennas operating in the half-spherical antenna array in front of the breast phantom without tumor are shown in (Figure 5.5.b). Figure 5.5.b indicates that the mutual coupling effects between antenna elements (S_{ij}, $i{\neq}j$) are very low, under -35 dB in the whole frequency range.

Recorded time-domain data are processed on DAS algorithm, and then images of the computed backscattered signal energies for each pixel are created as a function of position, as shown in Figure 5.7.
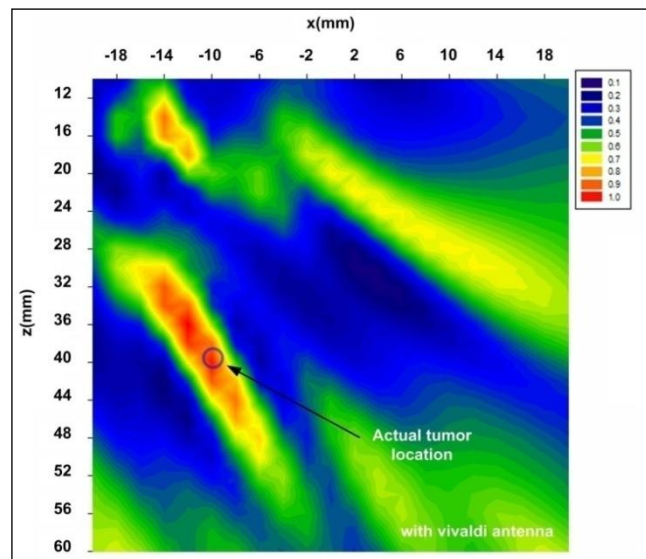
Figure 5.7. Image of breast cancer tumor with 2 mm diameter at 40 mm depth embedded in
the homogeneous fatty breast phantom

The faulty location of the detected tumor has been observed by around 4 mm. As the
signals are analyzed, S_{13} or S_{31} signals show anomaly; then if one avoids the use of them in
the imaging algorithm, the tumor is successfully detected in its actual location, as shown in
Figure 5.8.
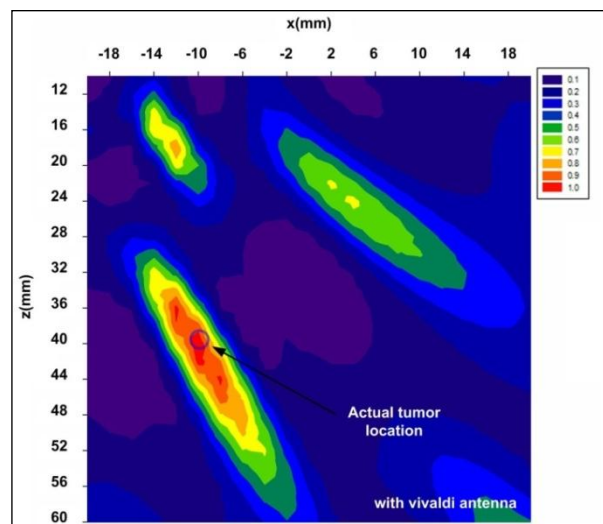
Figure 5.8. Image of breast cancer tumor with 2 mm diameter at 40 mm depth embedded in
the homogeneous fatty breast phantom, without the use of anomaly signals

If one changes the location of the tumor at 30 mm depth for another case study, the tumor has been also succesffuly detected, as shown in Figure 5.9. Tumor response levels has been obtained between -90 and -110 dB, which is an available region for practical measurements.
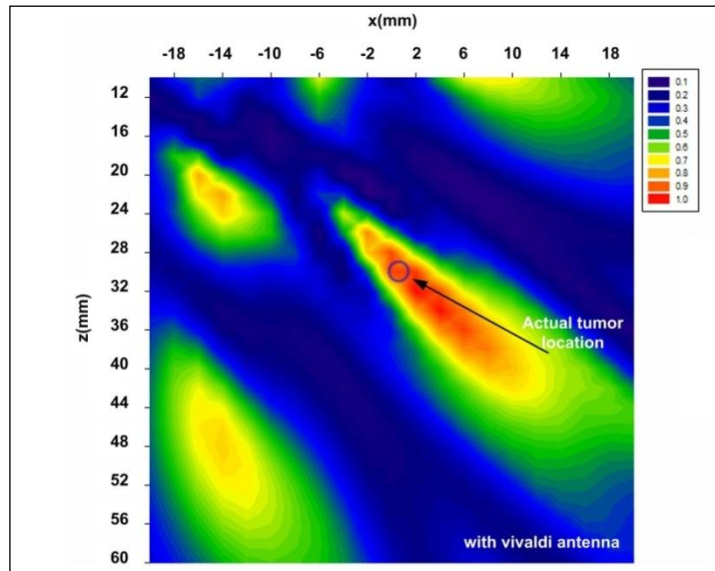
Figure 5.9. Image of breast cancer tumor with 2 mm diameter at 30 mm depth embedded in the homogeneous fatty breast phantom

If the antennas encircling the breast increase, the faulty tumor location error in the image would decrease, opposite the possible anomaly signals. Therefore, as a different case, seven UWB Small Vivaldi antennas are located optimally 5.82 mm above the breast phantom with homogeneous fatty breast tissue that is also modeled on CST Microwave Studio® (Figure 5.10.a). The same sine-modulated Gaussian pulse excitation signal with the 4.5–10.5 GHz frequency range is used.

All of 49 time-domain and frequency-domain signals (S_{ii} and S_{ij}, i≠j) coming from three antennas are obtained from the simulation model with and without 2 mm diameter tumor at 40 mm depth inside breast phantom model by feeding each antenna sequentially. The frequency responses of the magnitude of (S_{ii} and S_{ij}, i≠j) for the antennas operating in the half-spherical antenna array in front of the breast phantom without tumor are shown in

(Figure 5.10.b). Figure 5.10.b indicates that the mutual coupling effects between antenna elements (S_{ij}, i≠j) are very low, under -30 dB in the whole frequency range.
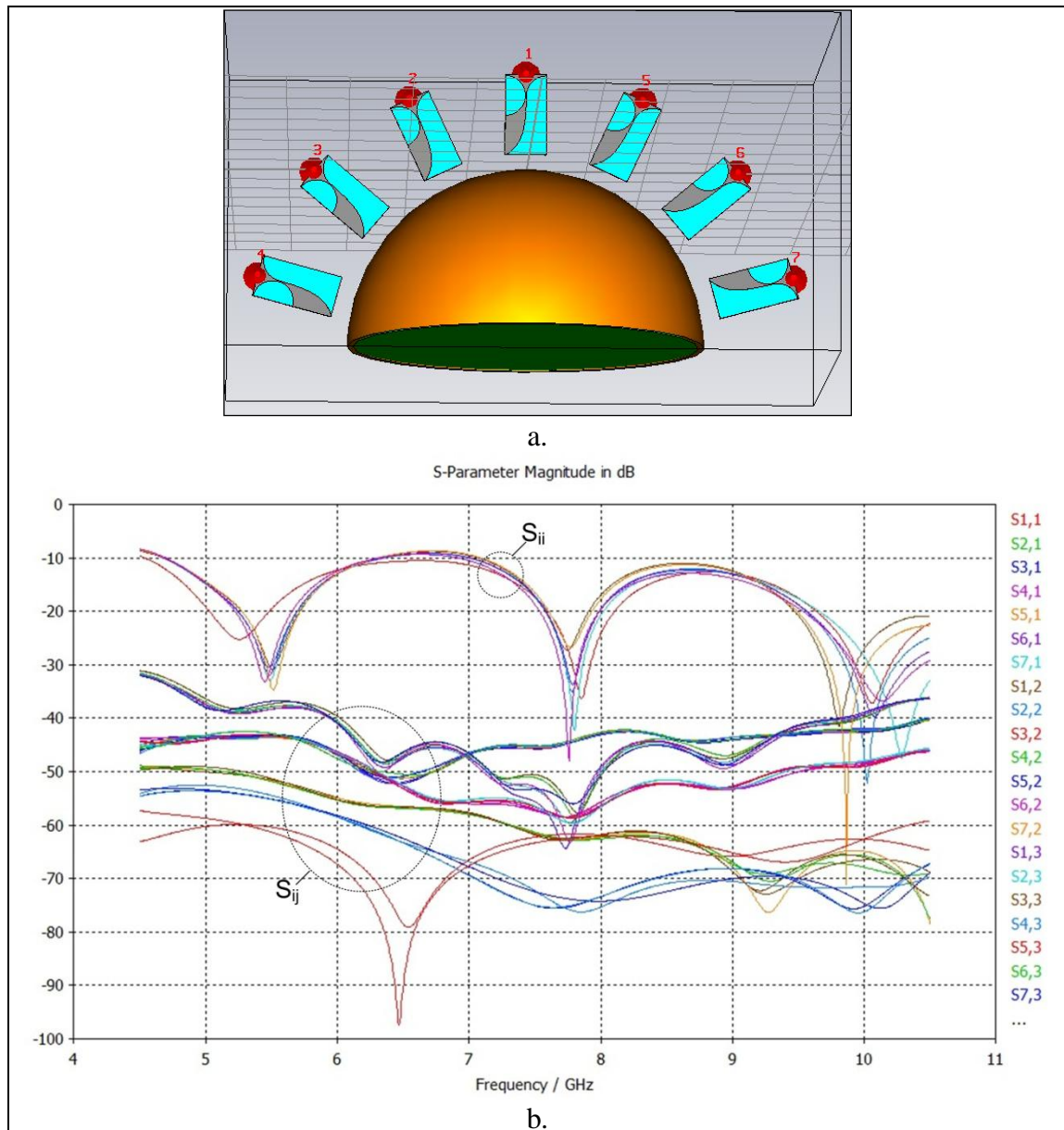
Figure 5.10. a. Simulation model of Small Vivaldi antenna array in front of the breast phantom, b. frequency response of the magnitude of (S_{ii} and S_{ij}, i≠j) for seven antennas in the half-spherical antenna array in front of the breast phantom without tumor

Recorded time-domain data are processed on DAS algorithm, and then images of the computed backscattered signal energies for each pixel are created as a function of position, as shown in Figure 5.11.
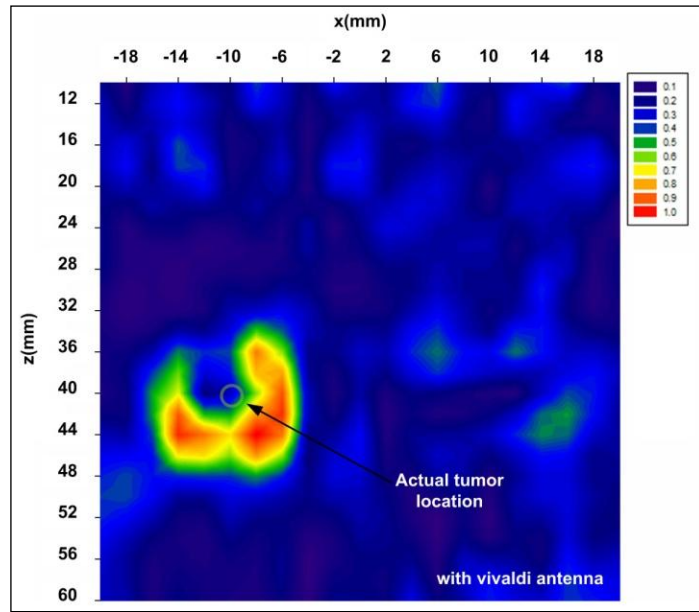
Figure 5.11. Image of breast cancer tumor with 2 mm diameter at 40 mm depth embedded in the homogeneous fatty breast phantom

The tumor has been detected by a small faulty location, however it situation is highly related to the anomaly signals as explained above. Increasing the number of antennas more would decrease the faulty location problems, too.

5.3. EXPERIMENTAL MEASUREMENT SET-UP

In the experimental measurement setup as shown in Figure 5.12.a, the Large Vivaldi antenna is located in front of a homogeneous breast phantom model, which was determined in TUBITAK-MAM [126]. The vivaldi antenna is connected to a performance network analyzer (Agilent PNA N5230A, 10 MHz-20 GHz) to transmit and receive microwave signals. The breast phantom is manually rotated around itself by 20° degrees at each measurement, using a wooden rod (Figure 5.12.b).

There are two breast phantoms used in the experiments, as shown in Figure 5.13. The breast phantoms are illuminated by the both Large and Small Vivaldi antennas, and the backscattered signals (S_{11}) in the frequency-domain are recorded in the frequency range of 5-10 GHz. Electromagnetic absorbing materials within a box are located under the

experimental setup, as well as the the back of the system to reduce ambient reflections (Figure 5.12.a).

a.

b.
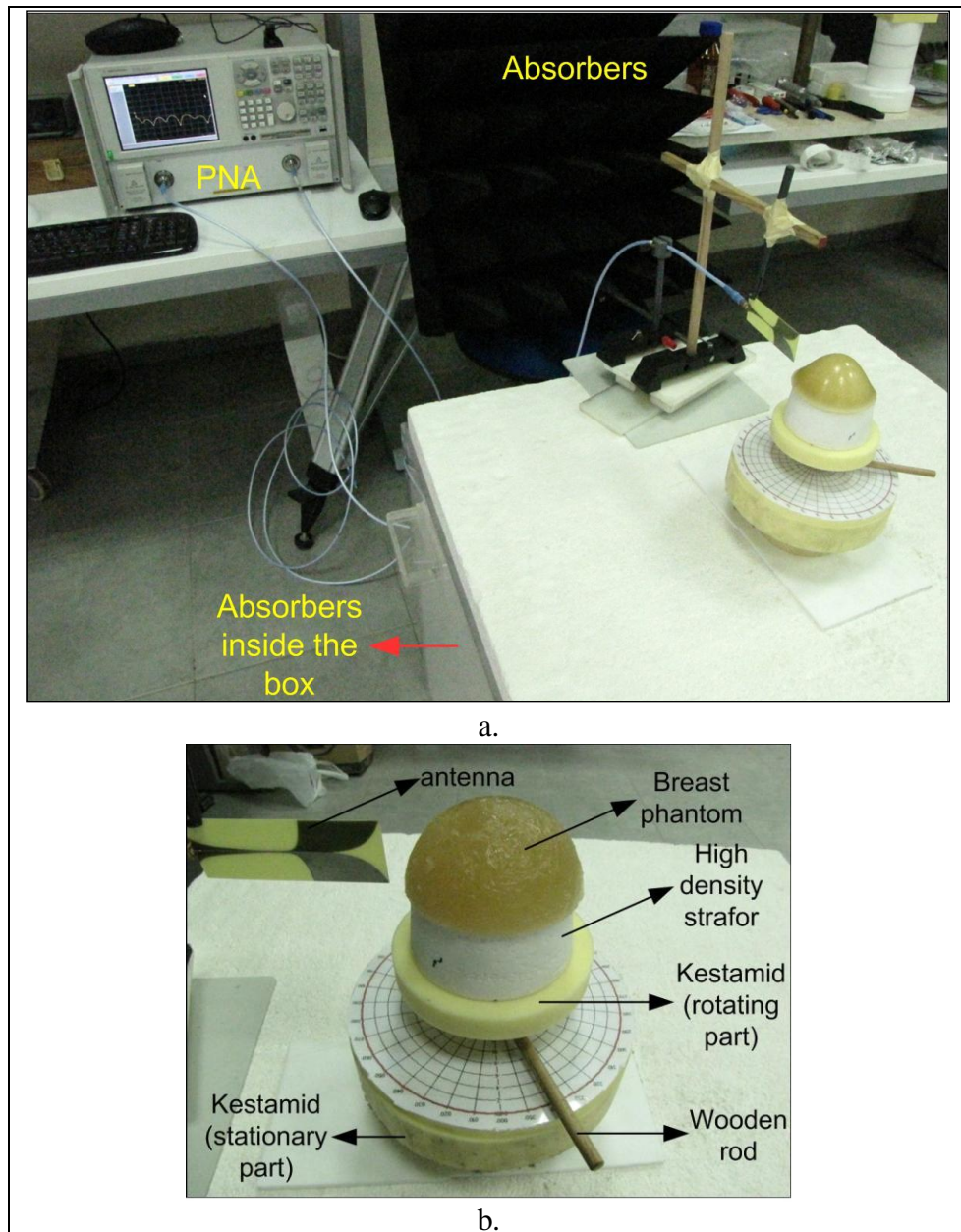
Figure 5.12. Experimental setup of the microwave imaging system

The breast phantom is sequentially rotated manually by 20° degrees and the backscattered signals (S_{11}) are recorded in the frequency range of 5–10 GHz, at each step. Totally measured 18 frequency-domain datas at each angle (separated by 20°) are recorded at 1001 frequency points, and its time-domain equivalent is obtained by using inverse FFT. Images

of the computed signal energies are created as a function of position by using DAS algorithm.
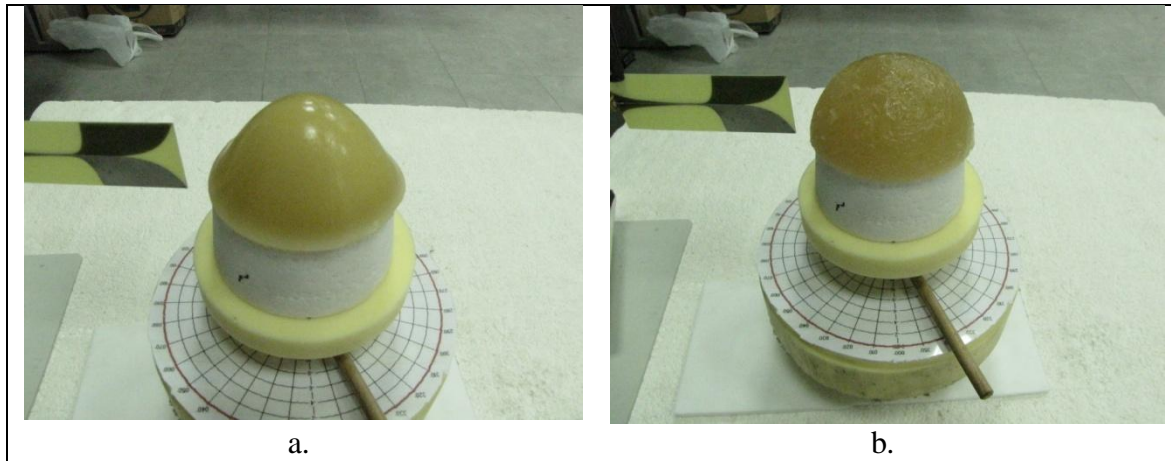
Figure 5.13. Breast phantom models used in the experimental study, a. Phantom 1, b. Phantom 2

Inverse FFT is calculated as follows. First of all, the complex conjugate of S_{ii} data is taken, and then those values are located in the symmetrical negative-real axis, as expressed in Equation (5.1). Then, an inverse FFT operation is done through MATLAB, with the aid of "ifftshift" and "ifft" functions, as well as zero padding.

$$S_{ii}(-f) = S_{ii}^{*}(f) \tag{5.1}$$

5.4. MEASUREMENTS AND IMAGING RESULTS

Before obtaining the imaging results, time-delay test has been done by using a metal plate for both Large and Small Vivaldi antennas operating in air, as shown in Figure 5.14. "d" values correspond to the distance between the antenna and metal plate. Time-domain "plate response" signals S_{11}^{T} are calculated as extracting S_{11} time-domain signal with plate from the one without plate, as explained in Equation (4.1).
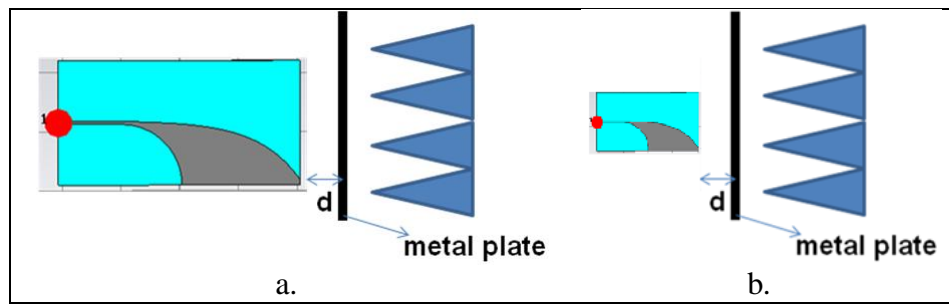
Figure 5.14. Schematic illustration of measurement set-ups for time-delay test by using a metal plate for a. Large Vivaldi, b. Small Vivaldi antenna
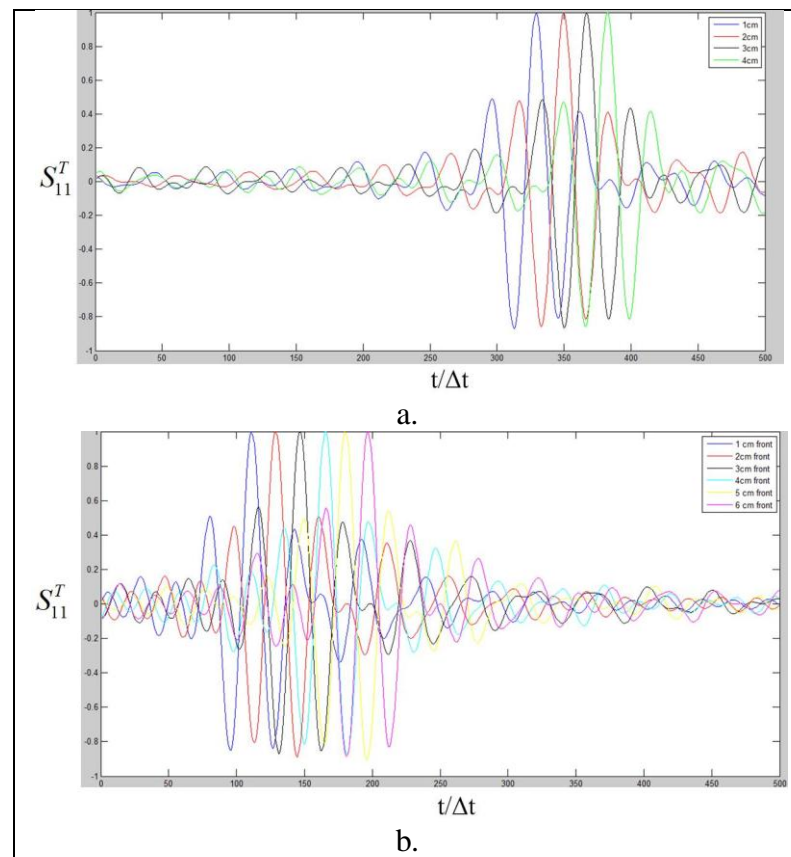
Figure 5.15. Time-domain "plate response" signals for different d values, for a. Large Vivaldi, b. Small Vivaldi antennas (in air)

Time-domain "plate response" signals for different d values for Large and Small Vivaldi antennas are shown in Figure 5.15. The time step is taken as $\Delta t = 4 \times 10^{-12}$ sec. Successful time-delays are obtained for each metal plate movement, after analyzing the results in Figure 5.15.

Moreover, another time-delay test has been done by using a tumor mimicking PEC object with 8 mm diameter for Small Vivaldi antenna operating in air, as shown in Figure 5.16.
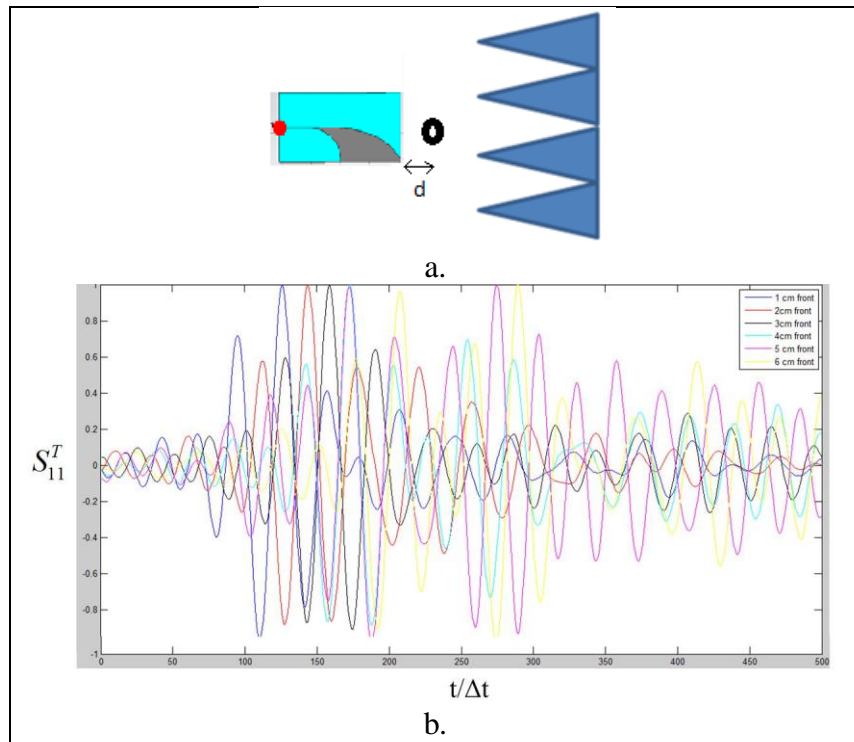
Figure 5.16. Time-domain "tumor response" signals for different d values, for Small Vivaldi antenna (in air)

Time-domain "tumor response" signals for different d values for Small Vivaldi antenna are shown in Figure 5.16. The time step is taken as $\Delta t = 4 \times 10^{-12}$ sec. However, some anomaly time-delays have been observed for distances greater than 4 cm, after analyzing the results in Figure 5.16.

It should be noted that since it is difficult to test the Small Vivaldi antenna in the coupling medium, the Small Vivaldi antenna will be operated in air for the experimental measurements. The difficulty comes from risk of possible short-circuits of the antenna inside the coupling liquid, risk of possible leakage of the coupling liquid into the port cable, and hardness of determining a coupling medium (liquid) whose electrical properties are very close to the fatty breast tissue. Although it's operated in air, the movement of the metal plate has been successfully observed via delayed "plate response" signals in Figure 5.15.

The phase velocity values of electromagnetic fields inside the breast phantom models which are used in the imaging algorithm are obtained separately for Phantom 1 and Phantom 2. Time-delay between the transmitted signal from 1. antenna to 2. antenna (S_{21}) has been observed for determining an appropriate phase velocity value of the electromagnetic field inside the breast phantoms, to be used in the imaging algorithm, as shown in Figure 5.17.

a. b.
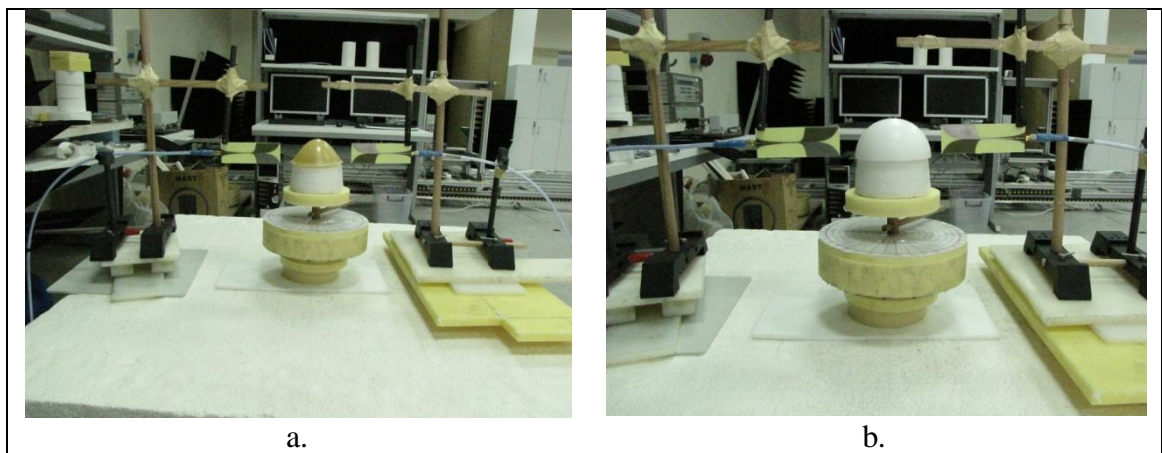
Figure 5.17. Experimental measurement set-up for determining an appropriate phase velocity value of the electromagnetic field inside the breast phantoms

A teflon phantom, in Figure 5.17.b, is also used in the experiments with the knowledge of the value of dielectric constant as 2.2. Comparing the S_{21} time-domain signals for the cases of air, teflon phantom, Phantom 1 and Phantom 2 located in between the antennas (Figure 5.18), the phase velocity values of the electromagnetic fields inside Phantom 1 and Phantom 2 obtained as $v=220.1\times10^6$ *m/s* and $v=202.3\times10^6$ *m/s*, respectively, as in Section 4.5.5. The time step is taken as $\Delta t=4\times10^{-12}$ sec.
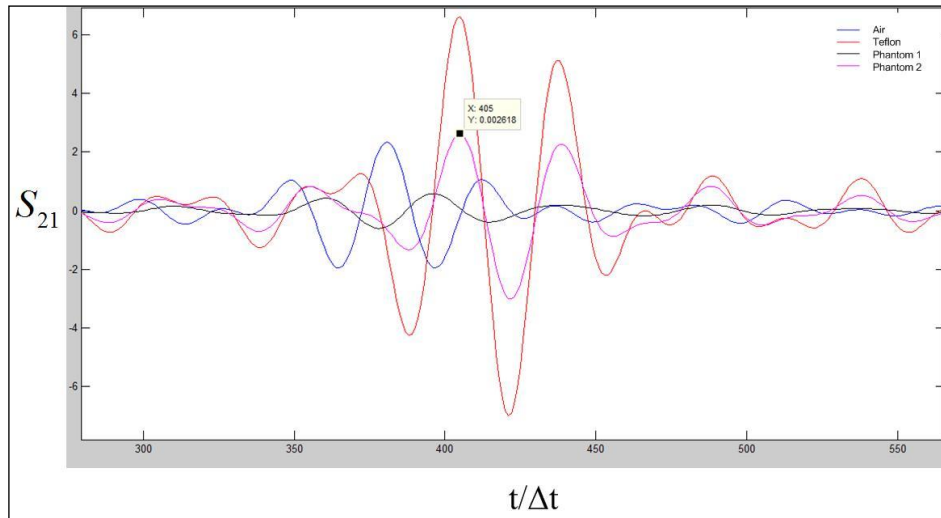
Figure 5.18. Comparisons of the S_{21} time-domain signals for the cases of air, teflon phantom, Phantom 1 and Phantom 2, located in between the antennas

After a lot of trials, the time-step is decreased to $\Delta t = 4 \times 10^{-13}$ sec for better imaging results. There are two scenarios to detect 10 mm diameter spherical PEC object inside Phantom 2 with Small Vivaldi, and there are also two more scenarios to detect 8 mm diameter spherical PEC object inside Phantom 1 with Large Vivaldi.

The imaging results for 1. and 2. scenarios with Small Vivaldi are given in Figure 5.19 and Figure 5.20. As the time-delays of each measured data at different angles (separated by 20°) are not far away from each other, at the center point ($x=0$ mm, $y=0$ mm) and near around that point, the computed signal energy of the time-shifted total tumor response becomes maximum at this location, resulting to mask the visibility of the tumor in the images of Figure 5.19.a and Figure 5.20.a. However, if one disregards and compensates the high energy regions centered at the center point ($x=0$ mm, $y=0$ mm), the resulting compensated images give approximately the correct location of the tumor, as shown in Figure 5.19.b and in Figure 5.20.b.
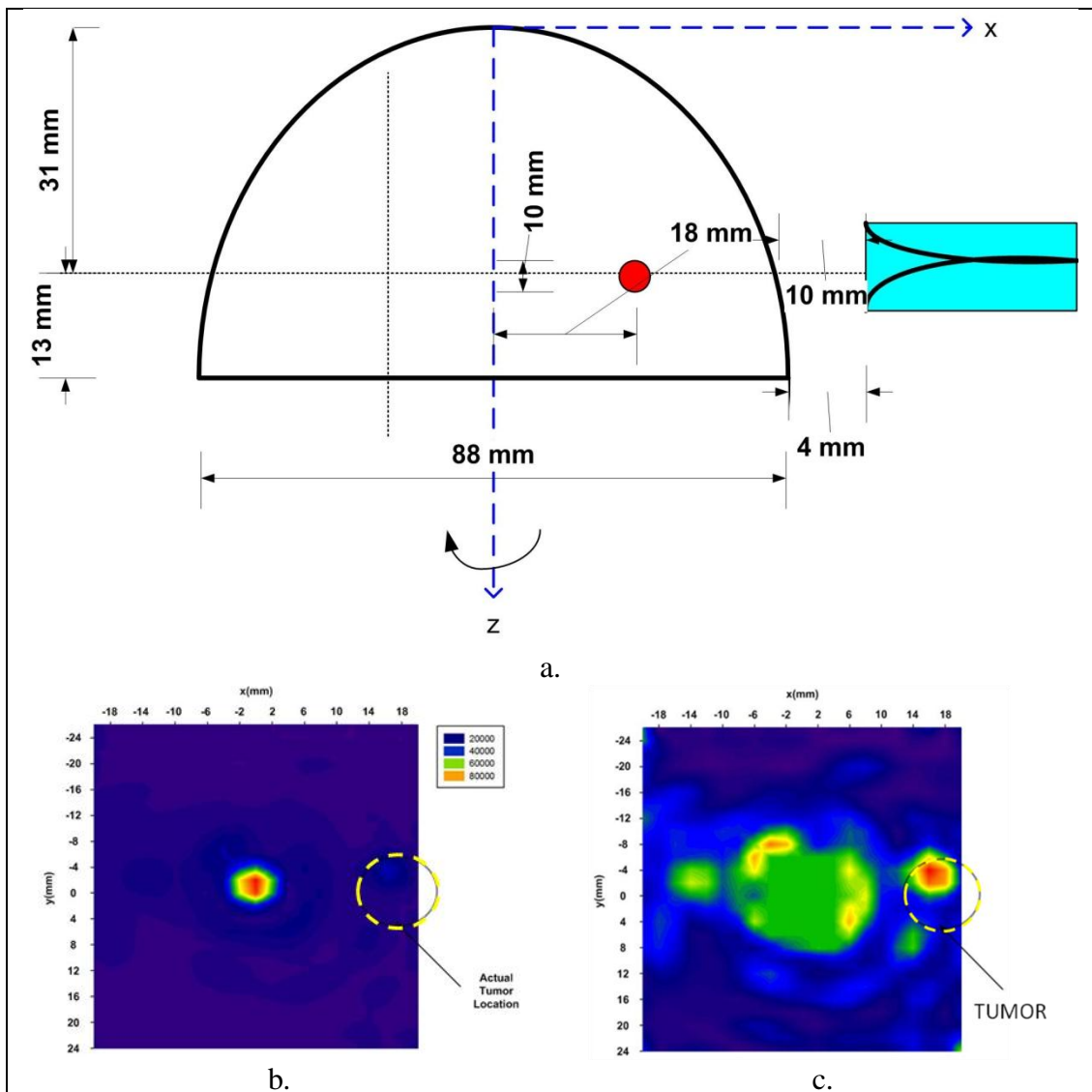
Figure 5.19. a. Schematic illustration of 1. scenario for the detection of 10 mm diameter spherical PEC object inside Phantom 2, with Small Vivaldi, b. Imaging result in *x-y* plane, at *z*= 31 mm, c. Compensated imaging result in *x-y* plane, at *z*= 31 mm
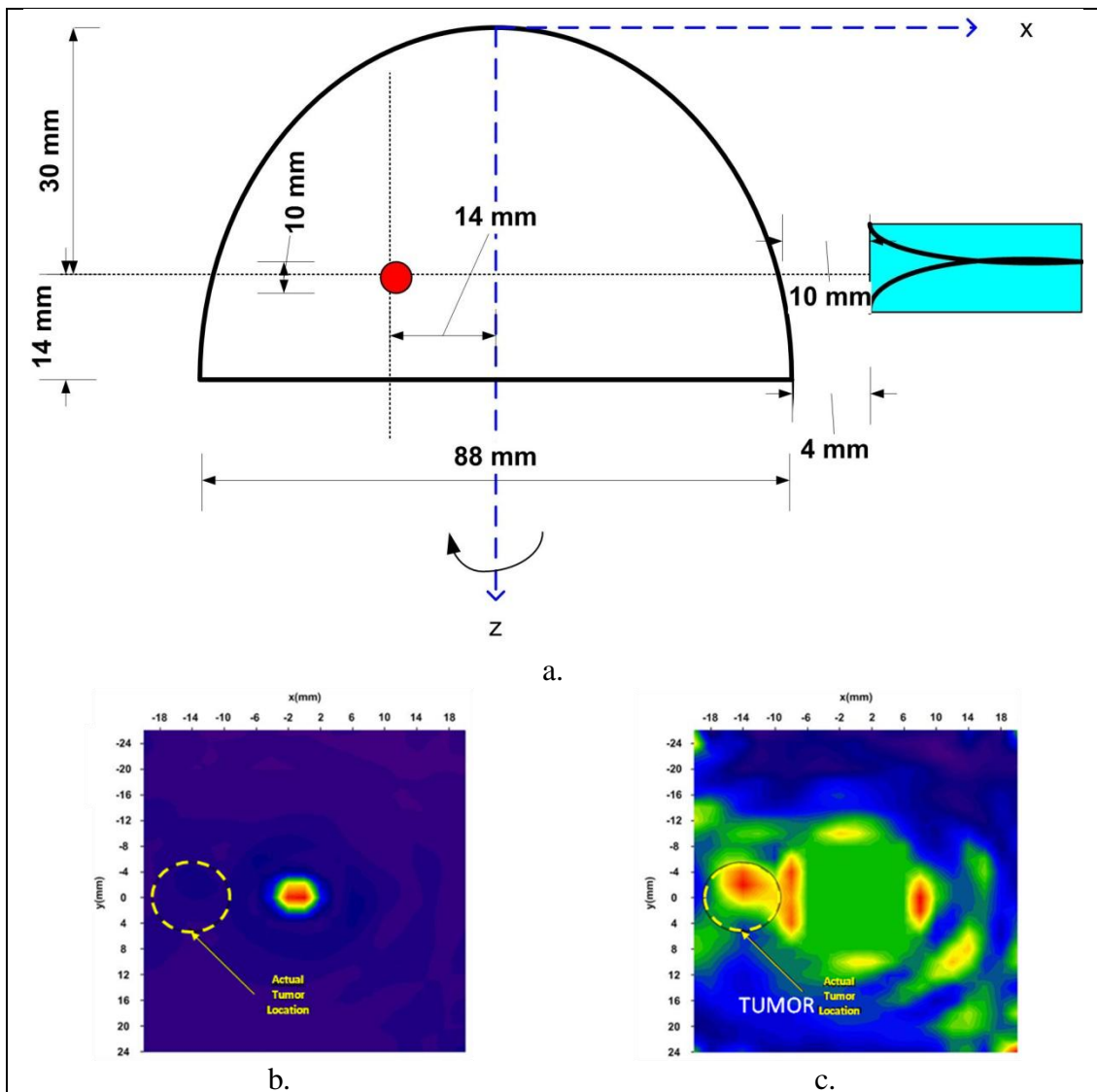
Figure 5.20. a. Schematic illustration of 2. scenario for the detection of 10 mm diameter spherical PEC object inside Phantom 2, with Small Vivaldi, b. Imaging results in *x-y* plane, at *z*= 30 mm, c. Compensated imaging result in *x-y* plane, at *z*= 30 mm

The imaging results for 3. and 4. scenarios with Large Vivaldi are given in Figure 5.21 and Figure 5.22. In these cases, it wasn't found to make a compensation for the center point (*x*=0 mm, *y*=0 mm) and near around that point, in the imaging results. The resulting image of 3. scenario gives approximately the correct location of the tumor, as shown in Figure 5.21.b, but for the case of 4. scenario the tumor seems to be around 10 mm far from its actual location (Figure 5.22.b). This error is probably related to possible anomaly delays of the signals captured by the antenna as explained in Section 5.2 and as shown in Figure 5.16. Those anomaly time-delays had been also observed in the simulations, in Section 5.2.

There might be also little shifts while rotating of the breast phantoms manually, as an experimental error.
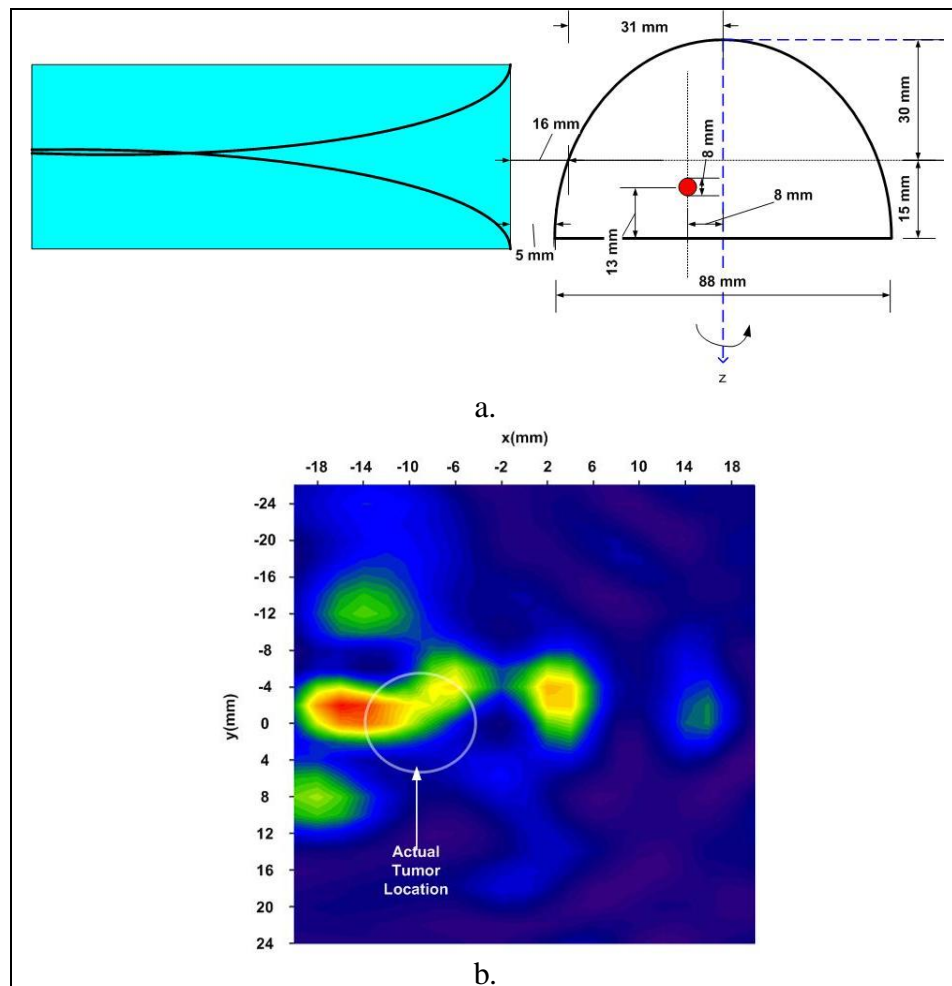
Figure 5.21. a. Schematic illustration of 3. scenario for the detection of 8 mm diameter spherical PEC object inside Phantom 1 with Large Vivaldi, b. Imaging results in *x-y* plane, at *z*= 32 mm
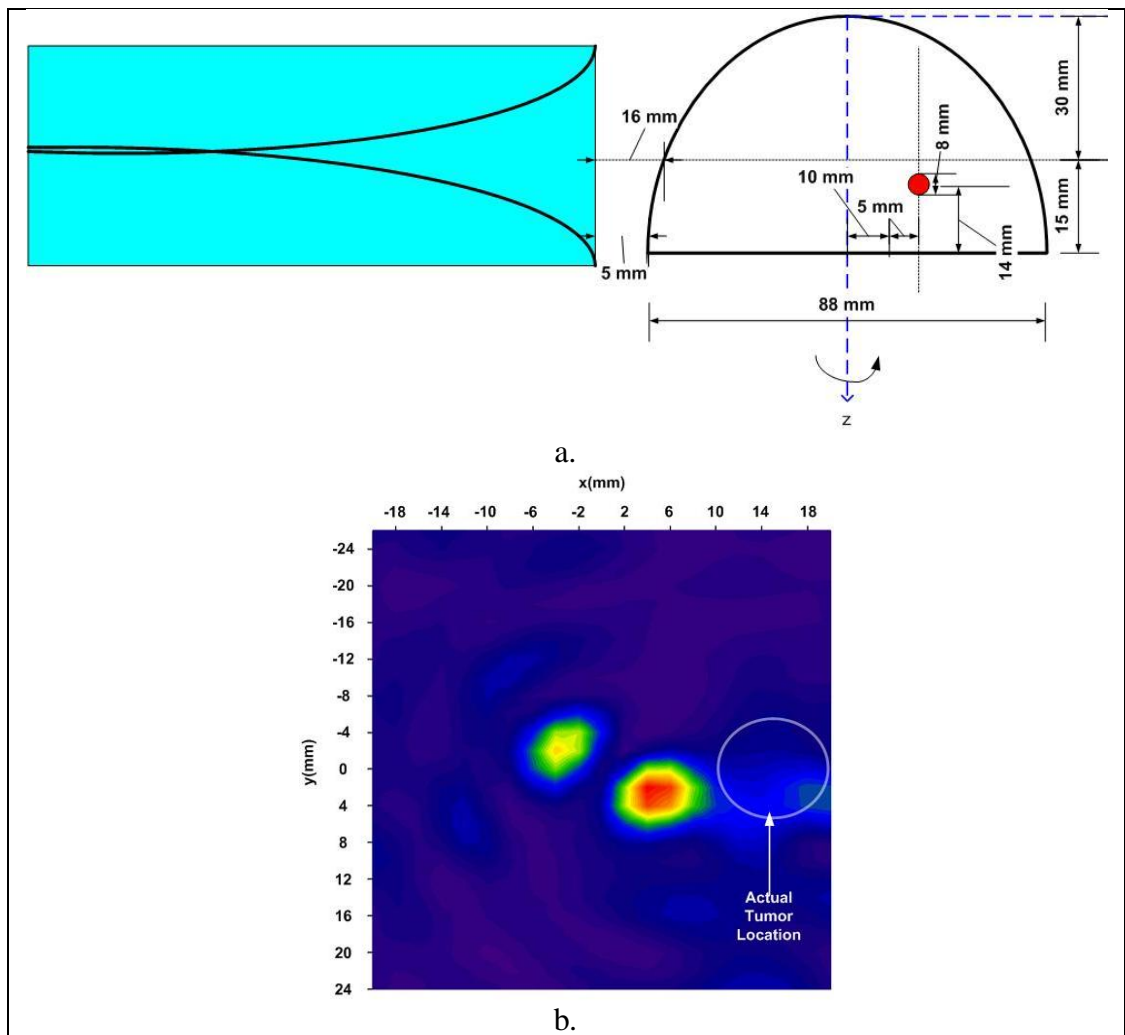
Figure 5.22. a. Schematic illustration of 4. scenario for the detection of 8 mm diameter spherical PEC object inside Phantom 1 with Large Vivaldi, b. Imaging results in *x-y* plane, at *z*= 31 mm

6. CONCLUSIONS AND REMAINING WORK

This dissertation mainly presents herein spherical conformal bow-tie antennas to improve tumor detection capability of the microwave imaging system. Conventional planar UWB bow-tie antennas are curved onto a hemi-sphere surface to investigate its effects on enhancement of tumor responses and signal energies, as well as that of mutual coupling levels between array elements and pulse distortion performance. This UWB spherical conformal bow-tie antenna array surrounding the breast has been designed and tested on the full-wave electromagnetic simulator for this new microwave radar-based imaging system. The proposed bow-tie antenna with spherical curvature would be an attractive candidate element for radar-based breast cancer detection to achieve good polarization matching with spherical waves inside the breast, as well as low pulse distortion and low mutual effects between array elements. Time domain behavior of the conformal antenna has indicated better pulse distortion performance through the breast, comparing with the planar bow-tie. The mutual coupling effects of the conformal antenna have been reduced in overall compared to that of the planar antenna, too. Three different breast phantom models with homogeneous fatty breast tissue, quasi-heterogeneous mix of fibro-glandular and fatty breast tissues, and homogeneous fibro-glandular tissue have been used representing "mostly fatty", "heterogeneously dense" and "very dense" quasi-realistic phantom models, respectively. Images of the spherical tumor with 2 mm diameter have been successfully formed by using the DAS algorithm. The use of the spherical conformal antenna presents an excellent solution to increase tumor responses by at least 2.27 dB, as well as to decrease mutual coupling effects between array elements, compared to the same system with planar bow-tie antennas.

Competing imaging results (successful detection of tumor with 2 mm diameter in quasi-heterogeneous breast phantom) have been obtained by the spherical conformal bow-tie antennas in the simulation environment, as compared to those obtained by the similar recent developed microwave imaging systems (Table 1.2). The obtained simulation results are reasonably reliable and promising; however more work is required with anatomically more realistic breast phantom models. Analytical and numerical investigations in Section 2

were very helpful in the design part of the new UWB microwave imaging system, as well as that of the spherical conformal antennas.

Beside that new contribution of the conformal antenna structure, DAS algorithm has been also successfully developed and tested with the quasi-heterogeneous and dispersive breast phantom model, by using a method for compensation of the velocity errors in the imaging algorithm, too. On the other hand, a closed form solution is presented for the electromagnetic field scattered due to a lossy dielectric spherical tumour with arbitrary diameter, inside a lossy dielectric breast fat tissue medium, for the first time.

In the first experimental study, constructed realistic elastic tumor model with 2 cm diameter has been detected by using so many frequency and position dependent raw data obtained from the stacked microstrip patch antenna, although dielectric properties of tumor and breast have been close to each other compared to the PEC object. In the second experimental study, fabricated Vivaldi antennas by TUBITAK-BILGEM-UEKAE are tested for the breast tumor detection. In this experimental study, quasi-realistic and homogeneous breast and tumor phantom models are used. Tumor simulating spherical PEC objects with 8 mm and 10 mm diameters embedded in the homogeneous breast phantoms have been detected by using Small and Large Vivaldi antennas, in the imaging results of the experimental study.

In particular, in order to improve the UWB microwave imaging system, effort is warranted in the following areas:

- Anatomically more realistic breast phantom models derived from MRI data of real patients' breasts should also be used, including chest wall and nipple in the models. The UWB microwave imaging system that has been tested with the quasi-realistic breast phantom models is also expected to be successful with the anatomically realistic breast phantom models.
- Smaller spherical conformal bow-tie antennas should be designed and fabricated to encircle the whole breast with many antennas to increase the dynamic range. Conformal antenna curvature could also be optimized to resonance with the spherical waves inside the breast better.

- Imaging algorithms such as MAMI could also be used and tested to be more successful for detection of the tumor hidden inside the "heterogeneously dense" or "very dense" breasts. However, DAS algorithm has been given considerably good imaging results with the quasi-realistic breast phantom models, too.

- Since current imaging results are obtained in long time intervals, effective usage of all the cores of the computer should be investigated to obtain 3D imaging results.

- Since Small Vivaldi antenna has been designed and fabricated to operate perfectly in the coupling medium, more convenient experimental measurement set-ups should be prepared to embed and operate the antenna in the coupling medium for the UWB radar-based microwave imaging system.

7. REFERENCES

1. Globocan, Cancer Incidence, Mortality and Prevalence Worldwide, *IARC Cancer Base No. 5*, *Version 2.0*, IARC Press, Lyon, 2008.

2. Gail, M. H., L. A. Brinton and D. P. Byar, "Projecting Individualized Probabilities of Developing Breast Cancer for White Females Who Are Being Examined Annually", *J. Natl. Cancer Inst*, Vol. 81, pp. 1879-86, 1989.

3. Guo, B., *Microwave Techniques for Breast Cancer Detection and Treatment*, Ph.D. Dissertation, University of Florida, 2007.

4. Hassan, A. M. and M. El-Shenawee, "Review of Electromagnetic Techniques for Breast Cancer Detection", *IEEE Reviews in Biomedical Engineering*, Vol. 4, pp. 103-118, 2011.

5. Huynh, P., A. Jarolimek and S. Daye, "The False Negative Mammogram", *Radiographics*, Vol. 18, pp. 1137-1154, 1998.

6. Nass, S., I. Henderson and J. Lashof, "Developing Technologies for the Early Detection of Breast Cancer", in National Cancer Policy Board (eds.), *Mammography and Beyond*, National Academy Press, USA, 2001.

7. Mohammed, B. J., A. M. Abbosh and M. E. Bialkowski, "Design of Tapered Slot Antenna Operating In Coupling Liquid for Ultrawideband Microwave Imaging Systems", *APSURSI*, Washington, USA, pp. 145-148, 2011.

8. Fear, E. C., X. Li, S. C. Hagness and M. A. Stuchly, "Confocal Microwave Imaging For Breast Tumor Detection: Localization In Three Dimensions", *IEEE Trans. Antennas Propag.*, Vol. 49, No. 8, pp. 812-822, 2002.

9. Fang, Q., *Computational Methods for Microwave Medical Imaging*, Ph.D. Dissertation, Thayer School of Engineering, Dartmouth College, 2004.

10. Stang, J. P., *A 3D Active Microwave Imaging System for Breast Cancer Screening*, Ph.D. Dissertation, Department of Electrical and Computer Engineering, Duke University, 2008.

11. Carr, K. L., "Microwave Radiometry: Its Importance to The Detection of Cancer", *IEEE Trans. Microwave Theory and Tech.*, Vol. 37, No. 12, pp. 1862-1869, 1989.

12. Wang, L. V., X. Zhao, H. Sun and G. Ku, "Microwave-Induced Acoustic Imaging for Biological Tissues", *Rev. Sci. Instrum.*, Vol. 70, No. 9, pp. 3744-3748, 1999.

13. Bulyshev, A. E., S. Y. Semenov, A. E. Souvorov, R. H. Svenson, A. G. Nazarov, Y. E. Sizov and G. P. Tatsis, "Computational Modelling of Three-Dimensional Microwave Tomography of Breast Cancer", *IEEE Trans. Biomed. Eng.*, Vol. 48, No. 9, pp. 1053-1056, 2001.

14. Bond, E. J., X. Li, S. C. Hagness and B. D. Van Veen, "Microwave Imaging via Space-Time Beamforming for Early Detection of Breast Cancer", *IEEE Trans. Antennas Propag.*, Vol. 51, No. 8, pp. 1690-1705, 2003.

15. Klemm, M., I. J. Craddock, J. A. Leendertz, A. Preece and R. Benjamin, "Radar-based Breast Cancer Detection Using a Hemispherical Antenna Array-Experimental Results", *IEEE Trans. Antennas Propag.*, Vol. 57, No. 6, pp. 1692-1704, 2009.

16. Klemm, M., J. A. Leendertz, D. Gibbins, I. J. Craddock, A. Preece and R. Benjamin, "Microwave Radar-Based Differential Breast Cancer Imaging: Imaging in Homogeneous Breast Phantoms and Low Contrast Scenarios", *IEEE Trans. Antennas Propag.*, Vol. 58, No. 7, pp. 2337-2344, 2010.

17. Klemm, M., D. Gibbins, J. Leendertz, T. Horseman, A. W. Preece, R. Benjamin and I. J. Craddock, "Development and Testing of A 60-element UWB Conformal Array for

Breast Cancer Imaging", *Proc. 5th European Conf. on Antennas and Propagation*, Rome, Italy, pp. 3077-3079, 2011.

18. Bialkowski, M., D. Ireland, Y. Wang and A. Abbosh, "Ultra-Wideband Array Antenna System for Breast Imaging", *Proc. Asia-Pacific Microwave Conference*, Yokohama, Japan, 7-10 October, pp. 267-270, 2010.

19. Ünal, İ., B. Türetken, U. Buluş and C. Canbay, "Konformal Antenler Kullanarak Meme Kanseri Tümörünün Radar-Tabanlı Mikrodalga Görüntüleme Tekniği ile Tespit Edilmesi", *BİYOMUT 2012*, Boğaziçi University, İstanbul, 3-5 October, pp. 1-4, 2012.

20. Ünal, İ., B. Türetken, U. Buluş and C. Canbay, "Analysis of Dispersive Effects of Breast Phantom Model on Ultra Wideband Microwave Imaging of Breast Cancer Tumor", *BIOMED 2013*, Innsbruck, Austria, 13-15 February, pp. 1-6, 2013.

21. Ünal, İ., B. Türetken, U. Buluş and C. Canbay, "Spherical Conformal Bow-tie Antenna for Ultra Wideband Microwave Imaging of Breast Cancer Tumor", submitted to *ACES Journal*. (under review)

22. Zhao, Y., W. Shao and G. Wang, "UWB Microwave Imaging for Early Breast Cancer Detection: Effect of Two Synthetic Antenna Array Configurations", *IEEE Int. Conference on Systems, Man and Cybernetics*, The Hague, Netherlands, pp. 4468-4473, 2004.

23. Shao, W., J. Li and R. Wu, "UWB Microwave Imaging for Breast Tumor Detection In Inhomogeneous Tissue", *Proceedings of the 2005 IEEE, Engineering in Medicine and Biology 27th Annual Conference*, Shanghai, China, 1-4 September, pp. 1-4, 2005.

24. Li, X., S. K. Davis, S. C. Hagness, D. W. van der Weide and B. D. Van Veen, "Microwave Imaging via Space-Time Beamforming: Experimental Investigation of Tumor Detection In Multilayer Breast Phantoms", *IEEE Trans. Microw. Theory Tech.*, Vol. 52, No. 8, pp. 1856-1865, 2004.

25. Li, X., E. J. Bond, B. D. Van Veen, D. W. van der Weide and S. C. Hagness, "An Overview of Ultra-Wideband Microwave Imaging Via Space-Time Beamforming for Early-Stage Breast-Cancer Detection", *IEEE Antennas and Propagation Magazine*, Vol. 47, No. 1, pp. 19-34, 2005.

26. Wang, Z., J. Li and R. Wu, "Time-Delay- and Time-Reversal-Based Robust Capon Beamformers for Ultrasound Imaging", *IEEE Trans. Medical Imaging*, Vol. 24, No. 10, pp. 1308-1322, 2005.

27. Xie, Y., B. Guo, L. Xu, J. Li and P. Stoica, "Multistatic Adaptive Microwave Imaging for Early Breast Cancer Detection", *IEEE Trans. Biomedical Engineering*, Vol. 53, No. 8, pp. 1647-1657, 2006.

28. Byrne, D., M. O'Halloran, E. Jones and M. Glavin, "The Effects of Breast Tissue Heterogeneity on Data-adaptive Beamforming", *Progress In Electromagnetics Research Symposium Proceedings*, Cambridge, USA, 5-8 July, pp. 915-920, 2010.

29. Kopans, D. B., *Breast Imaging*, Lippincott Williams & Wilkins, 2007.

30. Hughes, L. E., R. E. Mansel and D. Webster, *Benign Disorders and Diseases of the Breast*, W. B. Saunders, 2000.

31. Isaacs, J. H., *Textbook of Breast Disease*, Mosby, 1992.

32. Mandelson, M. T., N. Oestreicher and P. L. Porter, "Breast Density As a Predictor of Mammographic Detection: Comparison of Interval- and Screen Detected Cancers", *J. Natl. Cancer Inst.*, Vol. 92, pp. 1081-1087, 2000.

33. Pisano, E. D., C. Gastonis and E. Hendrick, "Diagnostic Performance of Digital Versus Film Mammography for Breast Cancer Screening", *N. Engl. J. Med.*, Vol. 353, pp. 1-11, 2005.

34. Huynh, P. T., A. M. Jarolimek and S. Daye, "The False-Negative Mammogram", *Radiograph*, Vol. 18, pp. 1137-1154, 1998.

35. Saslow, D., C. Boetes and W. Burke, "American Cancer Society Guidelines for Breast Screening With MRI As an Adjunct to Mammography", *CA Cancer J. Clin.*, Vol. 57, pp. 75-89, 2007.

36. Park, J. M., E. A. Franken, Jr. M. Garg, L. L. Fajardo and L. T. Niklason, "Breast Tomosynthesis: Present Considerations and Future Applications", *RadioGraphics*, Vol. 27, pp. 231-240, 2007.

37. Kopans, D. B., "Breast Cancer Screening with Ultrasonography", *Lancet*, Vol. 354, pp. 2096-2097, 1999.

38. Kaplan, S. S., "Clinical Utility of Bilateral Whole-Breast US In the Evaluation of Women with Dense Breast Tissue", *Radiology*, Vol. 221, pp. 641-649, 2001.

39. Elmore, J. G., "Screening for Breast Cancer", *JAMA*, Vol. 293, pp. 1245-1256, 2005.

40. Lin, S. P. and J. J. Brown, "MR Contrast Agents: Physical and Pharmacologic Basics", *J. Magn. Reson. Imaging*, Vol. 25, pp. 884-889, 2007.

41. Liberman, L., T. L. Feng, D. D. Dershaw, E. A. Morris, A. F. Abramson and J. J. Brown, "US Guided Core Breast Biopsy: Use and Cost Effectiveness", *Radiology*, Vol. 208, pp. 717-723, 1998.

42. Kerner, T., K. Paulsen, A. Hartov, S. Soho and S. Poplack, "Electrical Impedance Spectroscopy of The Breast: Clinical Imaging Results In 26 Subjects", *IEEE Trans. Med. Imag.*, Vol. 21, No. 6, pp. 638-645, 2002.

43. Ng, E., S. Sree, K. Ng and G. Kaw, "The Use of Tissue Electrical Characteristics for Breast Cancer Detection: A Perspective Review", *Technol. Cancer Res. Treatment*, Vol. 7, No. 4, pp. 295-308, 2008.

44. Bera, T., S. Biswas, K. Rajan and J. Nagaraju, "Improving Image Quality In Electrical Impedance Tomography (EIT) Using Projection Error Propagation-Based Regularization (PEPR) Technique: A Simulation Study", *J. Electr. Bioimp.*, Vol. 2, pp. 2-12, 2011.

45. Konecky, S., *Non-Invasive Imaging of Breast Cancer with Diffusing Near-Infrared Light*, Ph.D. Dissertation, Univ. Pennsylvania, Philadelphia, PA, 2007.

46. Poplack, S., T. Tosteson, W. Wells, B. Pogue, P. Meaney, A. Hartov, C. Kogel, S. Soho, J. Gibson and K. Paulsen, "Electromagnetic Breast Imaging: Results of a Pilot Study In Women with Abnormal Mammograms", *Radiology*, Vol. 243, pp. 350-359, 2007.

47. Anninos, P., A. Kotini, N. Koutlaki, A. Adamopouos, G. Galazios and P. Anastasiadis, "Differential Diagnosis of Breast Lesions by Use of Biomagnetic Activity and Non-Linear Analysis", *Eur. J. Gynaecolog. Oncol.*, Vol. 21, No. 6, pp. 591-595, 2000.

48. Kotini, A., A. Anastasiadis, N. Koutlaki, D. Tamiolakis, P. Anninos and P. Anastiadis, "Biomagnetism In Gynaecologic Oncology: Our Experience In Greece", *Eur. J. Gynaecolog. Oncol.*, Vol. 27, No. 6, pp. 594-596, 2006.

49. Anastasiadis, P., P. Anninos and E. Sivridis, "Biomagnetic Activity In Breast Lesions", *Breast*, Vol. 3, pp. 177-180, 1994.

50. Baillet, S., J. Mosher and R. Leahy, "Electromagnetic Brain Mapping", *IEEE Signal Processing Mag.*, Vol. 18, No. 6, pp. 14-30, 2001.

51. Fear, E., S. Hagness, P. M. Okoniewski and M. Stuchly, "Enhancing Breast Tumor Detection with Near-Field Imaging", *IEEE Microw. Mag.*, Vol. 3, No. 1, pp. 48-56, 2002.

52. Ünal, İ., B. Türetken, U. Buluş and C. Canbay, "Analysis of the Electromagnetic Field Scattered by a Spherical Breast Tumour Model", *URSI-EMTS 2013*, Hiroshima, Japan, 20-24 May, pp. 1-4, 2013. (*accepted for poster presentation*)

53. Poplack, S., T. Tosteson, W. Wells, B. Pogue, P. Meaney, A. Hartov, C. Kogel, S. Soho, J. Gibson and K. Paulsen, "Electromagnetic Breast Imaging: Results of A Pilot Study In Women with Abnormal Mammograms", *Radiology*, Vol. 243, pp. 350-359, 2007.

54. Klemm, M., I. J. Craddock, J. A. Leendertz, A.W. Preece and R. Benjamin, "Experimental and Clinical Results of Breast Cancer Detection Using UWB Microwave Radar", *Antennas and Propagation Society International Symposium*, San Diego, California, United States, 5-11 July, pp. 1-4, 2008.

55. Meaney, P. M., M. W. Fanning, T. Zhou, A. Golnabi, S. D. Geimer and K. D. Paulsen, "Clinical Microwave Breast Imaging – 2D Results and Evolution to 3D", *Int. Conference on Electromagnetics in Advanced Applications*, Torino, Italy, 14-18 September, pp. 881-884, 2009.

56. Hagness, S. C., A. Taflove and J. E. Bridges, "Two-Dimensional FDTD Analysis of Pulsed Microwave Confocal System for Breast Cancer Detection: Fixed-Focus and Antenna-Array Sensors", *IEEE Trans. Biomed. Eng.*, Vol. 45, No. 12, pp. 1470-1479, 1998.

57. Hagness, S. C., A. Taflove and J. E. Bridges, "Three-dimensional FDTD Analysis of Pulsed Microwave Confocal System for Breast Cancer Detection: Design of An Antenna-Array Element", *IEEE Trans. Antennas and Propagat.*, Vol. 47, No. 5, pp. 783-791, 1999.

58. Daniels, D. J., *Surface Penetrating Radar*, IEEE Press, London, 1996.

59. Li, X. and S. C. Hagness, "A Confocal Microwave Imaging Algorithm for Breast Cancer Detection", *IEEE Microwave and Wireless Components Letters*, Vol. 11, No. 3, pp. 130-132, 2001.

60. Xie, Y., B. Guo, J. Li and P. Stoica, "Novel Multistatic Adaptive Microwave Imaging Methods for Early Breast Cancer Detection", *EURASIP J. Appl. Si. P.*, Vol. 91961, pp. 1-13, 2006.

61. Guo, B., Y. Wang, J. Li, P. Stoica and R. Wu, "Microwave Imaging via Adaptive Beamforming Methods for Breast Cancer Detection", *Progress In Electromagnetics Research Symposium*, Hangzhou, China, 22-26 August, pp. 350-353, 2005.

62. Lazebnik, M., M. Okoniewski, J. H. Booske and S. C. Hagness, "Highly Accurate Debye Models for Normal and Malignant Breast Tissue Dielectric Properties at Microwave Frequencies", *IEEE Microwave and Wireless Components Letters*, Vol. 17, No. 12, pp. 822-824, 2007.

63. Meaney, P., M. Fanning, D. Li, S. Poplack and K. Paulsen, "A Clinical Prototype for Active Microwave Imaging of The Breast", *IEEE Trans. Microw. Theory Techniques*, Vol. 48, No. 11, pp. 1841-1853, 2000.

64. Golnabi, A. H., P. M. Meaney, S. Geimer and K. D. Paulsen, "Microwave Imaging for Breast Cancer Detection and Therapy Monitoring", *IEEE Topical Conference on Biomedical Wireless Technologies, Networks, and Sensing Systems (BioWireleSS)*, Phoenix, AZ, 16-19 January, pp. 59-62, 2011.

65. Sill, J. F. and E. C. Fear, "Tissue Sensing Adaptive Radar for Breast Cancer Detection-Experimental Investigation of Simple Tumor Models", *IEEE Trans. Microw. Theory Techniques*, Vol. 53, No. 11, pp. 3312-3319, 2005.

66. Yu, C., M. Q. Yuan, J. Stang, E. Bresslour, R. T. George, G. A. Ybarra, W. T. Joines and Q. H. Liu, "Active Microwave Imaging II: 3-D System Prototype and Image

Reconstruction From Experimental Data", *IEEE Trans. Microw. Theory Techniques*, Vol. 56, No. 4, pp. 991-1000, 2008.

67. Rubæk, T. and V. Zhurbenko, "Phantom Experiments with A Microwave Imaging Sstem for Breast-Cancer Screening", *3rd European Conference on Antennas and Propagation*, Berlin, Germany, 23-27 March, pp. 2950-2954, 2009.

68. Bialkowski, M. E., "Ultra Wideband Microwave System with Novel Image Reconstruction Strategies for Breast Cancer Detection", *Proceedings of the 40th European Microwave Conference*, Paris, France, 28-30 September, pp. 537-540, 2010.

69. Ünal, İ., B. Türetken, K. Sürmeli and C. Canbay, "An Experimental Microwave Imaging System for Breast Tumor Detection on Layered Phantom Model", *URSI GASS 2011*, İstanbul, Turkey, pp. 1-4, 2011.

70. Hagness, S. C., A. Taflove and J. E. Bridges, "Wideband Ultralow Reverberation Antenna for Biological Sensing", *Electronics Letters*, Vol. 33, No. 19, pp. 1594-1595, 1997.

71. Yun, X., E. C. Fear and R. H. Johnston, "Compact Antenna for Radar-Based Breast Cancer Detection", *IEEE Trans. Antennas Propag.*, Vol. 53, No. 8, pp. 2374-2380, 2005.

72. Kanj, H. and M. Popovic, "Two-Element T-Array for Cross-Polarized Breast Tumor Detection", *Applied Computational Electromagnetics Society (ACES) Journal*, Vol. 23, No. 3, pp. 249-254, 2008.

73. Tavassolian, N., S. Nikolaou and M. M. Tentzeris, "A Flexible UWB Elliptical Slot Antenna with A Tuning Uneven U-Shape Stub on LCP for Microwave Tumor Detection", *Asia-Pasific Microwave Conference*, Bangkok, Thailand, pp. 1-4, 2007.

74. Gibbins, D., M. Klemm, I. J. Craddock, J. A. Leendertz, A. Preece and R. Benjamin, "A Comparison of a Wide-Slot and A Stacked Patch Antenna for The Purpose of

Breast Cancer Detection", *IEEE Trans. Antennas Propag.*, Vol. 58, No. 3, pp. 665-674, 2010.

75. Bourqui, J., M. Okoniewski and E. C. Fear, "Balanced Antipodal Vivaldi Antenna for Breast Cancer Detection", *The Second European Conference on Antennas and Propagation*, Edinburgh, UK, pp. 1-5, 2007.

76. Stang, J. P., W. T. Joines, Q. H. Liu, G. A. Ybarra, R. T. George, M. Yuan and I. Leonhardt, "A Tapered Microstrip Patch Antenna Array for Use in Breast Cancer Screening via 3D Active Microwave Imaging", *Antennas and Propagation Society Int. Symposium*, Charleston, SC, USA, pp. 1-4, 2009.

77. Akmehmet, M. C., İ. Ünal and C. Canbay, "Dispersif ve Kayıplı Ortamda Keyfi Polarizasyonlu Antenler Arasındaki Elektromanyetik Etkileşimin İncelenmesi", *I. ULUSAL EMC (Elektromanyetik Uyumluluk) Konferansı*, Doğuş Üniversitesi, İstanbul, 14-16 September, pp. 1-4, 2011.

78. Ünal, İ., B. Türetken, U. Buluş and C. Canbay, "Spherical Conformal Bow-tie Antenna for Ultra Wideband Microwave Imaging of Breast Cancer Tumor", submitted to *ACES Journal*. (under review)

79. Gabriel, C., S. Gabriel and G. Corthout, "The Dielectric Properties of Biological Tissues: III. Parametric Models for The Dielectric Spectrum of Tissues", *Phys. Med. Biol.*, Vol. 41, No. 11, pp. 2271-2293, 1996.

80. Yun, X., R. H. Johnston and E. C. Fear, "Radar-Based Microwave Imaging for Breast Cancer Detection: Tumor Sensing with Cross-Polarized Reflections", *Antennas and Propagation Society Int. Symposium*, California, USA, pp. 2432-2435, 2004.

81. Wang, Y., A. E. Faty and M. R. Mahfouz, "Novel Compact Tapered Microstrip Slot Antenna for Microwave Breast Imaging", *AP-S/URSI*, pp. 2119-2122, 2011.

82. Abbosh, A. A. and M. E. Bialkowski, "Tapered Slot Antenna for Near-Field Microwave Imaging", *International Symposium on Antennas and Propagation ISAP*, Singapore, 1-4 November, pp. 1-4, 2006.

83. Jafari, H. M., J. M. Deen, S. Hranilovic and N. K. Nikolova, "Co-Polarised and Cross-Polarised Antenna Arrays for Breast Cancer Detection", *IET Microw. Antennas Propag.*, Vol. 1, No. 5, pp. 1055-1058, 2007.

84. Abbosh, A. A. and M. E. Bialkowski, "Compact Directional Antenna for Ultra Wideband Microwave Imaging Systems", *APS-URSI*, USA, pp. 1-4, 2009.

85. Cheng, D. K., *Field and Wave Electromagnetics*, Addison-Wesley Publishing Company, Inc., 1989.

86. Wait, J. R., *Electromagnetic Waves in Stratified Media*, Oxford University Press, USA, 1996.

87. Ünal, İ. and C. Canbay, "*N*-Katmanlı, Kayıplı, Dispersif Düzlemsel Tabakaların Elektriksel Özelliklerinin ve Kalınlıklarının Elektromagnetik Yöntemle Kestirilmesi", *V. URSI Türkiye 2010 Bilimsel Kongresi ve Ulusal Genel Kurul Toplantısı*, ODTU Kuzey Kıbrıs Yerleşkesi, 25-27 August, pp. 1-4, 2010.

88. Zhang, Z. Q., Q. H. Liu, C. Xiao, E. Ward, G. Ybarra and W. T. Joines, "Microwave Breast Imaging: 3-D Forward Scattering Simulation", *IEEE Trans. Biomed. Eng.*, Vol. 50, pp. 1180-1189, 2003.

89. Senaratne, G. G., R. B. Keam, W. L. Sweatman and G. C. Wake, "Microwave Scattering at Malignant Tissue Boundaries: A New Method for Breast Screening", *SICE-ICASE*, pp. 193-197, 2006.

90. Abbosh, A. M., M. E. Bialkowski and S. Crozier, "Investigations Into Optimum Characteristics for The Coupling Medium In UWB Breast Cancer Imaging Systems", *IEEE Antennas and Propagation Symp.*, pp. 1-4, 2008.

91. Abbosh, A. M., M. E. Bialkowski and S. Crozier, "A Simple Model for Electromagnetic Scattering Due to Breast Tumour", *IEEE Antennas and Propagation Symp.*, pp. 1-4, 2008.

92. Abbosh, A. M. and A. A. Bakar, "Three-Dimensional Modeling of Electromagnetic Scattering From Breast Tumor", *Proc. Asia-Pacific Microwave Conference*, pp. 1384-1387, 2010.

93. Simonov, N. A., S. I. Jeon, S. H. Son, J. M. Lee and H. J. Kim, "Modeling Signals of Small Tumors Inside The Breast In Ultra-Wide Frequency Band", *Proc. 5th European Conference on Antennas and Propagation*, pp. 493-497, 2011.

94. Harrington, R. F., *Time-Harmonic Electromagnetic Fields*, Wiley-IEEE Press, USA, 2001.

95. Zastrow, E., S. K. Davis, M. Lazebnik, F. Kelcz, B. D. Van Veen and S. C. Hagness, "Development of Anatomically Realistic Numerical Breast Phantoms with Accurate Dielectric Properties for Modeling Microwave Intereactions with The Human Breast", *IEEE Trans. Biomed. Eng.*, Vol. 55, pp. 2792-2800, 2008.

96. Hagness, S. C., A. Taflove and J. Bridges, "Three Dimensional FDTD Analysis of A Pulsed Microwave Confocal System for Breast Cancer Detection", *IEEE Trans. Antennas. Propag.*, Vol. 47, pp. 783-791, 1999.

97. Balanis, C. A., *Antenna Theory, Analysis and Design*, 3rd ed., John Wiley & Sons, New York, 2005.

98. Canbay, C., *Anten ve Propagasyon I*, Yeditepe Üniversitesi Press, İstanbul, 1997.

99. Akmehmet, M. C., *Coupling Analysis among the Special Smart Antenna Elements*, M.Sc. Thesis, Yeditepe University, 2009.

100. Pozar, D. M., "Microstrip Antennas", *Proc. of the IEEE*, Vol. 80, pp. 79-91, 1992.

101. Bayrakçı, E., *Antenlerin Teorisi ve Tekniği*, Güneş Kitabevi, 1992.

102. Khor, W. C., F. Y. Hui, M. E. Bialkowski and S. Crozier, "Investigations into Microwave Properties of Various Substances to Develop a Breast Phantom for a UWB Breast Tumour Radar Detecting System", *17th International Conference on Microwaves, Radar and Wireless Communications*, Wroclaw, PL, pp. 1-4, 2008.

103. Ortega-Palacios, R., L. Leija, A. Vera and M. F. J. Cepeda, "Measurement of Breast - Tumor Phantom Dielectric Properties For Microwave Breast Cancer Treatment Evaluation", *7th International Conference on Electrical Engineering, Computing Science and Automatic Control (CCE 2010)*, Tuxtla Gutierrez, MX, pp. 216-219, 2010.

104. Primak, S., J. LoVetri and B. Zhang, Microwave Image Reconstruction Methods" *RTO SET Lecture Series on* "Advanced Pattern Recognition Techniques", Bristol, UK, 14-15 September, 1998; Rome, Italy, 17-18 September, 1998; Lisbon, Portugal, 21-22 September, 1998.

105. Winters, D. W., J. D. Shea, E. L. Madsen, G. R. Frank, B. D. Van Veen and S. C. Hagness, "Estimating the Breast Surface Using UWB Microwave Monostatic Backscatter Measurements", *IEEE Trans. Biomed. Eng.*, Vol. 55, pp. 247-256, 2008.

106. Ünal, İ., B. Türetken, U. Buluş and C. Canbay, "Meme Kanseri Tümörünün Tespit Edilmesi İçin Geliştirilen Mikrodalga Görüntüleme Sisteminin, Kalp Pili Kullananlar İçin Elektromanyetik Bağışıklık Açısından İncelenmesi", I. *ULUSAL EMC (Elektromanyetik Uyumluluk) Konferansı*, İstanbul, Turkey, 14-16 September, pp. 1-4, 2011.

107. Schenke, S., L.-O. Fichte, F. Sutter, M. Clemens and S. Dickmann, "Electromagnetic Field Coupling Into Cardiac Pacemaker Systems – Numerical Simulation Using Body Models with Dispersive Dielectric Tissues", *IEEE International Symposium on Electromagnetic Compatibility*, 17-21 August, pp. 258-261, 2009.

108. Ferhanoğlu, O., A. Altıntaş and E. Atalar, "Kalp Pillerinin Manyetik Rezonans Görüntüleme Esnasında Yarattığı Sıcaklık Artışı", *URSI-Türkiye'2004 Bilimsel Kongresi ve Ulusal Genel Kurul Toplantısı*, Bilkent Üniversitesi, Ankara, 8-10 September, pp. 1-4, 2004.

109. Smith, S. and R. Aasen, "The Effects of Electromagnetic Fields on Cardiac Pacemakers", *IEEE Trans. Broadcasting*, Vol. 38, pp. 136-139, 1992.

110. American National Standard. ANSI/AAMI PC69:2007 Active implantable medical devices–electromagnetic compatibility–emc test protocols for implantable cardic pacemakers and implantable cardioverter defibrillators, 2007.

111. Wang, J. and v, "Modeling of Electromagnetic Interference to an Implanted Cardiac Pacemaker due to Mobile Phones", *IEEE International Symposium on Electromagnetic Compatibility*, Washington, DC, USA, 25-29 August, pp. 209-212, 2000.

112. Ybarra, G. A., Q. H. Liu, W. T. Joines and J. Stang, "Microwave breast imaging," in J. S. Suri, R. Rangayyan and S. Laxminarayan (eds.), *Emerging Technologies in Breast Imaging and Mammography*, ch. 16, American Scientific Publishers, 2006.

113. Tavasolian, N., H. Kanj and M. Popović, "The Effect of Breast Glands on Microwave Tumor Sensing with "Dark Eyes" Antenna", *Antennas and Propagation Society Int. Symposium*, Albuquerque, NM, USA, pp. 291-294, 2006.

114. Šipuš, Z., S. Škokić and N. Burum, "Performance Analysis of Spherical Stacked-Patch Antennas", *18th Int. Conference on Applied Electromagnetics and Communications*, Dubrovnik, Croatia, pp. 1-4, 2005.

115. Conceição, R. C., M. O'Halloran, M. Glavin and E. Jones, "Comparison of Planar and Circular Antenna Configurations for Breast Cancer Detection Using Microwave Imaging", *Progress In Electromagnetics Research*, PIER 99, pp. 1-20, 2009.

116. Jafari, H. M., M. J. Deen, S. Hranilovic and N. K. Nikolova, "A Study of Ultra-Wideband Antennas Operating In a Biological Medium", *IEEE Trans. Antennas Propag.*, Vol. 55, No. 4, pp. 1184-1188, 2007.

117. Boese, F. G., "On Impulse Distortion In Dispersive Media", *Proc. Appl. Math. Mech.*, Vol. 6, No. 1, pp. 603-604, 2006.

118. Oughstun, K. E., "Pulse Propagation In a Linear, Causally Dispersive Medium", *Proc. IEEE*, Vol. 79, No. 10, pp. 1379-1390, 1991.

119. Lamensdorf, D. and L. Susman, "Baseband-Pulse-Antenna Techniques", *IEEE Antennas Propag. Magazine*, Vol. 36, No. 1, pp. 20-30, 1994.

120. Winters, D. W., J. D. Shea, P. Kosmas, B. D. Van Veen and S. C. Hagness, "Three-Dimensional Microwave Breast Imaging: Dispersive Dielectric Properties Estimation Using Patient-Specific Basis Functions", *IEEE Trans. Medical Imag.*, Vol. 28, No. 7, pp. 969-981, 2009.

121. Ünal, İ., B. Türetken, U. Buluş and C. Canbay, "Konformal Antenler Kullanarak Meme Kanseri Tümörünün Radar-Tabanlı Mikrodalga Görüntüleme Tekniği ile Tespit Edilmesi", *BİYOMUT 2012*, Boğaziçi Üniversitesi, İstanbul, 3-5 October, pp. 1-4, 2012.

122. Rohde&Schwarz GmbH & Co. KG, ZNB 8 Vector Network Analyzer, Product Data Sheet.

123. Gibson, P. J., "The Vivaldi Aerial", *Proc. 9th Europe Microwave Conference*, pp. 101-105, 1979.

124. Hamzah, N. and K. A. Othman, "Designing Vivaldi Antenna with Various Sizes using CST Software", *Proceedings of the World Congress on Engineering Vol II, WCE 2011*, London, UK, 6-8 July, pp. 1-4, 2011.

125. Mehdipour, A., K. Mohammadpour-Aghdam and R. Faraji-Dana, "Complete Dispersion Analysis of Vivaldi Antenna for Ultra Wideband Applications", PIER 77, pp. 85-96, 2007.

126. Açıkalın, E., A. Vertiy, A. Sayıntı and K. Çoban, "Complex Dielectric Coefficient of Breast Phantom Prepared For Breast Cancer Detection", *2nd International Advances in Applied Physics & Materials Science Congress*, April, pp. 1-4, 2012.

127. Ludwig, R. and P. Bretchko, *RF Circuit Design*, Prentice Hall Inc., 2000.

APPENDIX A: APPLYING BOUNDARY CONDITIONS

Electric and magnetic field components can be easily computed by using Equation (2.25) and Equation (2.26), as follows:

Let us compute E_θ^+, by using $E_\theta^+ = \dfrac{-1}{r\sin(\theta)}\dfrac{\partial F_r^+}{\partial \phi} + \dfrac{1}{r(\sigma + j\omega\varepsilon)}\left(\dfrac{\partial^2 A_r^+}{\partial r\,\partial \theta}\right)$ as;

$$\frac{\partial F_r^+}{\partial \phi} = \frac{E_0}{k}\cos(\phi)\sum_{n=1}^{\infty}\left[a_n\,\hat{J}_n(kr) + c_n\,\hat{H}_n^{(2)}(kr)\right]P_n^1(\cos(\theta)) \tag{A.1}$$

$$\left(\frac{\partial^2 A_r^+}{\partial r\,\partial \theta}\right) = \frac{E_0}{\omega\mu}\cos(\phi)\sum_{n=1}^{\infty}\left[a_n\frac{\partial \hat{J}_n(kr)}{\partial r} + b_n\frac{\partial \hat{H}_n^{(2)}(kr)}{\partial r}\right]\frac{\partial P_n^1(\cos(\theta))}{\partial \theta} \tag{A.2}$$

At $r=a$, E_θ^+ is expressed as:

$$\begin{aligned}
E_\theta^+ = &\frac{-1}{a\sin(\theta)}\left[\frac{E_0}{k}\cos(\phi)\sum_{n=1}^{\infty}\left[a_n\,\hat{J}_n(ka) + c_n\,\hat{H}_n^{(2)}(ka)\right]P_n^1(\cos(\theta))\right]\\
&+\frac{1}{a(\sigma + j\omega\varepsilon)}\left(\frac{E_0 k}{\omega\mu}\cos(\phi)\sum_{n=1}^{\infty}\left[a_n\,\hat{J}_n'(ka) + b_n\,\hat{H}_n^{(2)\prime}(ka)\right]\frac{\partial P_n^1(\cos(\theta))}{\partial \theta}\right)
\end{aligned} \tag{A.3}$$

Let us compute E_ϕ^+, by using $E_\phi^+ = \dfrac{1}{r}\dfrac{\partial F_r^+}{\partial \theta} + \dfrac{1}{r\sin(\theta)(\sigma + j\omega\varepsilon)}\left(\dfrac{\partial^2 A_r^+}{\partial r\,\partial \phi}\right)$ as;

$$\frac{\partial F_r^+}{\partial \theta} = \frac{E_0}{k}\sin(\phi)\sum_{n=1}^{\infty}\left[a_n\,\hat{J}_n(kr) + c_n\,\hat{H}_n^{(2)}(kr)\right]\frac{\partial P_n^1(\cos(\theta))}{\partial \theta} \tag{A.4}$$

$$\left(\frac{\partial^2 A_r^+}{\partial r\,\partial \phi}\right) = \frac{-E_0 k}{\omega\mu}\sin(\phi)\sum_{n=1}^{\infty}\left[a_n\,\hat{J}_n'(kr) + b_n\,\hat{H}_n^{(2)\prime}(kr)\right]P_n^1(\cos(\theta)) \tag{A.5}$$

At $r=a$, E_ϕ^+ is expressed as:

$$E_\phi^+ = \frac{1}{a}\left[\frac{E_0}{k}\sin(\phi)\sum_{n=1}^{\infty}\left[a_n\,\hat{J}_n(ka)+c_n\,\hat{H}_n^{(2)}(ka)\right]\frac{\partial P_n^1(\cos(\theta))}{\partial\theta}\right]$$
$$+\frac{-1}{a(\sigma+j\omega\varepsilon)\sin(\theta)}\left(\frac{E_0 k}{\omega\mu}\sin(\phi)\sum_{n=1}^{\infty}\left[a_n\,\hat{J}_n'(ka)+b_n\,\hat{H}_n^{(2)\prime}(ka)\right]P_n^1(\cos(\theta))\right) \qquad (A.6)$$

Let us compute H_θ^+, by using $H_\theta^+ = \frac{1}{r\sin(\theta)}\frac{\partial A_r^+}{\partial\phi}+\frac{1}{r(j\omega\mu)}\left(\frac{\partial^2 F_r^+}{\partial r\partial\theta}\right)$ as;

$$\frac{\partial A_r^+}{\partial\phi}=-\frac{E_0}{\omega\mu}\sin(\phi)\sum_{n=1}^{\infty}\left[a_n\,\hat{J}_n(kr)+b_n\,\hat{H}_n^{(2)}(kr)\right]P_n^1(\cos(\theta)) \qquad (A.7)$$

$$\left(\frac{\partial^2 F_r^+}{\partial r\partial\theta}\right)=\frac{E_0}{k}\sin(\phi)\sum_{n=1}^{\infty}\left[a_n\frac{\partial\hat{J}_n(kr)}{\partial r}+c_n\frac{\partial\hat{H}_n^{(2)}(kr)}{\partial r}\right]\frac{\partial P_n^1(\cos(\theta))}{\partial\theta} \qquad (A.8)$$

At $r=a$, H_θ^+ is expressed as:

$$H_\theta^+ = \frac{1}{a\sin(\theta)}\left[-\frac{E_0}{\omega\mu}\sin(\phi)\sum_{n=1}^{\infty}\left[a_n\,\hat{J}_n(ka)+b_n\,\hat{H}_n^{(2)}(ka)\right]P_n^1(\cos(\theta))\right]$$
$$+\frac{1}{a(j\omega\mu)}\left(\frac{E_0 k}{k}\sin(\phi)\sum_{n=1}^{\infty}\left[a_n\,\hat{J}_n'(ka)+c_n\,\hat{H}_n^{(2)\prime}(ka)\right]\frac{\partial P_n^1(\cos(\theta))}{\partial\theta}\right) \qquad (A.9)$$

Let us compute H_ϕ^+, by using $H_\phi^+ = -\frac{1}{r}\frac{\partial A_r^+}{\partial\theta}+\frac{1}{r\sin(\theta)(j\omega\mu)}\left(\frac{\partial^2 F_r^+}{\partial r\partial\phi}\right)$ as;

$$\frac{\partial A_r^+}{\partial\theta}=\frac{E_0}{\omega\mu}\cos(\phi)\sum_{n=1}^{\infty}\left[a_n\,\hat{J}_n(kr)+b_n\,\hat{H}_n^{(2)}(kr)\right]\frac{\partial P_n^1(\cos(\theta))}{\partial\theta} \qquad (A.10)$$

$$\left(\frac{\partial^2 F_r^+}{\partial r\partial\phi}\right)=\frac{E_0 k}{k}\cos(\phi)\sum_{n=1}^{\infty}\left[a_n\,\hat{J}_n'(kr)+c_n\,\hat{H}_n^{(2)\prime}(kr)\right]P_n^1(\cos(\theta)) \qquad (A.11)$$

At $r=a$, H_ϕ^+ is expressed as:

$$H_\phi^+ = -\frac{1}{a}\left(\frac{E_0}{\omega\mu}\cos(\phi)\sum_{n=1}^{\infty}\left[a_n\,\hat{J}_n(ka)+b_n\,\hat{H}_n^{(2)}(ka)\right]\frac{\partial P_n^1(\cos(\theta))}{\partial\theta}\right)$$
$$+\frac{1}{a\sin(\theta)(j\omega\mu)}\left(\frac{E_0 k}{k}\cos(\phi)\sum_{n=1}^{\infty}\left[a_n\,\hat{J}_n'(ka)+c_n\,\hat{H}_n^{(2)'}(ka)\right]P_n^1(\cos(\theta))\right)$$

(A.12)

Let us compute E_θ^- , by using $E_\theta^- = \dfrac{-1}{r\sin(\theta)}\dfrac{\partial F_r^-}{\partial\phi}+\dfrac{1}{r(\sigma_d+j\omega\varepsilon_d)}\left(\dfrac{\partial^2 A_r^-}{\partial r\,\partial\theta}\right)$ as;

$$\frac{\partial F_r^-}{\partial\phi}=\frac{E_0}{k}\cos(\phi)\sum_{n=1}^{\infty}e_n\,\hat{J}_n(k_d r)\,P_n^1(\cos(\theta))$$

(A.13)

$$\left(\frac{\partial^2 A_r^-}{\partial r\,\partial\theta}\right)=\frac{E_0 k_d}{\omega\mu}\cos(\phi)\sum_{n=1}^{\infty}d_n\,\hat{J}_n'(k_d r)\frac{\partial P_n^1(\cos(\theta))}{\partial\theta}$$

(A.14)

At $r=a$, E_θ^- is expressed as:

$$E_\theta^- = \frac{-1}{a\sin(\theta)}\left(\frac{E_0}{k}\cos(\phi)\sum_{n=1}^{\infty}e_n\,\hat{J}_n(k_d a)\,P_n^1(\cos(\theta))\right)$$
$$+\frac{1}{a(\sigma_d+j\omega\varepsilon_d)}\left(\frac{E_0 k_d}{\omega\mu}\cos(\phi)\sum_{n=1}^{\infty}d_n\,\hat{J}_n'(k_d a)\frac{\partial P_n^1(\cos(\theta))}{\partial\theta}\right)$$

(A.15)

Let us compute E_ϕ^- , by using $E_\phi^- = \dfrac{1}{r}\dfrac{\partial F_r^-}{\partial\theta}+\dfrac{1}{r\sin(\theta)(\sigma_d+j\omega\varepsilon_d)}\left(\dfrac{\partial^2 A_r^-}{\partial r\,\partial\phi}\right)$ as;

$$\frac{\partial F_r^-}{\partial\theta}=\frac{E_0}{k}\sin(\phi)\sum_{n=1}^{\infty}e_n\,\hat{J}_n(k_d r)\frac{\partial P_n^1(\cos(\theta))}{\partial\theta}$$

(A.16)

$$\left(\frac{\partial^2 A_r^-}{\partial r\,\partial\phi}\right)=\frac{-E_0 k_d}{\omega\mu}\sin(\phi)\sum_{n=1}^{\infty}\left[d_n\,\hat{J}_n'(k_d r)\right]P_n^1(\cos(\theta))$$

(A.17)

At $r=a$, E_ϕ^- is expressed as:

$$E_\phi^- = \frac{1}{a}\left(\frac{E_0}{k}\sin(\phi)\sum_{n=1}^{\infty}e_n\,\hat{J}_n(k_d a)\,\frac{\partial P_n^1(\cos(\theta))}{\partial\theta} \right)$$
$$+ \frac{1}{a\sin(\theta)(\sigma_d + j\omega\varepsilon_d)}\left(\frac{-E_0\,k_d}{\omega\mu}\sin(\phi)\sum_{n=1}^{\infty}\left[d_n\,\hat{J}_n'(k_d a) \right]P_n^1(\cos(\theta)) \right)$$

(A.18)

Let us compute H_θ^-, by using $H_\theta^- = \frac{1}{r\sin(\theta)}\frac{\partial A_r^-}{\partial\phi} + \frac{1}{r(j\omega\mu_d)}\left(\frac{\partial^2 F_r^-}{\partial r\,\partial\theta} \right)$ as;

$$\frac{\partial A_r^-}{\partial\phi} = -\frac{E_0}{\omega\mu}\sin(\phi)\sum_{n=1}^{\infty}d_n\,\hat{J}_n(k_d r)\,P_n^1(\cos(\theta))$$

(A.19)

$$\left(\frac{\partial^2 F_r^-}{\partial r\,\partial\theta} \right) = \frac{E_0\,k_d}{k}\sin(\phi)\sum_{n=1}^{\infty}e_n\,\hat{J}_n'(k_d r)\frac{\partial P_n^1(\cos(\theta))}{\partial\theta}$$

(A.20)

At $r=a$, H_θ^- is expressed as:

$$H_\theta^- = \frac{1}{a\sin(\theta)}\left(-\frac{E_0}{\omega\mu}\sin(\phi)\sum_{n=1}^{\infty}d_n\,\hat{J}_n(k_d a)\,P_n^1(\cos(\theta)) \right)$$
$$+ \frac{1}{a(j\omega\mu_d)}\left(\frac{E_0\,k_d}{k}\sin(\phi)\sum_{n=1}^{\infty}e_n\,\hat{J}_n'(k_d a)\frac{\partial P_n^1(\cos(\theta))}{\partial\theta} \right)$$

(A.21)

Let us compute H_ϕ^-, by using $H_\phi^- = -\frac{1}{r}\frac{\partial A_r^-}{\partial\theta} + \frac{1}{r\sin(\theta)(j\omega\mu_d)}\left(\frac{\partial^2 F_r^-}{\partial r\,\partial\phi} \right)$ as;

$$\frac{\partial A_r^-}{\partial\theta} = \frac{E_0}{\omega\mu}\cos(\phi)\sum_{n=1}^{\infty}d_n\,\hat{J}_n(k_d r)\frac{\partial P_n^1(\cos(\theta))}{\partial\theta}$$

(A.22)

$$\left(\frac{\partial^2 F_r^-}{\partial r\,\partial\phi} \right) = \frac{E_0\,k_d}{k}\cos(\phi)\sum_{n=1}^{\infty}e_n\,\hat{J}_n'(k_d r)\,P_n^1(\cos(\theta))$$

(A.23)

At $r=a$, H_ϕ^- is expressed as:

$$H_\phi^- = -\frac{1}{a}\left(\frac{E_0}{\omega\mu}\cos(\phi)\sum_{n=1}^{\infty} d_n\,\hat{J}_n(k_d a)\frac{\partial P_n^1(\cos(\theta))}{\partial\theta} \right)$$
$$+ \frac{1}{a\sin(\theta)(j\omega\mu_d)}\left(\frac{E_0 k_d}{k}\cos(\phi)\sum_{n=1}^{\infty} e_n\,\hat{J}_n'(k_d a)P_n^1(\cos(\theta)) \right)$$

(A.24)

With the continuity of tangential components of electric and magnetic fields at $r=a$, one can reduce the four relations into the following forms:

$$a_n\,\hat{J}_n(ka)+c_n\,\hat{H}_n^{(2)}(ka)=e_n\,\hat{J}_n(k_d a)$$

(A.25)

$$\left(a_n\,\hat{J}_n'(ka)+b_n\,\hat{H}_n^{(2)\prime}(ka) \right)\left(\frac{k}{(\sigma+j\omega\varepsilon)} \right)=\left(d_n\,\hat{J}_n'(k_d a) \right)\left(\frac{k_d}{(\sigma_d+j\omega\varepsilon_d)} \right)$$

(A.26)

$$a_n\,\hat{J}_n(ka)+b_n\,\hat{H}_n^{(2)}(ka)=d_n\,\hat{J}_n(k_d a)$$

(A.27)

$$\left(\frac{1}{\mu} \right)\left(a_n\,\hat{J}_n'(ka)+c_n\,\hat{H}_n^{(2)\prime}(ka) \right)=\left(\frac{k_d}{k\mu_d} \right)\left(e_n\,\hat{J}_n'(k_d a) \right)$$

(A.28)

Then, one can obtain the closed form equations of the unknown constants; b_n, c_n, d_n and e_n.

APPENDIX B: *S*-PARAMETERS

S–parameters are power wave descriptors that permit us to define the input-output relations of a network in terms of incident and reflected waves. With reference to Figure B.1 below, we define an incident normalized power wave a_n^S and a reflected normalized power wave b_n^S as follows:

$$a_n^S = \frac{1}{2\sqrt{Z_0}}\left(V_n + Z_0\, I_n\right)$$

$$b_n^S = \frac{1}{2\sqrt{Z_0}}\left(V_n - Z_0\, I_n\right)$$

(B.1)

and lead to

$$V_n = \sqrt{Z_0}\left(a_n^S + b_n^S\right)$$

$$I_n = \frac{1}{\sqrt{Z_0}}\left(a_n^S - b_n^S\right)$$

(B.2)

where the index *n* refers to either port number 1 or 2. The impedance Z_0 is the characteristic impedance of the connecting lines on the input side of the network (Assuming that characteristic impedances on the input and output sides of the network are same).
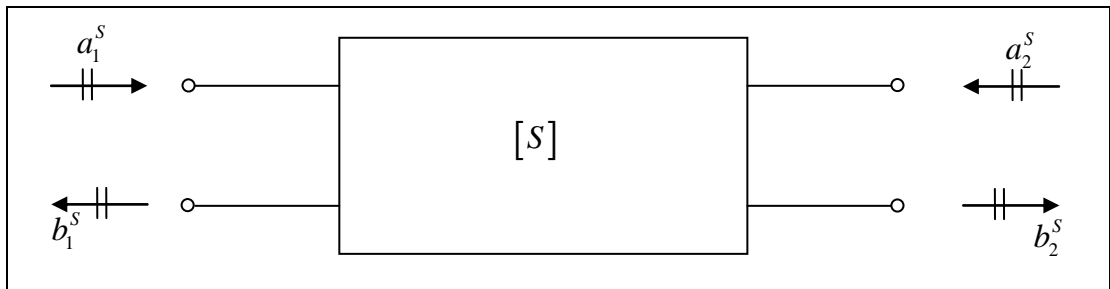

Figure B.1. Schematic illustration of directional convention of *S*-parameters

Based on the directional convention shown in the Figure B.1, we can define the *S*-parameters [127]:

$$\begin{Bmatrix} b_1 \\ b_2 \end{Bmatrix} = \begin{bmatrix} S_{11} & S_{12} \\ S_{21} & S_{22} \end{bmatrix} \begin{Bmatrix} a_1 \\ a_2 \end{Bmatrix} \tag{B.3}$$

where the terms are

$$S_{11} = \left.\frac{b_1}{a_1}\right|_{a_2=0} \equiv \frac{\text{reflected power wave at port 1}}{\text{incident power wave at port 1}} \tag{B.4}$$

$$S_{21} = \left.\frac{b_2}{a_1}\right|_{a_2=0} \equiv \frac{\text{transmitted power wave at port 2}}{\text{incident power wave at port 1}} \tag{B.5}$$

$$S_{22} = \left.\frac{b_2}{a_2}\right|_{a_1=0} \equiv \frac{\text{reflected power wave at port 2}}{\text{incident power wave at port 2}} \tag{B.6}$$

$$S_{12} = \left.\frac{b_1}{a_2}\right|_{a_1=0} \equiv \frac{\text{transmitted power wave at port 1}}{\text{incident power wave at port 2}} \tag{B.7}$$

APPENDIX C: DESIGN CRITERIA FOR VIVALDI ANTENNA

On both Small Vivaldi and Large Vivaldi antennas, the tapered microstrip line is applied as the antenna feeder and a 0.5 mm thick FR4 (ε_r=4.4, tanδ=0.025) material is used for both of them as a substrate. The upper and lower layers are copper layer which have a thickness of 0.035 mm. The length and width of Large Vivaldi is 100 mm × 35 mm, and that of Small Vivaldi is 27.34 mm × 14 mm. The theoretical design equations for a conventional Vivaldi antenna are as follows [124]:
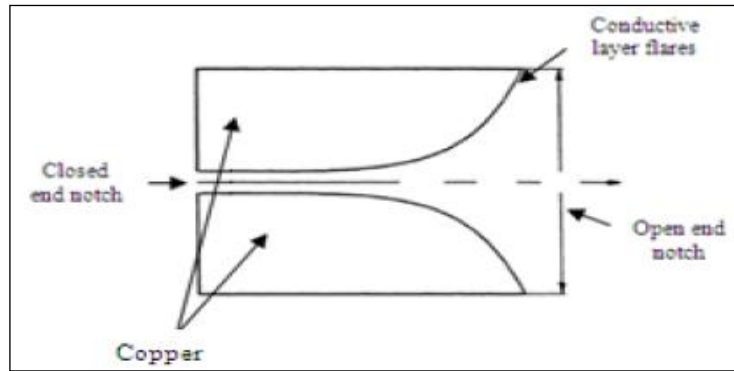

Figure C.1. Schematic illustration of a conventional Vivaldi antenna

In theory, the maximum opening width is

$$W_{\max} = \frac{c}{2 f_{\min} \sqrt{\varepsilon_{ref.}}}$$
(C.1)

Then, the minimum opening width is

$$W_{\min} = \frac{c}{2 f_{\max} \sqrt{\varepsilon_{ref.}}}$$
(C.1)

where $\varepsilon_{ref.}$ corresponds to the effective dielectric constant of the substrate.

The frequency response results of return loss of the Vivaldi antennas have been given in Section 5.

The resulting far-field radiation pattern of the Small Vivaldi antenna operating in coupling medium is also given to show the end-fire radiator behavior of the Vivaldi antenna, as follows:
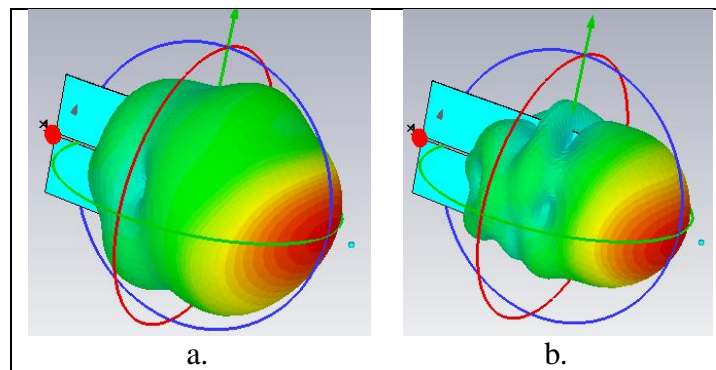

| a. | b. |

Figure C.2. Far-field radiation pattern of the Small Vivaldi antenna operating in coupling medium for a. 5 GHz and b. 9 GHz